2013

Nanoindentation characterization of clay minerals and clay-based hybrid bio-geomaterials

Rohit Raj Pant
Louisiana State University and Agricultural and Mechanical College

NANOINDENTATION CHARACTERIZATION OF CLAY MINERALS AND CLAY-BASED HYBRID BIO-GEOMATERIALS

A Dissertation

Submitted to the Graduate Faculty of the
Louisiana State University and
Agricultural and Mechanical College
in partial fulfillment of the
requirements for the degree of
Doctor of Philosophy
in

The Department of Civil and Environmental Engineering

by
Rohit Raj Pant
B.E., National Institute of Technology Rourkela, 2002
M.S., Louisiana State University and A&M College, 2007
December 2013

To

My grandparents

My parents

My family

My teachers

and

My alma mater

Acknowledgements

I would like to express my sincere gratitude to my advisor, Dr. Guoping Zhang, whose expertise, understanding and patience added considerably to my graduate experience. I cannot thank you enough for your guidance and continuous support throughout my Ph.D. journey. I also wish to express my deep appreciation to the members of my graduate committee: Dr. Murad Y. Abu-Farsakh, Dr. Jungwon Jung, Dr. Ying Wang and Dr. Steven G. Hall. Your encouragement, guidance, and valuable suggestions have highly benefited my PhD work.

I would also like to acknowledge the elucidating discussions with Professor G. Byerly, LSU and Dr. V.P. Singh, CAMD-LSU. Technical support of Mr. Rick Young, Rock Preparations Laboratory lab, Ms. Wanda LeBlanc, X-Ray Diffraction & Geochemistry Lab, Dr. Dogmei Cao, Material Characterization Center and Ying Xiao, Biological Sciences, LSU in sample preparation and SEM/TEM imaging is greatly appreciated. I have greatly benefited from the collaboration with my fellow research group members, thank you for your time, patience and insightful discussions.

I thank my grandparents, parents and my family for the support they provided me through my entire life. Your love and support has given me the strength and guidance to pursue my dreams and succeed in my career path.

Table of Contents

List of Tables

List of Figures

Abstract

Layered hydrous aluminosilicates are key constituent minerals in rocks, soils, and other parts of the Earth crust. Understanding mechanical properties of these aluminosilicates is crucial for seismic study, stability of parent rocks and geomaterials, and for geophysical subsurface exploration. Recently, growing prospects of clay based nanocomposites have renewed further interest in understanding the fundamental elastic and plastic properties of hydrous aluminosilicates. Their distinct, nanoscale layered crystal structure is known to result in anisotropic responses to loading, however, owing to their tiny sizes; it is a significant challenge to determine the anisotropic properties. There is a little data available in the literature on the elastic and plastic properties of clays and clay-based geomaterials. This Ph.D. research work has undertaken the novel approach to study mechanical properties of geomaterials using a pioneering nanomechanical testing method, nanoindentation, to probe the elastic and plastic properties at nano/micro scale. Genesis of these nanomechanical properties are analyzed in the light of microstructures, interatomic bonds, mineralogical and chemical composition.

A nanoindentation study of muscovite mica revealed highly anisotropic behavior. Both elastic and plastic anisotropy exist for indentation normal and perpendicular to the basal plane. Nano-mechanical behavior of the well-ordered, nanocrytalline clay minerals is, mainly, governed by generation and storage of dislocations, formation and annihilation of kink bands and intermittent kink bands. Interpretations of indentation test based on continuum mechanics and gradient plasticity models, therefore, give satisfactory result. On the other hand, chemical, morphological, microstructural and structural characterization of a hybrid clay-lime-starch bio nanocomposite material revealed highly heterogeneous, amorphous and multi-phase matrix. Statistical analysis of the massive volume of data obtained using grid indentation technique

revealed that this matrix is composed of five distinct mechanical phases. Thus, this study proposes that slow and weak pozzolanic reaction between clay and lime produces cementitious binder network consisting of C-S-H phase. Interaction of the biopolymer (sticky rice) with clay and C-S-H resulted in intercalated nanocomposites that have superior mechanical and barrier properties. Clay, sand, and silt particles act as active fillers in this composite, whereby forming a dense and compact mass, which renders durability and toughness to this hybrid composite.

Chapter 1. Introduction

1.1. Background

Physical and chemical properties of geo-materials are of paramount significance to modern engineering realm. Everything we produce, built, or discard comes from, supported on or disposed onto this planet. Be it a conventional usage as construction material or novel clay based nano-composites, understanding of physical-chemical properties is essential. Particularly with a very strict window of accuracy in modern design, need for more robust models and understanding of characteristic behavior of constituent minerals with in multiphase geo-material is ever increasing. High stakes in the performance of nuclear waste repository to exploration, drilling and yield of hydrocarbon reservoir demands precise modeling of physical and chemical behavior of underlying geo-materials. This is quite a daunting task owing to heterogeneous and multiphase composition of natural geo-materials. Therefore, to understand macro scale behavior of geo-materials, micro/nano scale study of individual phases and thier interaction is very significant.

Clay minerals or hydrous aluminosilicates, also known as phyllosilicates, are one of the major constituents of the geo-materials. Understanding the mechanical properties of clay minerals, thus, is essential for understanding the micro/macro behavior of geo-material as a whole. However, the tiny size of individual clay crystals imposes a significant challenge to the experimental determination of elastic and plastic properties. Past research on mechanical properties of phyllosilicates used techniques such as Brillouin spectroscopy, X-ray or neutron diffraction, ultrasonic measurements, and more recently molecular dynamics simulation.

A nanomechanical testing method, nanoindentation, has been utilized to assess elastic and plastic properties of metals, ceramics, thin films and biological specimens. Following the

theoretical framework of Vlassak (1993), Vlassak et al. (2003), Swadener and Pharr (2001), Delafargue and Ulm (2004) and others, nanoindentation technique has been further extended to study anisotropy of metals, bones and clay minerals. Similarly, elastic modulus of well-ordered mica and rectorite specimens showed good agreement between experimental and theoretical values for indentation modulus normal to basal plane (Zhang et al., 2009).

1.2. Objective and Scope

This research focused on the nano/micro mechanical behavior of clay minerals and clay-based geo-materials using nanoindentation technique. Two geo-materials were chosen in this study: muscovite mica and hybrid clay-lime-starch-bio-nano-composite from the archeological site in China. Muscovite mica is well ordered, has relatively large crystal structure and exhibit distinct layered structure representative of clay minerals. Hybrid clay-lime-starch bio nano-composite is a matrix of coarse and fine aggregated bonded by clay based cementing binder. The granular structure of clay concrete is, thus, expected to exhibit amorphous structure. These two geo-materials, therefore, reflects the progression from highly ordered, crystalline, homogeneous structure to heterogeneous and amorphous state.

Nanoindentation techniques is frequently used to assess the mechanical properties such as Young's modulus, E, hardness, H, yield stress, σ_y, anisotropy etc. Purpose of nanoindentation in mica is twofold. First, to evaluate elastic and plastic properties along different crystallographic directions, anisotropic response and indentation size effects in phyllosilicate minerals. These properties have significant practical implication in various fields such as subsurface explorations, seismology and synthesis of clay based nanocomposites to name few. Second application is more semantic, this research aims to elucidate on nanomechanical deformation behavior of mica,

which can then be expanded to apply to other phyllosilicates, synthetic layered structures and thin films.

Characterizations of hybrid nanocomposite include morphological, chemical and structural analysis using optical microscopy, electron microscopy (SEM/EDS, TEM), X-ray diffraction, and NMR spectra analysis. Physical and chemical structures of individual phases in the heterogeneous clay concrete are expected to influence nano-mechanical properties. Using the nanoindentation technique, elastic-plastic properties of individual phases as well as that of the composite as a whole is studied. Clay based geopolymers are emerging as a versatile, ecofriendly and renewable construction material resources and a potent alternative to conventional cement concrete. Hybrid clay cement from the archeological site used in this study has exhibited durability, impressive physical and chemical properties and some striking morphological characteristics. By understanding the mechanism of physical and chemical structure that imparts these characteristic properties can enrich the ongoing research on novel clay based cements and geopolymers.

1.3. Organization of the Dissertation

This dissertation consists of seven chapters prepared in a technical format approved by Graduate School of Louisiana State University. A brief outline of each chapter is presented in the following paragraphs.

Current chapter presents the brief introduction, research outline and organization of the dissertation. Chapter two gives the literature review covering background of the clay minerals and review of the mechanical properties of clay minerals. A brief introduction of clay based binders and techniques for chemical, structural and microstructural characterization of geo-

materials is also discussed. Finally, an introduction to nanoindentation technique and its usage in characterization of geo-materials is presented in detail.

Chapter three presents results of nanoindentation in muscovite mica in two normal direction. Elastic and plastic anisotropy, indentation size effect and nanomechanical deformation mechanism along two principle crystallographic directions of mica is explored.

A brief review of indentation size effect (ISE) models and analyses of ISE observed in muscovite mica along two indentation direction are discussed in chapter four.

Chapter five and six present the results of chemical, structural, microstructural and nano-mechanical characterization of the hybrid clay-lime-starch bio nanocomposite.

Finally, chapter seven outlines the main findings of this research, limitations of the study and direction for future study.

1.4. References

Delafargue, A., & Ulm, F. J. (2004). Explicit approximations of the indentation modulus of elastically orthotropic solids for conical indenters. *International Journal of Solids and Structures, 41*(26), 7351-7360. doi: 10.1016/j.ijsolstr.2004.06.019

Swadener, J. G., & Pharr, G. M. (2001). Indentation of elastically anisotropic half-spaces by cones and parabolae of revolution. *Philosophical Magazine A, 81*(2), 447-466. doi: 10.1080/01418610108214314

Vlassak, J. (1993). Indentation modulus of elastically anisotropic half spaces. *Philosophical Magazine A, 67*(5), 1045-1056.

Vlassak, J. J., Ciavarella, M., Barber, J. R., & Wang, X. (2003). The indentation modulus of elastically anisotropic materials for indenters of arbitrary shape. *Journal of the mechanics and physics of solids, 51*(9), 1701-1721. doi: 10.1016/s0022-5096(03)00066-8

Zhang, G., Wei, Z., & Ferrell, R. E. (2009). Elastic modulus and hardness of muscovite and rectorite determined by nanoindentation. *Applied Clay Science, 43*(2), 271-281. doi: 10.1016/j.clay.2008.08.010

Chapter 2. Literature Review

2.1. Clay and Clay Minerals

The term clay is often used ambiguously in geotechnical engineering. For example, clay as a size term refers to constituents of a soil with particle size smaller than 2 μm whereas as a mineral class it refers to a layered, platy structures that has net negative electrical charge and produce plasticity when mixed with water (Mitchell & Soga, 2005). Thus in order to avoid the ambiguity, use of term 'clays' and 'clay minerals' is adopted by Nomenclature Committee of the Association Internationale pour l'Etude des Argiles (AIPEA) and used in this dissertation. The clay is, thus, defined as a naturally occurring material composed primarily of fine-grained minerals, which is generally plastic at appropriate water contents and will harden when dried or fired and clay mineral refers to phyllosilicate minerals and to minerals which impart plasticity to clay and which harden upon drying or firing (Guggenheim et al., 2006; Guggenheim & Martin, 1995). Based on this, it can be inferred that clay are naturally occurring geomaterials that contain both clay minerals as well as associated phases such as organic and inorganic inclusions. Similarly, clay minerals also include any minerals, other than phyllosilicates, that impart both plasticity and hardening characteristic to clays.

2.1.1. General Structure and Classification of Clay Minerals

Unit structure of phyllosilicates constitute of combination of two structural units: silicon tetrahedron (silicon and four oxygen in tetrahedral combination) and the aluminum or magnesium octahedron (Mg^{2+} or Al^{+3} in octahedral combination with anions such as O, OH, Cl, S) (Mitchell & Soga, 2005). In a planar phyllosilicates, tetrahedral sheet of composition T_2O_5 (T= Si, Al, Fe^{3+}, Be, B etc.) is formed by sharing of three basal oxygen forming continuous two dimensional structure (usually hexagonal net) and fourth apical oxygen pointing in any direction

(Guggenheim et al., 2006; Mitchell & Soga, 2005). Thickness of this layer in phyllosilicates is 4.63 Å. Octahedral sheet is formed by edge sharing octahedron and has thickness of 5.05 Å. Octahedral sheet with trivalent cation such as $Al_2(OH)_6$ has only two-third of cationic spaces filled and the structure is called dioctahederal. On the other hand, octahedral sheet with divalent cation such as in $Mg_3(OH)_6$ has all possible cation sites occupied and structure is termed as tri-octahederal. In addition to Mg^{2+} and Al^{3+}, other cations (Fe^{2+}, Fe^{3+}, Mn^{+2}, Ti^{4+}, Ni^{2+}, Cr^{3+} and Li^{+} may also be present by isomorphous substitution (Mitchell & Soga, 2005).

Stacking of tetrahederal and octahederal sheets forms a layer. A 1:1 layer is formed by combination of one tetrahedral and one octahederal sheet whereas 2:1 layer has an octahedral sheet between two opposing tetrahederal sheet (Guggenheim et al., 2006). Interlayer materials such as cations, hydrated cations, organic material, hydroxide octahedral and/or hydroxide octahedral sheets or none may be present between interlayer galleries (Figure 2.1). A unit structure constituting a clay mineral is, thus, a total assembly of layers and interlayer species (Guggenheim et al., 2006). Clay minerals thus can be classified based on the stacking sequence, net layer charge and octahederal characteristic. Table 2.1 presents the classification of planar phyllosilicates based on AEPA recommendation (Guggenheim et al., 2006, 2007).

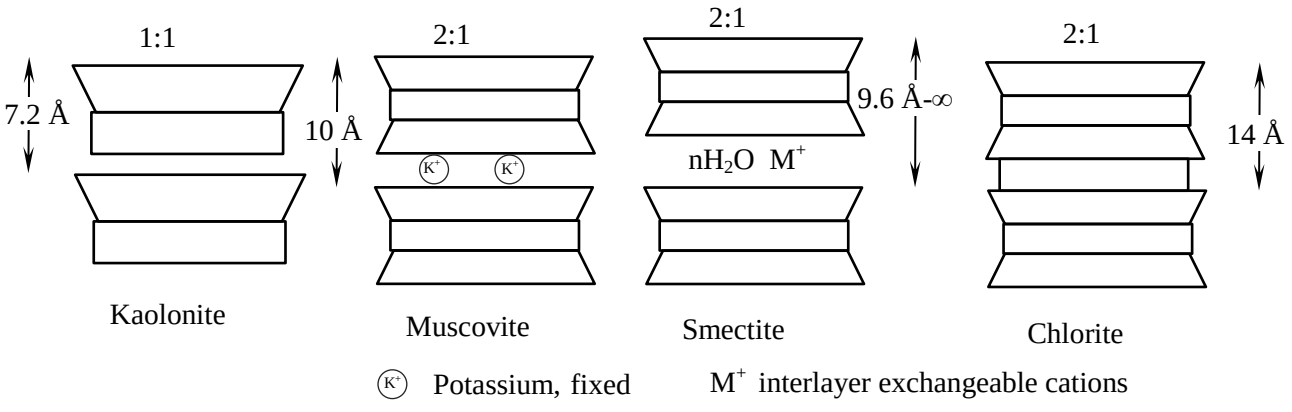

Figure 2.1: Schematic diagram of the structures of clay minerals (adopted from (Mitchell & Soga, 2005)).

Table 2.1: Classification of planar phyllosilicates (after (Guggenheim et al., 2006, 2007))

Layer Type	Interlayer Material	Group	[a]Oct. Char.	Species
1:1	None or H_2O x≈0	Serpentine-kaolin	Tri	Lizardite, berthierine, amesite, cronstedtite, nepouite, kellyite, fraipontite, brindleyite
			Di	Kaolinite, dickite, nacrite, halloysite (planar)
			Di, Tri	Odinite
2:1	None x≈0	Talc-pyrophyllite	Tri	Talc, willemseite, kerolite, pimelite
			Di	Pyrophyllite, ferripyrophyllite
	Hydrated exchangeable x≈0.2-0.6	Smectite	Tri	Saponite, hectorite, sauconite, stevensite, swinefordite
			Di	Montmorillonite, beidellite, nontronite, volkonskoite
	Hydrated exchangeable x≈0.6-0.9	Vermiculite	Tri	Trioctahedral vermiculite
			Di	Dioctahedral vermiculite
	Non-hydrated monovalent cations (≥50% mono) x ≈ 0.85-1 for Di	True mica	Tri	Phlogopite, siderophyllite, aspidolite
			Di	Muscovite, celadonite, paragonite
	Non-hydrated mono- or divalent cations x ≈ 0.6-0.85	Interlayer-deficient mica	Tri	Wonesite[b]
			Di	none[c]
	Non-hydrated divalent cations (≥50% div.) x≈1.8-2.0	Brittle mica	Tri	Clintonite, kinoshitalite, bityite, anandite
			Di	Margarite, chernykhite
	Hydroxide sheet x = variable	Chlorite	Tri	Clinochlore, chamosite, pennantite, nimite,
			Di	Donbassite
			Di,tri	Cookeite, sudoite
			Tri,di	None
2:1	Regularly interstratified x = variable	Variable	Tri	Corrensite, aliettite, hydrobiotite, kulkeite
			Di	Rectorite, tosudite, brinrobertsite
1:1, 2:1			Tri	Dozyite

x is net layer charge p.f.u., given as a positive number, [a]Octahederal character, Di=dioctahederal, tri=trioctahederal [b]net layer charge may be <0.6, but this is an exception. [c] Illite and other micas are omitted being 'series' name.

2.1.2. Review of Mechanical Properties of Clay Minerals

Elastic and plastic properties of geo-materials have conventionally been determined by various macro and micro scale testing such as acoustic, X-ray diffraction, Berrilium scattering, ultrasonic velocity measurements, triaxial testing and more recently using molecular dynamic simulation. Table 2.2 presents survey of mechanical properties and micro testing method as applied to clays and clay based nanocomposites.

Table 2.2: Mechanical properties of clays and clay based nano-composites.

Method	Properties	References
Acoustic Methods	Bulk Modulus(K), Shear Modulus (G)	(Kroner, 1967),Mondol et al. (2008), Vanorio et al. (2003), Wang et al. (2001)
Molecular Dynamics Simulation	Elastic Moduli (E_1, E_2, E_3), Bulk Modulus (K), Shear Modulus (G)	Seo et al. (1999), Sato et al. (2001), Manevitch and Rutledge (2003),Cygan et al. (2004), Teich-McGoldrick et al. (2012)
Brillouin Scattering Method	Elastic Stiffness Constant (C_{ijkl})	Vaughan and Guggenheim (1986), McNeil and Grimsditch (1993)
Atomic Force Microscopy (AFM)	Elastic Moduli, Morphology, Friction Angle	Zbik and Smart (1998); Bickmore et al. (2002), Kosoglu et al. (2010), Piner et al. (2003) Ploehn and Liu (2006), Prasad et al. (2002)
X-ray Diffraction with Diamond Anvil Cell (DAC)	Bulk Modulus (K)	Dera et al. (2003), Pawley et al. (1995), Zanazzi et al. (2007), Comodi and Zanazzi (1995), Hazen and Finger (1978)
Miniature Triaxial Testing	Yield Stress, Activation Energy (Q), Anisotropy	Shea and Kronenberg (1992), Christoffersen and Kronenberg (1993)
Nanoindentation	Elastic Moduli (E_1, E_2, E_3), Hardness (H), Anisotropy.	Zhang et al. (2009), Wei (2009), Basu et al. (2009)

Table 2.3 presents the range of mechanical properties of some of the representative clay minerals based on the references given in Table 2.2. Review of mechanical properties of clay mineral suggests that there is a large variation in these reported values. While some of the discrepancies in the reposted properties are obviously from sample to sample variation: different mineralogical

compositions depending upon the source of minerals, sometimes large variation is observed depending upon the testing method. This is again due to limitations in the testing methods, sample preparation and assumptions in the theoretical models.

Table 2.3: Mechanical properties of common clay minerals (adopted from (Wei, 2009))

Minerals	Elastic Modulus *E* (GPa)	Bulk Modulus *K* (GPa)	Shear Modulus *G* (GPa)	References
Serpentine-Kaolin				
Dickite	11.2	6.2		Prasad et al. (2002)
		68.3		Dera et al. (2003)
Kaolinite	3.4	1.5	1.4	Mavko et al. (1998)
poorly crystallized (KGa-2)	73.5	44.0	22.1	Wang et al. (2001)
well crystallized (KGa-1b)	74.2	47.9	19.7	Wang et al. (2001)
Kaolinite	21.5-24.1	7.9-17.8	4.7-10.2	Mondol et al. (2008)
	40.3			Ulm and Abousleiman (2006)
Talc-pyrophyllite				
Talc	74.9-73.8	41.6-41.0		Pawley et al. (2002)
				Pawley et al. (1995)
Pyrophyllite	66.6	37.0		Pawley et al. (2002)
Smectite				
Montmorillonite (SWy-1)	51.6	29.7	16.4	Wang et al. (2001)
Na-rich montmorillonite (SWy-2)	61.8	34.7	20.3	Wang et al. (2001)
Mg-rich montmorillonite (SHca-2)	98.3	63.4	26.2	Wang et al. (2001)
Ca-rich montmorillonite (STX-1)	82.1	49.6	24.4	Wang et al. (2001)
Smectite	33.1-39.5	12.3-29.0	7.9-15.6	Mondol et al. (2008)
Mica				
Phlogopite	112.0	58.5	40.1	Mavko et al. (1998)
Biotite	57.6-102.7	41.1-59.7	12.4-42.3	Mavko et al. (1998)
Muscovite	72.5-116.3	42.9-61.5	22.2-41.1	Mavko et al. (1998)
Muscovite (K-rich)		49.0		Comodi and Zanazzi (1995)
Muscovite (Na-rich)		54.0		
Illite and illite mixed layers				
Illite (IMT-2)	93.8	60.1	25.3	Wang et al. (2001)
Illite/smectite (ISMT-2)	61.2	36.7	18.4	Wang et al. (2001)
Chlorite				
Chlorite (ripidolite) (CCa-2)	232.8	164.3	51.4	
Chlorite	156.6	86.9		Pawley et al. (2002)

2.2. Clay Based Composites

Clay based composites have attracted a great deal of attention recently due to growing potential in technological and industrial applications such as in paper, rubber and elastomers, mechanical and thermal coatings, food packaging etc. (Cook & Pickering, 1968; Harvey & Lagaly, 2006; Joly et al., 2002; Theng, 1970). Incorporation of clays and clay minerals in polymers as fillers is now a well-established practice to enhance the physical-chemical properties of the composites such as rheology, elastic-plastic strength, thermal and hydraulic conductivity, electrical and chemical insulation. Mode of dispersion of cay particles in the matrix mainly as segregated tectoid dispersion, intercalated layers or exfoliated nano layers chiefly governs the nanomechanical characteristic of the clay-polymer composites (Lan et al., 1995). However, interaction of dispersed clay with polymers is not merely that of extender or filler material. It is rightly suggested that chemical reactivity of the clay minerals actively influence polymerization of monomers (Theng, 1970; Theng & Walker, 1970) or chemically interact with preformed polymers (Uskov et al., 1966).

2.2.1. Mechanism of Clay-polymer Interaction in Nanocomposites

Interaction of clay minerals with polymers can be discussed in terms of the charge characteristics of the clay surfaces and polymer concerned (Theng, 1970; Theng, 2012) . Typically, 2:1 type layer silicates have residual negative charge due to isomorphous substitution. Also, the siloxane surface of the silicate layer provides the scope for hydrogen bonding, although weaker in nature. On the other hand, basal hydroxyl surface of 1:1 type layer silicates can form strong hydrogen bond. Thus, uncharged linear macromolecules of non-ionic polymers are primarily adsorbed to negatively charged clay mineral surfaces through ion-dipole and van der Waals interactions. On the other hand, charged polymers are primarily adsorbed to clay mineral

surface through electrostatic interaction. Typically, polymer adsorption of polymers on a clay mineral surface decreases in the order of cationic >non-ionic >anionic (Gu & Doner, 1992). Since polymer molecules are long, flexible and polyfunctional, these molecules can attach to a clay surface by numerous segment (Theng, 1970) bonds thus forming train-loop-tail conformation (Figure 2.2) (Theng, 2012).

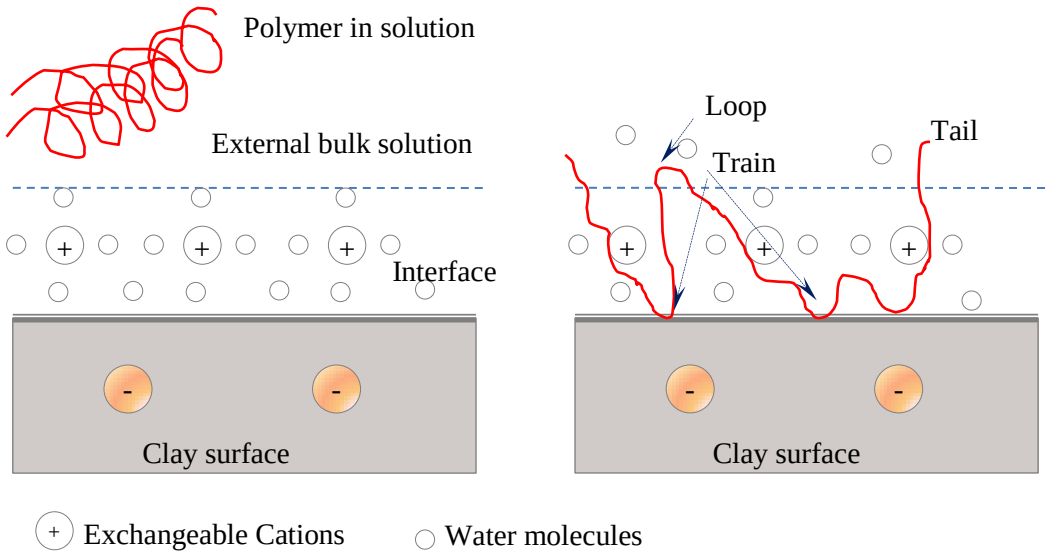

Figure 2.2: Adsorption of an uncharged polymer chain onto a negatively charged clay surface forming train-loop-tail configuration (adopted from (Theng, 2012)).

2.2.2. Classification of Clay Based Composites

Numerous uses of clay-based composites have produced several classes of clay-based composite. However, based on the structure of the clay in the composite these materials can be broadly classified in two groups: micro-composite and nanocomposites.

As the name suggests, clay-based microcomposites contains clays in the bulk form or as aggregates (tactoids) of several micrometer size. In these materials, clay components make substantial proportion of the matrix, >25 % (Theng, 2012). Function of clay in these types of composites is primarily as a filler or extender, however, as mentioned above, clay minerals in these system are not necessarily chemically inert (Uskov et al., 1966).

In clay based nanocomposites, incorporated clay particles have at least one dimension in nanometer range (<100 nm) and typically clay makes only minimal proportion (<5%) of the matrix (Theng, 2012). Based on the clay-polymer interaction, clay based nanocomposites can be further classified into two structurally distinct nanocomposites: intercalated and exfoliated type (Lan et al., 1995; Theng, 2012). In the intercalated structure, one or more molecular layers of polymers penetrate the interlayer space of the clay minerals. Typically, clay content of these systems is high (>50%) and properties resembles that of ceramic host (Lan et al., 1995). On the other hand, in the exfoliated type composites, individual silicate layers are more or less dispersed in ordered or disordered fashion (Theng, 2012). Clay content in these types of nanocomposites is typically low and properties of the matrix resemble that of host polymer host. Nevertheless, incorporation of nanosize clay particles in the matrix significantly enhances the mechanical, thermal and barrier properties of the nanocomposites.

2.2.3. Clay Based Cementitious Binder

Uses of clay based binders have been in practice since early civilization. Mix of mud (clay rich) and cow dung was used to build wall and adobe in India and other central Asian region since primitive times. Practice of construction of lime coated mud wall has been recorded as early as 2500 B.C. in this region. Similarly, Chinese used mix of lime, clay, sand and organic polymer (starch) to prepare novel construction material during Han dynasty (206 B.C.-220 A.D.).

Physical and chemical reaction between lime (Ca^{+} source) and clay is still employed in many modern construction methods. Lime stabilization is still a viable and economical option in stabilization of plastic clays. Ordinary Portland cement (OPC) can also act as calcium source and thus stabilize the plastic clays (Prusinski & Bhattacharja, 1999). Improvement of clay soils with

lime or OPC involves cation exchange, flocculation and agglomeration, cementitious hydration (in case of OPC only) and pozzolanic reaction.

Reaction of a solid aluminosilicate with a highly concentrated aqueous alkali hydroxide or silicate solution produces a synthetic alkali aluminosilicate material generically called a 'geopolymer' (Davidovits, 1991) or alternatively geo-cement (Krivenko, 1994; Krivenko & Kovalchuk, 2007) low temperature aluminosilicate glass (Rahier et al., 1996), alkali activated cement (Palomo & López dela Fuente, 2003) or simply inorganic polymer concrete (Cyr et al., 2012; Sofi et al., 2007). In general, different nomenclature in the literature originates from the variety of raw materials used in synthesis and variation of microstructure, physical, chemical and thermal properties of the end product thereof. However, the underlying chemistry for above products can be described as a complex system of coupled alkali mediated dissolution and precipitation reactions in an aqueous reaction substrate (Duxson et al., 2007). These inorganic polymers or geopolymers have numerous properties such as high compressive strength, low shrinkage, fire resistance, acid resistance and waste immobilization. Further, production of these inorganic polymers from industrial wastes has significant advantage in terms of cost effectiveness and Greenhouse gas reduction. Therefore use of inorganic polymer as a cementitious binder as a substitute for OPC has recently garnered a lot of attention.

2.3. Techniques for Chemical, Structural and Microstructural Characterization

2.3.1. X-ray Diffraction

Small wavelengths of the X-ray, of the order of 1Å, are frequently used in the analysis of the structure of crystalline materials (Mitchell & Soga, 2005). In case of clay minerals, X-ray diffraction is frequently utilized to study the basal spacing of specific species, their orientation and stacking order. On the other hand, both C-S-H and geopolymers are largely considered

amorphous to X-rays with featureless hump observed at approximately 27-29^{o} 2θ of powder X-ray Diffraction (XRD) pattern (Fernández-Jiménez & Palomo, 2005; Grutzeck et al., 1991; Yip et al., 2005). However, amorphous aluminosilicate gel is indeed a zeolite precursor and thus small content of some minor crystalline phases, zeolites, such as hydroxysodalite and herschelite are often detected in XRD spectra of geopolymers (Fernández-Jiménez & Palomo, 2005).

2.3.2. Scanning Electron Microscope (SEM)

High resolution SEM image are frequently used to study the microstructure of clays, geopolymers and C-S-H gels. SEM images can produce valuable information about morphology, pore structures, distribution of different phases in the system and therefore, contribute in clarifying the mechanism of synthesis or degree of reaction achieved for varying conditions (Fernández-Jiménez & Palomo, 2005). Another advantage of SEM image is the larger depth of field thus giving the 3-*D* image of the surface which is very valuable in assessing interaction between the aggregate and the cementing gel matrix that can have significant bearing on mechanical properties of composites. Figure 2.3 shows the SEM image raw fly ash before activation (Fernández-Jiménez & Palomo, 2005). On activation with 8.6% Na_2O, hollow spheres are consumed and amorphous aluminosilicate phase is formed. Moderate reaction resulting in porous matrix is noticed in figure 2.4b. Figure 2.4c shows coating of synthesized aluminosilicate gel on unreacted spheres which can hinder further reaction and also non-existent interfacial gap between gel and aggregate in the matrix reflecting good cementitious adhesion.

In addition to normal secondary electron scanning mode, modern SEM machines are also equipped with electron back scattering diffraction (EBSD) tool and spectrometers for chemical analysis by characteristic x-rays produced by the incident electron beam (EDS). EBSD provides quantitative microstructural information about the crystallographic nature of metals, minerals,

semiconductors, and ceramics-in fact most inorganic crystalline materials. It reveals grain size, grain boundary character, grain orientation, texture, and phase identity of the sample under the beam. In the microstructural characterization of geopolymers and C-S-H gels, back scattered electron (BSE) image are frequently utilized to distinguish activated and partially activated phase in matrix that have different mechanical properties (Davydov et al., 2011; Němeček et al., 2011).

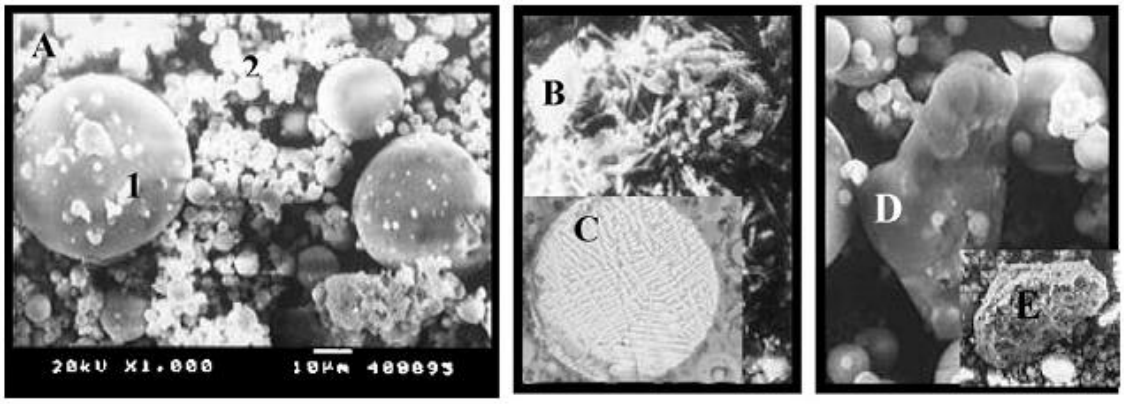

Figure 2.3: SEM micrograph of raw fly ash a) showing hollow spheres b) iron minerals c) mullite d) quartz and e) unburnt coal residue (Fernández-Jiménez & Palomo, 2005)

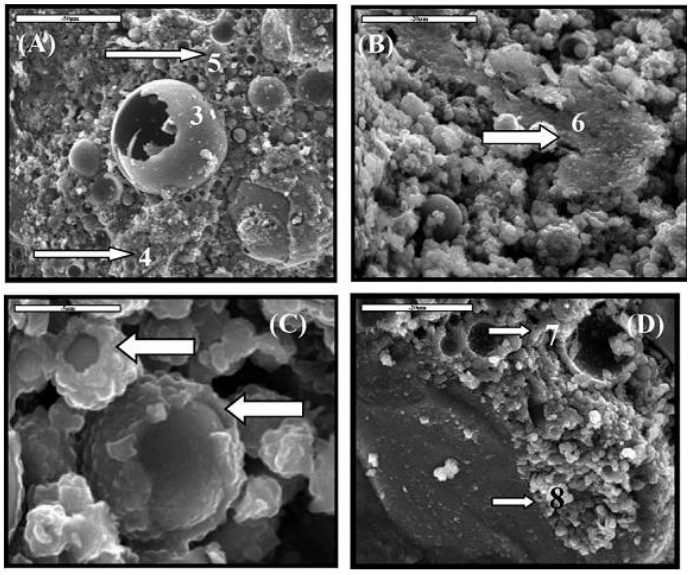

Figure 2.4: Raw fly ash activated with 8.6% Na_2O (adopted from (Fernández-Jiménez & Palomo, 2005))

2.3.3. Transmission Electron Microscope (TEM)

TEM micrograph has been recently used to study the microstructure of gel phase in geopolymers and C-S-H phase in ordinary portland cement mix (Duxson et al., 2005; Fernández-Jiménez & Palomo, 2005; Kriven et al., 2006; Richardson, 2004; Richardson & Groves, 1993). In C-S-H gel, two type of phase are frequently reported based on their elastic properties (Constantinides & Ulm, 2007; Constantinides et al., 2003; Jennings, 2000; Jennings et al., 2007; Ulm et al., 2007). C-S-H phase in Jenning's model are represented by globular 5 nm particles loosely packed in low density (LD) phase with efficiency,η=64% or densely packed high density (HD) gel with packing efficiency , η=74%. A TEM micrograph (Figure 2.5) of C-S-H phase present in C_3S cement with w/c ratio=0.5 and hardened at 20^{o}C for 8 years (Richardson, 2004) shows that size of globules in HD phase varies between 3-6 nm, however, LD phase are more fibrous in structure and diameter of the fibers extend up to 100 nm.

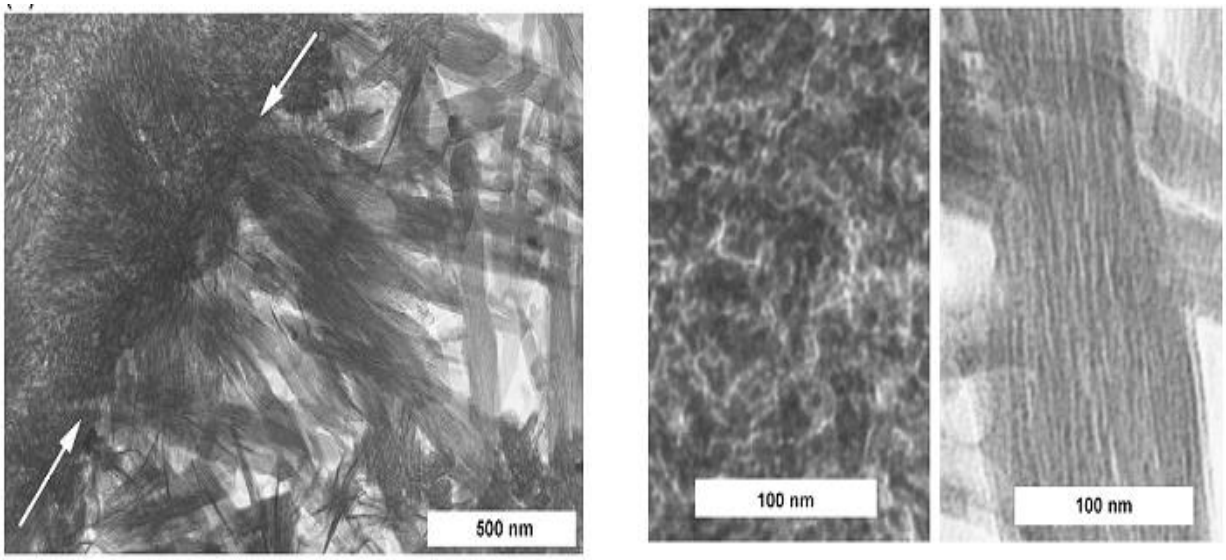

2.4a) 2.5 b)

Figure 2.5: a) TEM micrograph showing high density and low density C-S-H present in hardened C3S cement paste b) Enlargement of inner HD phase and outer LD C-S-H phase (Richardson, 2004).

2.4. Nanoindentation Technique

Nanoindentation techniques initially evolved as a tool used in mechanical characterization of materials at small scale. Originally, this method was applied to homogeneous materials such as metals, alloys and ceramics which can be modeled as continuous elastic half space (Doerner & Nix, 1986; Johnson, 1985; Oliver & Pharr, 1992, 2004). However, this technique has evolved as a versatile tool; methods have evolved to extend its uses with different shapes of indenter such as axisymmetric conical indenters (Doerner & Nix, 1986; Oliver & Pharr, 1992, 2004), spherical (J.S & Swain, 1995), parabolloid or in fact, of any arbitrary shape (Swadener & Pharr, 2001; Vlassak et al., 2003; Vlassak & Nix, 1994). So has its application beyond continuum materials; to thin films (Mencik et al., 1997), polymers, biological specimens and geo-materials (Basu et al., 2009; Bobko & Ulm, 2008; Constantinides et al., 2003; Ulm & Abousleiman, 2006; Zhang et al., 2009; Zhang et al., 2010).

Nanoindentation is technique whereby a tip of known geometry and mechanical properties is used to make an impression in a sample, with a penetration depth and force dynamically measured at resolutions of nanometers and micronewtons, respectively. The resulting force-depth curve can be analyzed to give bulk properties such as modulus and hardness, as well as to study deformation mechanisms. Oliver and Pharr method (Oliver and Pharr, 1992, 2002) which is the extension of Doerner and Nix (1986) method is frequently used to determine indentation modulus, Er and hardness, H. Figure 2.6 gives the schematic of axisymmetric conical indenter into elastic half space. During loading deformation is modeled as both elastic and plastic, however, unloading is assumed to be pure elastic recovery (Oliver and Pharr, 2002). Corresponding load-displacement or *P-h* curve is depicted in Figure 2.6d. Next few sections are devoted to derivations of mechanical properties using indentation curves.

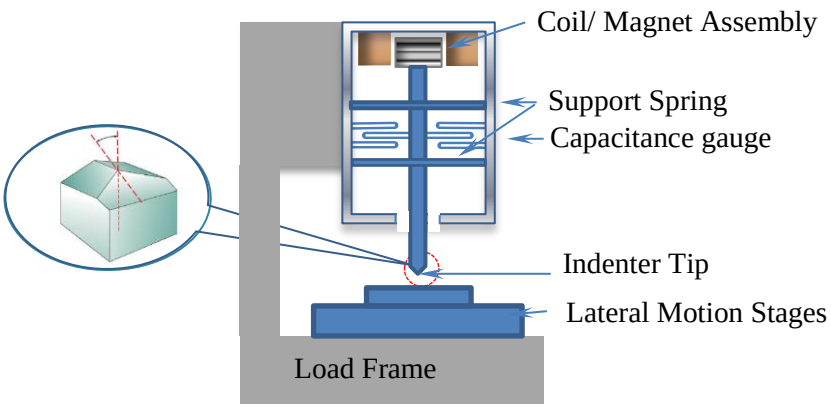

a)

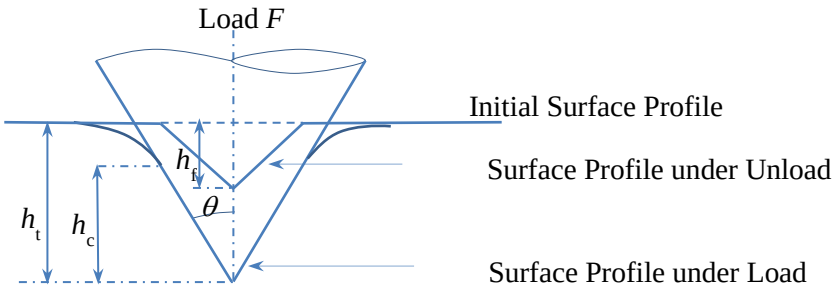

b)

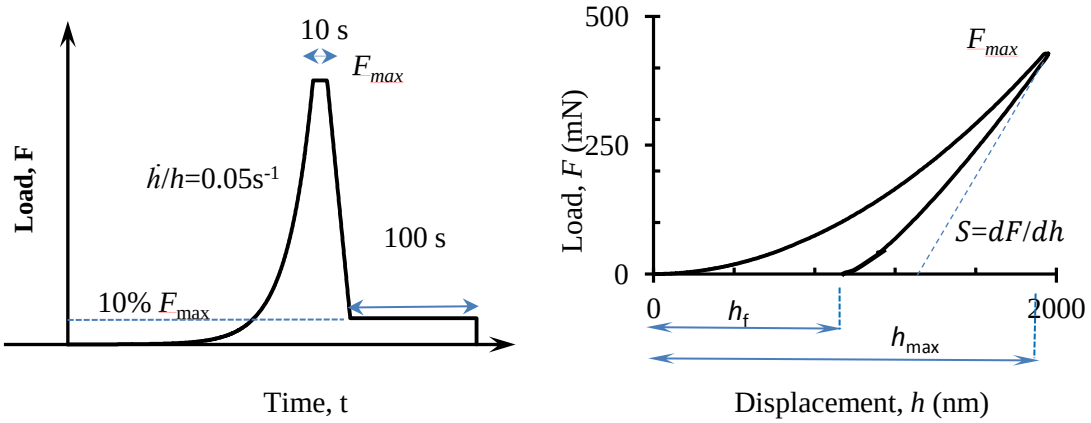

c) d)

Figure 2.6: a) Schematic of depth sensing instrument and indenter tip b) typical penetration profile into elastic-plastic half space c) loading-unloading schedule and d) corresponding load-displacement curve (*F*-*h* curve).

2.4.1. Indentation Modulus

Indentation modulus is derived as

$$\mathrm{E_r} = \frac{\sqrt{\pi}}{2\beta\sqrt{\mathrm{A_c}}}\mathrm{S} \quad [2.1]$$

$$\mathrm{S} = \frac{dP}{\mathrm{dh}}\Big|_{h_{max}} \quad [2.2]$$

where β is dimensionless correction factor for indenter tip shape and β=1.05 is commonly used for Berkovich indenter (Oliver and Pharr 2004), A_c is the projected contact area between indenter and sample, which can be obtained solely using indentation parameters (Oliver & Pharr, 1992, 2004; Sneddon, 1965).

$$\mathrm{A}_c = \mathrm{C}_0 h_c^2 + \sum_{j=1}^{8} \mathrm{C}_j h_c^{\left(\frac{1}{2}\right)^{j-1}} \quad [2.3]$$

where contact depth h_c is defined as

$$h_c = h - \varepsilon\frac{F}{S} \quad [2.4]$$

where ε is a constant that depends on indenter tip and used 0.75 for Berkovich indenter. For perfect Berkovich lead term C_0 is 24.5 and C_j (j=1, 2, …,8) are needed to describe the deviations of the Berkovich tip shape to inevitable rounding effect at the tip due to manufacturing artifacts.

The relation between the reduced and elastic moduli of the sample and indenter is expressed as (Doerner & Nix, 1986)

$$\frac{1}{\mathrm{E}_r} = \frac{1-\upsilon^2}{E} + \frac{1-\upsilon_i^2}{E_i} \quad [2.5]$$

where υ and υ_i are the Poisson's ratio of the sample and indenter, and E and E_i are the Young's modulus of the indenter and sample respectively. Previous studies suggest that the Poisson's ratio of the tested material has no significant influence on the Young's modulus (Mencik et al.,

1997) a constant υ=0.25 is assumed for mica samples. For a diamond indenter, E_i =1141 GPa and υ_i =0.07 (Oliver & Pharr, 1992).

For axisymmetric indenter and isotropic material, indentation modulus is independent of tip geometry (Pharr et al., 1992) and given as

$$E_r = \frac{E}{1-\upsilon^2} \quad [2.6]$$

However for anisotropic media, indentation modulus, E_r is complex function of elastic moduli. Analytical solution are available for indentation of anisotropic half-space by rigid and frictionless parabola of revolution (Vlassak, 1993), cones and parabola (Swadener & Pharr, 2001) and for indenters of arbitrary shapes (Vlassak et al., 2003). Delafargue and Ulm (2004) proposed an explicit solution for the indentation moduli of a transversely isotropic medium and a general orthotropic medium under rigid conical indentation in the three principal material symmetry directions. These closed form expressions were shown to be in good agreement with the much robust yet numerically exhaustive implicit solution schemes. Majority of clay minerals and clay based geopolymers exhibit transverse isotropic or orthotropic linear elastic behavior (Bobko & Ulm, 2008).

2.4.2. Hardness

Indentation hardness, *H*, is simply the measure of mean indentation stress at maximum load and given as

$$H = \frac{F_{max}}{A_c} \quad [2.7]$$

where F_{max} is the maximum force (Figure 2.6) and A_c is the contact area given by equation [2.3] and [2.4] for F_{max}. Further, relation [2.1] and [2.7] indicate that indentation modulus and hardness are not independent parameters and related by

$$E_r \propto \sqrt{H} \quad [2.8]$$

2.4.3. A Grid Indentation Technique

Previous sections outlined the methods for the extraction of mechanical properties by applying a continuum scale mechanical models to indentation into monolithic homogeneous half-space. Several researchers have extended the use of depth sensing indentation techniques to evaluate the bulk properties of heterogeneous materials. Igarashi et al. (1996) used micro-hardness test using Vickers indenter to explore mechanical properties of cementitious materials. Sakulich and Li (2010) performed nanoindentation test on engineered cement composites and Velez et al. (2001) explored the nano-mechanical properties of individual constituent of Portland cement. One of the major challenges of nanoindentation technique in heterogeneous material is to choose an indent on a specific phase with sufficient repeatability (Ulm et al., 2007). This challenge can be overcome if large numbers of indentation are performed in a grid pattern, whereby each indentation is a statistical event reflecting the response of representative equivalent volume (r.e.v.). This powerful technique has been implemented in nanomechanical characterization of geo-materials such as shales (Ulm & Abousleiman, 2006) , cement (Constantinides & Ulm, 2007; Constantinides et al., 2003; Ulm et al., 2007), biomaterials (Tai et al., 2006; Ulm et al., 2007). An underlining principle for grid indentation technique is presented in the following paragraphs.

Indentation gives the bulk properties of material at length scale $\mathcal{L}\approx 4x h_{max}$, where h_{max} is maximum penetration depth (Constantinides et al., 2003). Considering an infinite half-space composed of N different phases of characteristic length scale ℓ, such that $\ell << \mathcal{L} << D$, where D is the material length scale, for indentation depth, $h << \ell$, each indentation event is a response of one of the individual phases in the material. Thus, if large numbers of indentation are performed in grid with spacing larger than characteristic size of individual phase, probability of finding each

phase is equal to the surface fraction occupied by the two phases on the indentation surface. On the other hand, for $h >> \ell$, indentation gives some average response of the composite material. Grid indentation involves large number of indentation in arrays and statistical deconvolution of indentation results (Constantinides et al., 2006; Constantinides et al., 2003; Ulm et al., 2007).

If distribution of mechanical properties of individual phase is assumed Gaussian; for each phase 1 to *j*,

$$\mathrm{p_j(x)} = \frac{1}{\sigma\sqrt{2\pi}} \mathrm{e}^{-\frac{1}{2}\left(\frac{\mathrm{x}-\mu}{\sigma}\right)^2} \quad [2.9]$$

where μ_j is the arithmetic mean of all N_j values of each phase and σ_j is the standard deviation.

$$\mu_j = \frac{1}{N_j} \sum_{\mathrm{k}=1}^{\mathrm{Nj}} \mathrm{x_k} \quad [2.10]$$

$$\sigma_j^2(x) = \frac{1}{N_j - 1} \sum_{k=1}^{Nj} \left(x_k - \mu_k\right) \quad [2.11]$$

Now, considering all phases are Gaussian and do not interact mechanically with each other, joint probability distribution function (PDF) is given as

$$P(\mathrm{x}) = \sum_{j=1}^{N} f_j \mathrm{p_j(x)} \quad [2.12]$$

where f_j is surface fraction occupied by each phase such that, $f_j = \frac{N_j}{N}$ [2.13]

In the above analysis, each phase has three unknowns; μ, σ, and f. The unknown variables are solved by minimizing the standard error between theoretical PDF and discrete PDF from indentation data set.

$$\text{Standard Error} = \sum_{\boldsymbol{i=1}}^{\boldsymbol{m}} \frac{(\boldsymbol{P_i - P_{xi}})^2}{\boldsymbol{m}} \Rightarrow \textit{minimum}\text{ , subjected to } \sum_{\mathrm{j}=1}^{\mathrm{N}} \mathrm{f_j} = 1 \quad [2.14]$$

2.4.4. Continuous Stiffness Measurement

Continuous Stiffness measurement, CSM, technique imposes a small dynamic oscillation on force (or load) signal during loading of the indenter and measures the amplitude and phase of the

corresponding displacement (or force) signal (Oliver & Pharr, 2004). As the oscillation is restricted to one directional vertical motion, the system is modeled as a simple harmonic oscillator subjected to forced oscillation. The ordinary differential equation of such system is given by (MTS Lab reference manual),

$$\sum m\ddot{z} + D\dot{z} + Kz = F(t) \quad [2.15]$$

where K is the equivalent stiffness that includes stiffness of the contact, S, the load-frame stiffness K_f, and stiffness of the spring , K_s, such that

$$K = \left(\frac{1}{S} + \frac{1}{K_f}\right) + K_s \quad [2.16]$$

and D is the equivalent dashpot given as

$$D = D_i + D_s \quad [2.17]$$

where subscript i and s represent indenter and substrate respectively. Now for the forcing function of

$F(t) = F_0 e^{i\omega t}$ and resulting displacement function of type $z(t) = z_0 e^{i(\omega t - \phi)}$

where ϕ is the phase angle. Performing substitution and simultaneous solving of above equations finally gives the stiffness of the contact as

$$S = \left(\frac{1}{\frac{F_0}{z_0}\cos\phi - (K_s - m\omega^2)} + \frac{1}{K_f}\right) \quad [2.18]$$

Once the elastic stiffness of the contact S is determined continuously, modulus and hardness can be measured using Equation [2.1], [2.3], [2.4] and [2.7]. Therefore, using this technique, continuous derivation of modulus and hardness data with indentation is obtained. Further, CSM technique has additional benefits such as identification of precise initial contact, fast and reliable calibration of testing procedures etc. (Oliver & Pharr, 2004). However, CSM technique can also result in underestimation of measured load and displacement amplitude and thereby, modulus

and hardness, especially at small depths (Durst et al., 2007; Pharr et al., 2009). Anomalous response of CSM data at small depth is attributed mainly to large dynamic unloading, particularly for material with high E/H ratio and test performed at large displacement oscillation. Further, at small depth, due to dynamic unloading contact between indenter and specimen can be lost, known as tapping. Thus, the correct interpretation of indentation test using CSM technique warrants the prediction of tapping depth and corrections for load and displacement data for dynamic unloading conditions. A more prudent approach is to perform tests at small displacement oscillation amplitudes and verify test results with CSM option turned off and/or direct area measurement.

Thus, many research have utilized nanoindentation methods in the characterization of the elastic modulus and hardness of thin films and small volumes of material. This dissertation will focus on the anisotropy and indentation size effect in clay minerals (Chapter 3 and 4) and nanomechanical characterization of hybrid geomaterial (Chapter 6) using nanoindentation.

2.5. References

Basu, S., Zhou, A., & Barsoum, M. W. (2009). On spherical nanoindentations, kinking nonlinear elasticity of mica single crystals and their geological implications. *Journal of structural geology, 31*(8), 791-801. doi: 10.1016/j.jsg.2009.05.008

Bickmore, B. R., Nagy, K. L., Sandlin, P. E., & Crater, T. S. (2002). Quantifying surface areas of clays by atomic force microscopy. *American Mineralogist, 87*(5-6), 780-783.

Bobko, C., & Ulm, F.-J. (2008). The nano-mechanical morphology of shale. *Mechanics of Materials, 40*, 19.

Christoffersen, R., & Kronenberg, A. K. (1993). Dislocation interactions in experimentally deformed biotite. *Journal of structural geology, 15*(9), 1077-1095.

Comodi, P., & Zanazzi, P. F. (1995). High-pressure structural study of muscovite. *Physics and Chemistry of Minerals, 22*(3), 170-177. doi: 10.1007/bf00202297

Constantinides, G., Ravi Chandran, K. S., Ulm, F. J., & Van Vliet, K. J. (2006). Grid indentation analysis of composite microstructure and mechanics: Principles and validation. *Materials Science and Engineering: A, 430*(1–2), 189-202. doi: 10.1016/j.msea.2006.05.125

Constantinides, G., & Ulm, F.-J. (2007). The nanogranular nature of C–S–H. *Journal of the Mechanics & Physics of Solids, 55*(1), 64-90. doi: 10.1016/j.jmps.2006.06.003

Constantinides, G., Ulm, F.-J., & Vliet, K. V. (2003). On the use of nanoindentation for cementitious materials *Materials and Structures, 36*, 5.

Cook, L. E., & Pickering, F. G. (1968). *Kaolinite fillers in rubber*. Paper presented at the Rubber Meeting of Swedish Inst. Rubber Technology, Falsterbo

Cygan, R. T., Liang, J.-J., & Kalinichev, A. G. (2004). Molecular Models of Hydroxide, Oxyhydroxide, and Clay Phases and the Development of a General Force Field. *The Journal of Physical Chemistry B, 108*(4), 1255-1266. doi: 10.1021/jp0363287

Cyr, M., Idir, R., & Poinot, T. (2012). Properties of inorganic polymer (geopolymer) mortars made of glass cullet. *Journal of Materials Science, 47*(6), 2782-2797. doi: 10.1007/s10853-011-6107-2

Davidovits, J. (1991). Geopolymers. *Journal of Thermal Analysis and Calorimetry, 37*(8), 1633-1656. doi: 10.1007/bf01912193

Davydov, D., Jirásek, M., & Kopecký, L. (2011). Critical aspects of nano-indentation technique in application to hardened cement paste. *Cement and Concrete Research, 41*(1), 20-29. doi: 10.1016/j.cemconres.2010.09.001

Delafargue, A., & Ulm, F. J. (2004). Explicit approximations of the indentation modulus of elastically orthotropic solids for conical indenters. *International Journal of Solids and Structures, 41*(26), 7351-7360. doi: 10.1016/j.ijsolstr.2004.06.019

Dera, P., Prewitt, C. T., Japel, S., Bish, D. L., & Johnston, C. T. (2003). Pressure-controlled polytypism in hydrous layered materials. *American Mineralogist, 88*(10), 1428-1435.

Doerner, M. F., & Nix, W. D. (1986). A method for interpreting the data from depth-sensing indentation instruments. *Journal of Materials Research, 1*.

Durst, K., Franke, O., Boehner, A., & Goeken, M. (2007). Indentation size effect in Ni-Fe solid solutions. *Acta Materialia, 55*(20), 6825-6833. doi: 10.1016/j.actamat.2007.08.044

Duxson, P., Fernández-Jiménez, A., Provis, J. L., Lukey, G. C., Palomo, A., & Deventer, J. S. J. (2007). Geopolymer technology: the current state of the art. *Journal of Materials Science, 42*(9), 2917-2933. doi: 10.1007/s10853-006-0637-z

Duxson, P., Provis, J. L., Lukey, G. C., Mallicoat, S. W., Kriven, W. M., & van Deventer, J. S. J. (2005). Understanding the relationship between geopolymer composition, microstructure and mechanical properties. *Colloids and Surfaces A: Physicochemical and Engineering Aspects, 269*(1–3), 47-58. doi: 10.1016/j.colsurfa.2005.06.060

Fernández-Jiménez, A., & Palomo, A. (2005). Composition and microstructure of alkali activated fly ash binder: Effect of the activator. *Cement and Concrete Research, 35*(10), 1984-1992. doi: 10.1016/j.cemconres.2005.03.003

Grutzeck, M. W., Hoyle, S., Kwan, S., LaRosa, J., & Bozich, S. (1991). Microstructure, porosity and mechanical property relationships of calcium-silicate-hydrate (pp. 117): Pennsylvania State University, Park Materials Research Lab.

Gu, B., & Doner, H. E. (1992). The interaction of polysaccharides with silver hill illite. *Clays and Clay Minerals, 40*(2), 6. doi: 10.1346/CCMN.1992.0400203

Guggenheim, S., Adams, J. M., Bain, D. C., Bergaya, F., Brigatti, M. F., Drits, V. A., . . . Stanjek, H. (2006). Summary of recommendations of nomenclature committees relevant to clay mineralogy: report of the Association Internationale pour l'Etude des Argiles (AIPEA) Nomenclature Committee for 2006. *Clay Minerals, 41*(4), 863-877. doi: 10.1180/0009855064140225

Guggenheim, S., Adams, J. M., Bain, D. C., Bergaya, F., Brigatti, M. F., Drits, V. A., . . . Stanjek, H. (2007). Summary of recommendations of Nomenclature Committees Relevant to Clay Mineralogy: Report of the Association Internationale pour l'Etude des Argiles (AIPEA) Nomenclature Committee for 2006 (vol 42, pg no 575, 2007). *Clay Minerals, 42*(4), 575-576. doi: 10.1180/claymin.2007.042.4.13

Guggenheim, S., & Martin, R. T. (1995). Definition of clay and clay mineral: Joint report of the AIPEA nomenclature and CMS nomenclature committees. *Clays and Clay Minerals, 43*(2), 255-256. doi: 10.1346/ccmn.1995.0430213

Harvey, C. A., & Lagaly, G. (2006). Conventional Applications. In B. F, T. B.K.G & L. G (Eds.), *Handbook of Clay Science* (pp. 1246): Elsevier Science.

Hazen, R. M., & Finger, L. W. (1978). Crystal structures and compressibilities of layer minerals at high pressure. II. phlogopite and chlorite. *American Mineralogist, 63*, 293-296.

Igarashi, S., Bentur, A., & Mindess, S. (1996). Microhardness Testing of Cementitious Materials *Advance Cement Based Materials, 4*, 9.

J.S, F., & Swain, M. V. (1995). Determining the mechanical properties of small volumes of material from submicrometer spherical indentations. *J. Mater. Res, 10*(1), 12.

Jennings, H. M. (2000). A model for the microstructure of calcium silicate hydrate in cement paste. *Cement and Concrete Research, 30*(1), 101-116. doi: 10.1016/s0008-8846(99)00209-4

Jennings, H. M., Thomas, J. J., Gevrenov, J. S., Constantinides, G., & Ulm, F.-J. (2007). A multi-technique investigation of the nanoporosity of cement paste. *Cement and Concrete Research, 37*(3), 329-336. doi: 10.1016/j.cemconres.2006.03.021

Johnson, K. L. (1985). *Contact mechanics*: Cambridge University Press.

Joly, S., Garnaud, G., Ollitrault, R., Bokobza, L., & Mark, J. E. (2002). Organically Modified Layered Silicates as Reinforcing Fillers for Natural Rubber. *Chemistry of Materials, 14*(10), 4202-4208. doi: 10.1021/cm020093e

Kosoglu, L. M., Bickmore, B. R., Filz, G. M., & Madden, A. S. (2010). ATOMIC FORCE MICROSCOPY METHOD FOR MEASURING SMECTITE COEFFICIENTS OF FRICTION. *Clays and Clay Minerals, 58*(6), 813-820. doi: 10.1346/ccmn.2010.0580609

Kriven, W. M., Bell, J. L., & Gordon, M. (2006). Microstructure and Microchemistry of Fully-Reacted Geopolymers and Geopolymer Matrix Composites *Advances in Ceramic Matrix Composites IX* (pp. 227-250): John Wiley & Sons, Inc.

Krivenko, P. (1994). Alkaline cements. In K. PV (Ed.), *Proceedings of the first international conference on alkaline cements, concretes* (pp. 11-129). Kiev, Ukraine: VIPOL Stock Company.

Krivenko, P., & Kovalchuk, G. (2007). Directed synthesis of alkaline aluminosilicate minerals in a geocement matrix. *Journal of Materials Science, 42*(9), 2944-2952. doi: 10.1007/s10853-006-0528-3

Kroner, E. (1967). Elastic moduli of perfectly disordered composite materials. *Journal of the Mechanics and Physics of Solids., 15*, 11.

Lan, T., Kaviratna, P. D., & Pinnavaia, T. J. (1995). Mechanism of Clay Tactoid Exfoliation in Epoxy-Clay Nanocomposites. *Chemistry of Materials, 7*(11), 2144-2150. doi: 10.1021/cm00059a023

Manevitch, O. L., & Rutledge, G. C. (2003). Elastic Properties of a Single Lamella of Montmorillonite by Molecular Dynamics Simulation. *The Journal of Physical Chemistry B, 108*(4), 1428-1435. doi: 10.1021/jp0302818

Mavko, G., Mukerji, T., & Dvorkin, J. (1998). *The Rock Physics Handbook. Tools for Seismic Analysis in Porous Media.* Cambridge, New York: Cambridge University Press.

McNeil, L. E., & Grimsditch, M. (1993). Elastic moduli of muscovite mica. *Journal of Physics: Condensed Matter, 5*(11), 1681.

Mencik, J., Munz, D., Quandt, E., Weppelmann, E. R., & Swain, M. V. (1997). Determination of elastic modulus of thin layers using nanoindentation. *Journal of Materials Research, 12*(9), 2475-2484. doi: 10.1557/jmr.1997.0327

Mitchell, J. K., & Soga, K. (2005). *Fundamentals of Soil Behavior* (3 ed.). New Jersey: John Wiley & Sons, Inc.

Mondol, N. H., Jahren, J., Bjorlykke, K., & Brevik, I. (2008). Elastic properties of clay minerals. . *The Leading Edge, 27*, 13.

Němeček, J., Šmilauer, V., & Kopecký, L. (2011). Nanoindentation characteristics of alkali-activated aluminosilicate materials. *Cement and Concrete Composites, 33*(2), 163-170. doi: 10.1016/j.cemconcomp.2010.10.005

Oliver, W. C., & Pharr, G. M. (1992). An improved technique for determining hardness and elastic-modulus using load and displacement sensing indentation experiments *Journal of Materials Research, 7*(6), 1564-1583. doi: 10.1557/jmr.1992.1564

Oliver, W. C., & Pharr, G. M. (2004). Measurement of hardness and elastic modulus by instrumented indentation: Advances in understanding and refinements to methodology. *Journal of Materials Research, 19*(1), 3-20. doi: 10.1557/jmr.2004.19.1.3

Palomo, A., & López dela Fuente, J. I. (2003). Alkali-activated cementitous materials: Alternative matrices for the immobilisation of hazardous wastes: Part I. Stabilisation of boron. *Cement and Concrete Research, 33*(2), 281-288. doi: 10.1016/s0008-8846(02)00963-8

Pawley, A. R., Clark, S. M., & Chinnery, N. J. (2002). Equation of state measurements of chlorite, pyrophyllite, and talc. *American Mineralogist, 87*(8-9), 1172-1182.

Pawley, A. R., Redfern, S. A. T., & Wood, B. J. (1995). Thermal expansivities and compressibilities of hydrous phases in the system MgO-SiO2-H2O: Talc, phase A and 10-angstrom phase. . *Contributions to Mineralogy and Petrology, 122*, 301-307.

Pharr, G. M., Oliver, W. C., & Brotzen, F. R. (1992). On the generality of the relationship among contact stiffness, contact area, and elastic modulus during indentation. *Journal of Materials Research, , 7* 4. doi: 10.1557

Pharr, G. M., Strader, J. H., & Oliver, W. C. (2009). Critical issues in making small-depth mechanical property measurements by nanoindentation with continuous stiffness measurement. *Journal of Materials Research, 24*(3), 653-666. doi: 10.1557/jmr.2009.0096

Piner, R. D., Xu, T. T., Fisher, F. T., Qiao, Y., & Ruoff, R. S. (2003). Atomic Force Microscopy Study of Clay Nanoplatelets and Their Impurities. *Langmuir, 19*(19), 7995-8001. doi: 10.1021/la0347814

Ploehn, H. J., & Liu, C. (2006). Quantitative Analysis of Montmorillonite Platelet Size by Atomic Force Microscopy. *Industrial & Engineering Chemistry Research, 45*(21), 7025-7034. doi: 10.1021/ie051392r

Prasad, M., Kopycinska, M., Rabe, U., & Arnold, W. (2002). Measurement of Young's modulus of clay minerals using atomic force acoustic microscopy. *Geophys. Res. Lett., 29*(8), 1172. doi: 10.1029/2001gl014054

Prusinski, J., & Bhattacharja, S. (1999). Effectiveness of Portland Cement and Lime in Stabilizing Clay Soils. *Transportation Research Record: Journal of the Transportation Research Board, 1652*(-1), 215-227. doi: 10.3141/1652-28

Rahier, H., Mele, B., Biesemans, M., Wastiels, J., & Wu, X. (1996). Low-temperature synthesized aluminosilicate glasses. *Journal of Materials Science, 31*(1), 71-79. doi: 10.1007/bf00355128

Richardson, I. G. (2004). Tobermorite/jennite- and tobermorite/calcium hydroxide-based models for the structure of C-S-H: applicability to hardened pastes of tricalcium silicate, β-dicalcium silicate, Portland cement, and blends of Portland cement with blast-furnace slag, metakaolin, or silica fume. *Cement and Concrete Research, 34*(9), 1733-1777. doi: 10.1016/j.cemconres.2004.05.034

Richardson, I. G., & Groves, G. W. (1993). Microstructure and microanalysis of hardened ordinary Portland cement pastes. *Journal of Materials Science, 28*(1), 265-277. doi: 10.1007/bf00349061

Sakulich, A. R., & Li, V. C. (2010). Nanoscale characterization of engineered cementitious composites (ECC). *Cement and Concrete Research, 41*, 7.

Sato, H., Yamagishi, A., & Kawamura, K. (2001). Molecular Simulation for Flexibility of a Single Clay Layer. *The Journal of Physical Chemistry B, 105*(33), 7990-7997. doi: 10.1021/jp004491l

Seo, Y. S., Ichikawa, Y., & Kawamra, K. (1999). Stress-strain response of rock forming minerals by molecular dynamics simulation. *Mater. Sci. Res. Int., 5*(1), 13.

Shea, W. T., & Kronenberg, A. (1992). Rheology and Deformation Mechanisms of an Isotropic Mica Schis. *Journal of Geophysical Research,, 97*, 37.

Sneddon, I. N. (1965). The relation between load and penetration in the axisymmetric Boussinesq problem for a punch of arbitrary profile. *International Journal of Engineering Science, 3*, 10.

Sofi, M., Deventer, J. S. J., Mendis, P. A., & Lukey, G. C. (2007). Bond performance of reinforcing bars in inorganic polymer concrete (IPC). *Journal of Materials Science, 42*(9), 3107-3116. doi: 10.1007/s10853-006-0534-5

Swadener, J. G., & Pharr, G. M. (2001). Indentation of elastically anisotropic half-spaces by cones and parabolae of revolution. *Philosophical Magazine A, 81*(2), 447-466. doi: 10.1080/01418610108214314

Tai, K., Ulm, F.-J., & Ortiz, C. (2006). Nanogranular Origins of the Strength of Bone. *Nano Letters, 6*(11), 2520-2525. doi: 10.1021/nl061877k

Teich-McGoldrick, S. L., Greathouse, J. A., & Cygan, R. T. (2012). Molecular Dynamics Simulations of Structural and Mechanical Properties of Muscovite: Pressure and Temperature Effects. *The Journal of Physical Chemistry C, 116*(28), 15099-15107. doi: 10.1021/jp303143s

Theng, B. (1970). Interaction of clay minerals with organic polymers. Some practical applications. *Clays and Clay Minerals, 18*(16), 6.

Theng, B. K. G. (2012). *Formation and properties of clay-polymer complexes* (2 ed. Vol. 4): Elsevier.

Theng, B. K. G., & Walker, G. F. (1970). Interactions of clay minerals with organic monomers. *Israel Journal of Chemistry, 8*, 417-424.

Ulm, F.-J., & Abousleiman, Y. (2006). The nanogranular nature of shale. *Acta Geotechnica, 1*(2), 77-88. doi: 10.1007/s11440-006-0009-5

Ulm, F.-J., Vandamme, M., Bobko, C., Alberto Ortega, J., Tai, K., & Ortiz, C. (2007). Statistical Indentation Techniques for Hydrated Nanocomposites: Concrete, Bone, and Shale. *Journal of the American Ceramic Society, 90*(9), 2677-2692. doi: 10.1111/j.1551-2916.2007.02012.x

Uskov, I. A., Galinskaya, V. I., & Artyukh, L. V. (1966). Calorimetric method of determining the interaction energy of polymers with fillers. *Polymer Science U.S.S.R., 8*(10), 2048. doi: http://dx.doi.org/10.1016/0032-3950(66)90334-0

Vanorio, T., Prasad, M., & Nur, A. (2003). Elastic properties of dry clay mineral aggregates,suspensions and sandstones. *Geophysical Journal International, 155*, 8.

Vaughan, M. T., & Guggenheim, S. (1986). Elasticity of Muscovite and Its Relationship to Crystal Structure. *J. Geophys. Res., 91*(B5), 4657-4664. doi: 10.1029/JB091iB05p04657

Velez, K., Maximilien, S., Damidot, D., Fantozzi, G., & Sorrentino, F. (2001). Determination by nanoindentation of elastic modulus and hardness of pure constituents of Portland cement clinker. *Cement and Concrete Research, 31*(4), 555-561. doi: 10.1016/s0008-8846(00)00505-6

Vlassak, J. (1993). Indentation modulus of elastically anisotropic half spaces. *Philosophical Magazine A, 67*(5), 1045-1056.

Vlassak, J. J., Ciavarella, M., Barber, J. R., & Wang, X. (2003). The indentation modulus of elastically anisotropic materials for indenters of arbitrary shape. *Journal of the mechanics and physics of solids, 51*(9), 1701-1721. doi: 10.1016/s0022-5096(03)00066-8

Vlassak, J. J., & Nix, W. D. (1994). Measuring the elastic properties of anisotropic materials by means of indentation experiments. *Journal of the mechanics and physics of solids, 42*(8), 1223-1245.

Wang, Z., Wang, H., & Cates, M. E. (2001). Effective elastic properties of solid clays. *Geophysics, 66*, 13.

Wei, Z. (2009). Nanoindentation behavior of clay minerals and clay-based nanostructured multilayers (pp. 192): Lousiana State University.

Yip, C. K., Lukey, G. C., & van Deventer, J. S. J. (2005). The coexistence of geopolymeric gel and calcium silicate hydrate at the early stage of alkaline activation. *Cement and Concrete Research, 35*(9), 1688-1697. doi: 10.1016/j.cemconres.2004.10.042

Zanazzi, P. F., Montagnoli, M., Nazzareni, S., & Comodi, P. (2007). Structural effects of pressure on monoclinic chlorite: A single-crystal study. *American Mineralogist, 92*(4), 655-661. doi: 10.2138/am.2007.2341

Zbik, M., & Smart, R. S. C. (1998). Nanomorphology of kaolinites; comparative SEM and AFM studies. *Clays and Clay Minerals, 46*(2), 153-160.

Zhang, G., Wei, Z., & Ferrell, R. E. (2009). Elastic modulus and hardness of muscovite and rectorite determined by nanoindentation. *Applied Clay Science, 43*(2), 271-281. doi: 10.1016/j.clay.2008.08.010

Zhang, G., Wei, Z., Ferrell, R. E., Guggenheim, S., Cygan, R. T., & Luo, J. (2010). Evaluation of the elasticity normal to the basal plane of non-expandable 2:1 phyllosilicate minerals by nanoindentation. *American Mineralogist, 95*(5-6), 863-869. doi: 10.2138/am.2010.3398

Chapter 3. Elastic-Plastic Anisotropy of Muscovite Probed by Nanoindentation

3.1. Introduction

Clays and other phyllosiliate minerals consist of fundamental 1:1 layers of 0.7 nm in thickness or 2:1 layers of 1.0 nm thickness with sub-nanometer interlayer spacing usually occupied by hydrated or nonhydrated cations. For these minerals, usually, the interactions between interlayer cations and the fundamental 1:1 or 2:1 layers are much weaker than the atomic bonds between atoms within the layers, and hence play a key role in controlling the elastic and plastic properties (Zhang et al., 2010). Several factors such as the layer charge, *z*, structural and compositional variations, and interlayer spacing are found to influence their elastic modulus. Because of the distinct layered structure, phyllosilicates are expected to exhibit elastic and plastic anisotropy. However, the tiny size of individual clay crystals imposes a significant challenge to the experimental determination of elastic and plastic properties. Past research on mechanical properties of phyllosilicates used techniques such as Brillouin spectroscopy, X-ray or neutron diffraction, ultrasonic measurements, and more recently molecular dynamics simulation.

A nanomechanical testing method, nanoindentation, has been utilized to assess elastic and plastic properties of metals, ceramics, thin films and biological specimens. Following the theoretical framework of Vlassak (1993), Vlassak et al. (2003), Swadener and Pharr (2001), Delafargue and Ulm (2004) and others, nanoindentation technique has been further extended to study anisotropy of metals, bones and clay minerals. Similarly, elastic modulus of well-ordered mica and rectorite specimens showed good agreement between experimental and theoretical values for indentation modulus normal to basal plane (Zhang et al., 2009). In the current research, we have extended the previous work on nanoindentation characterization of muscovite by performing indentation on mica along loading directions both normal and parallel to the basal

plane, thereby examining the anisotropy in these two directions. This chapter presents the details of the elastic-plastic properties of mica probed by nanoindentation.

3.2. Materials and Methods

V1-grade muscovite specimens of 15 x 15 x 0.15-0.3 mm (length x width x thickness) were obtained from Axim Mica, New York, USA. V1-grade denotes the highest grade of mica that are clear, transparent, nearly flat, free from stains, foreign inclusions, cracks and other similar defects (ASTM-D351, 2008). Samples were clear to translucent with slight brownish hue and show negligible particle or air inclusions. For indentation normal to basal plane, samples were prepared using the procedure described in (Zhang et al., 2009). Samples for indentation parallel to the basal plane were prepared by mechanically polishing the vertical edge of the mica specimen encapsulated in a castable resin mix (EpoKwick, Buehler, USA). Indentations were performed by selecting flat surfaces; devoid of any mechanical distress or delamination that may have occurred during polishing. Strict quality control routine were observed which include area function calibration, tip cleaning and indentation on fused silica in between test, as described in the reference. Nanoindentation tests were performed using MTS XP indenter (MTS Nano instruments Inc., Oak Ridge, Tennessee) at ambient condition. An XP indenter equipped with Berkovich tip with a tip radius <20 nm was used to indent under the continuous stiffness measurement (CSM) mode at a constant indentation strain rate ($\dot{h}/h$) of 0.05 s^{-1} where h is indentation depth. CSM mode involved the superimposing of a displacement controlled harmonic loading with frequency of 45 Hz and amplitude of 1 nm.

The harmonic contact stiffness, S, was derived continuously during loading by imposing oscillating displacement and measuring amplitude and phase of the corresponding force (Oliver

& Pharr, 2004). Indentation modulus, M, (also referred as reduced elastic modulus, E_r, in literature) and hardness, H, were obtained as

$$M = \frac{\sqrt{\pi}}{2\beta\sqrt{A_c}}S \quad [3.1]$$

$$H = \frac{F_{max}}{A_c} \quad [3.2]$$

where β is a dimensionless factor for the indenter tip shape correction and β=1.05 is commonly used for Berkovich indenter (Oliver & Pharr, 2004), F_{max} is maximum indentation load at unloading, and A_c is the projected contact area between indenter and sample, which can be obtained solely using indentation parameters (Oliver & Pharr, 2004; Sneddon, 1965).

Indentation fracture toughness (K_{IC}) was determined using the method developed by (Anstis et al., 1981). This method relates the length of the cracks to K_{IC} as follows:

$$K_{IC} = \alpha\left(\frac{E}{H}\right)^{1/2}\left(\frac{F_{max}}{C^{3/2}}\right) \quad [3.3]$$

where α is an empirical constant depending on the geometry of the indenter. For Vickers and Berkovich indenter, α=0.016 is found to give good correlation between toughness measured using crack length measurement (Anstis et al., 1981; Pharr et al., 1993) and those obtained using conventional method (Lawn, 1993). Both E and H were obtained from the indentation data. The crack length was measured from the center of the indent to end of the crack using scanning electron microscope (SEM). For each indent using Berkovich indenter, an average of three radial cracks was taken to determine the crack length, c.

3.3. Analysis of Results

3.3.1. Load Displacement Curves

Figure 3.1 shows the load-displacement curves for both indentation directions. It is evident that the resistance to penetration is remarkably different in the two directions. First, higher

resistance to penetration is observed for the loading direction normal to the basal plane than that parallel to it. Second, randomly occurring displacement bursts or pop-ins are more pronounced in the indentations normal to the basal plane. One or more micrometer-sized pop-in occurred randomly, which are followed by several nanometer-sized pop-ins in between. In contrast, load displacement curves on edge are populated with small displacement bursts ranging a few nanometers. Suppression of large pop-ins on edge surface may insinuate surface deformation at first glance; however, comparable threshold load and pop-in size at small displacements (Fig. 1 inset) imply that insignificant residual stress or deformation is present within the specimen (Wang et al. 2011). Although, two faces are expected to behave distinctly, pop-in size and load can be fairly comparable at this range. It is noteworthy that the cleaving technique used in sample preparation is expected to impart very little surface deformation or additional dislocations (Christoffersen & Kronenberg, 1993). Therefore, the load-displacement curves show characteristic indentation features in two mutually perpendicular directions (Pant et al., 2013).

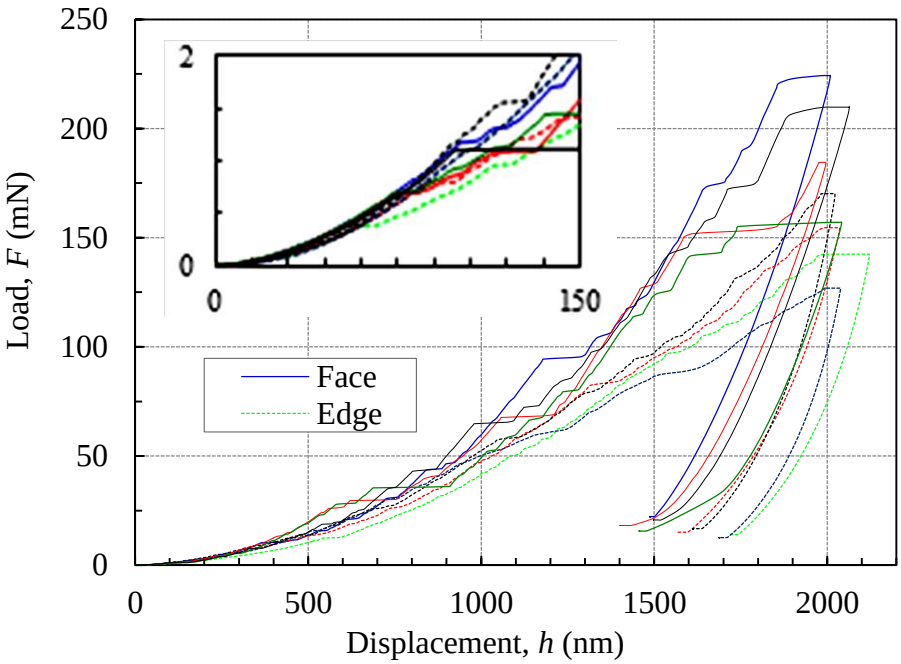

Figure 3.1: Indentation load-displacement curves of muscovite specimen.

Figures 3.2a and 3.2b show the typical residual imprints for two indentation directions. Indentation imprint on face surface is more symmetrical, while the imprint on edge surface is distinctly elongated. Relics of abrupt cracking, layer delaminations, spallation, and significant surface damage under the indenter are clearly visible, which are also reflected as discontinuities in the load-displacement curves. Also, kink boundaries and material pile-up around the imprint were observed. Comparatively, indentation imprint on the edge shows little pile-up, but visible cracks in the direction along the basal place. It may also be possible that some of these cracks may have closed after the load removal. Nevertheless, unlike on the basal plane, indentation impression boundaries on edge are sharply defined.

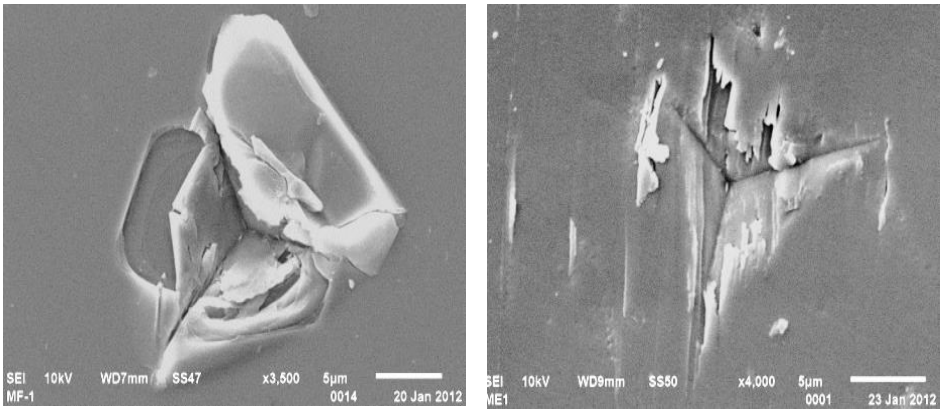

3.2 a) 3.2b)

Figure 3.2: SEM images showing the residual indents: a) face and b) edge

Another interesting feature, more prominent in the indentation normal to basal plane, is identical elastic-plastic resistance curve, following pop-ins. In other words, individual curve represents a single elasto-plastic curve separated by horizontal plastic displacement due to pop-ins. It has been shown in various studies that this elastoplastic curve can be described by relationship

$$F = Kh^2 \qquad [3.4]$$

where constant *K* depends on shape of indenter tip and material properties of indented material.

For a perfect Berkovich indenter, *K* can be expressed as (Hainsworth et al., 1996; Malzbender et al., 2000),

$$F = M\left(\frac{1}{\sqrt{24.5}}\sqrt{\frac{M}{H}} + \varepsilon\sqrt{\frac{\pi}{4}}\sqrt{\frac{H}{M}}\right) \qquad [3.5]$$

where ε =0.72 for conical indenter.

Figure 3.3 shows the plot of $\Delta F/\Delta h$ versus displacement for indentation on fused silica standard. In case of the fused silica standard, where no pop-ins occur, all data points corresponding to five representative tests plot in a narrow band forming a straight trend line, slope of which is equal to two times K, as defined in equation [3.4].

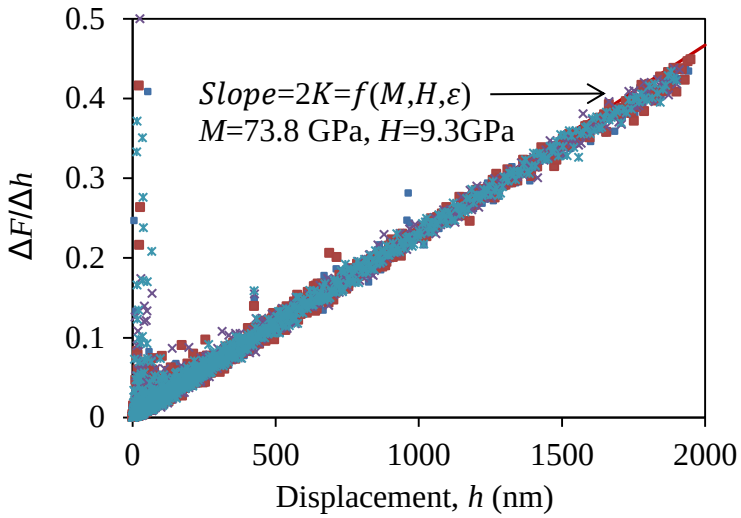

Figure 3.3: $\Delta F/\Delta h$ versus *h* plot for fused silica standard.

Figures 3.4a and 3.4b show the plot of $\Delta F/\Delta h$ versus displacement for indentation on mica face and mica edge respectively. In case of mica samples, data points plot in a cluster in between two straight lines. It should be noted that $\Delta F/\Delta h$ obtained in this manner are not exactly zero, even for large discernible pop-ins, due to data acquisition method. Therefore, simple data filter routine was employed where any Δh significantly greater than local trend were identified as pop-ins and thus removed. Again, for mica face and mica edge indentations, slopes of upper bound

and lower bound lines are given by [3.4] corresponding to M/H at peak and M/H average respectively.

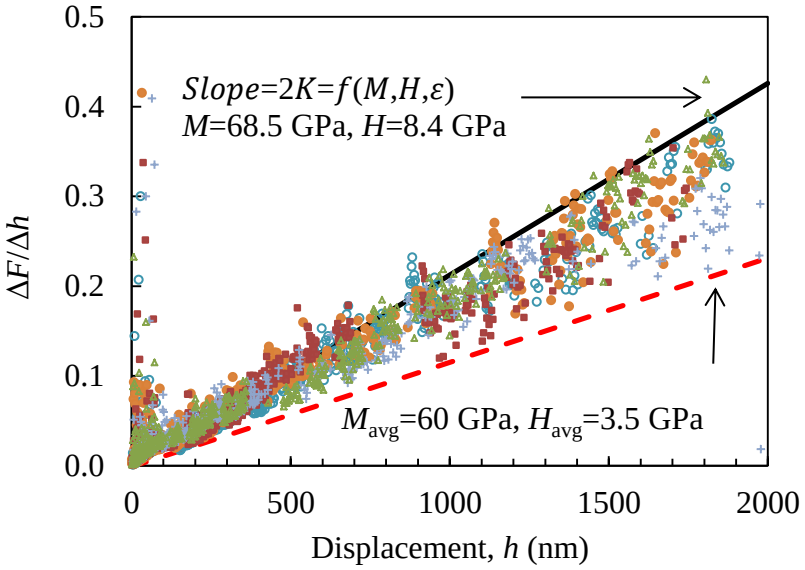

3.4a)

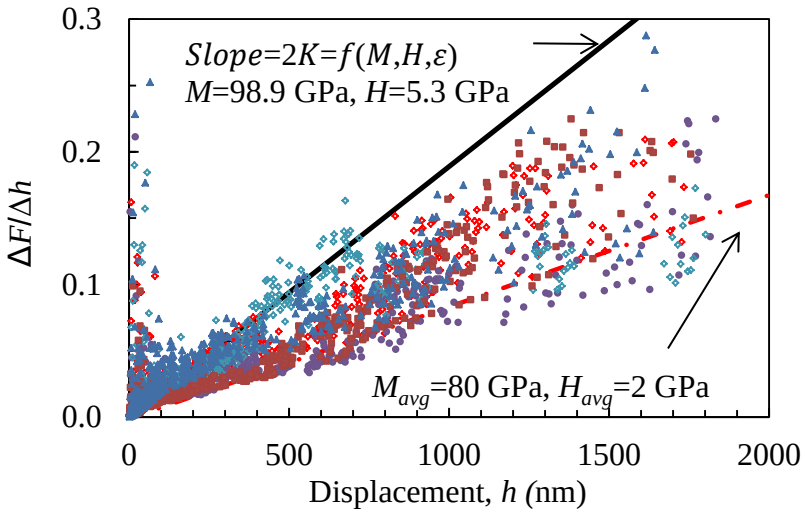

3.4b)

Figure 3.4: $\Delta F/\Delta h$ versus h plot for a) Mica Face b) Mica Edge sample.

3.3.2. Indentation Modulus

Figure 3.5 shows the indentation moduli averaged from multiple tests with the error bars representing one standard deviation. In plane indentation moduli (M_E) is higher than out of plane

indentation modulus (M_F). Also, indentation moduli in both directions show a gradual decrease with depth after an initial peak.

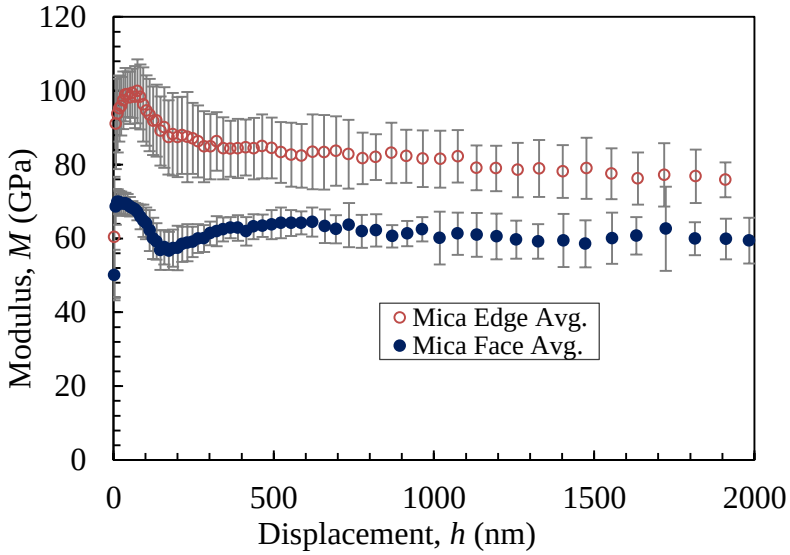

Figure 3.5: Relationship between indentation modulus and depth.

3.3.3.Hardness

Figure 3.6 shows the plot of hardness versus depth for indentations normal to basal plane and parallel to edges. As seen in the figure, hardness measured along both directions shows an apparent indentation size effect (ISE); hardness increases with decrease in depth. The hardness curve normal to basal plane exhibits some interesting features. First, hardness decreases rapidly with indentation, after the initial peak, up to the depth of 150-160 nm. However, in between 150-500 nm average hardness remains constant or rises subtly. Beyond 500 nm to micro range, hardness again decreases with depth. In contrast, hardness measured parallel to basal plane decreases uniformly. It is noteworthy to mention that discontinuity in hardness curve measured normal to basal plane is not an artifact due to area function; indentation were carried simultaneously in all samples with same indenter. Area function was calibrated in the beginning by indenting on standard fused silica and between each set of indentation on mica samples, tip

cleaning and indentation on standard fused silica was done to ensure validity of results. Effect of pop-in events and indentation depth on continuous hardness curves are more noticeable in the individual tests. Figure 3.7 shows a typical plot of load and hardness curves with depth. For indentation normal to basal plane, between pop-ins, hardness increases locally. However, beyond a depth of 500 nm, such phenomenon is indistinguishable. For the edge indentation, hardness curve appears relatively smooth throughout.

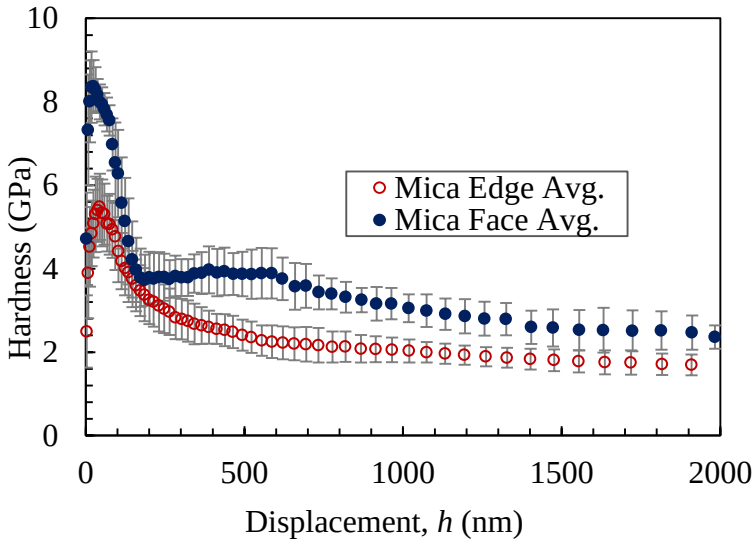

Figure 3.6: Relationships between hardness and depth.

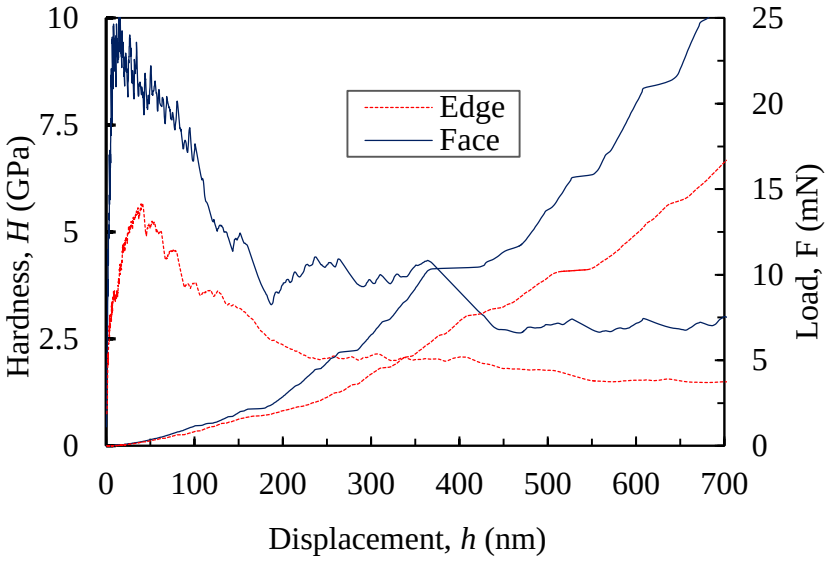

Figure 3.7: Hardness and load vs displacement curves.

3.3.4. Anisotropy

Mica has a monoclinic crystallographic structure with a weak cleavage plane parallel to basal plane. This imparts both elastic and plastic anisotropy to mica, verified in several experimental (Mares & Kronenberg, 1993; Vaughan & Guggenheim, 1986) and molecular dynamics (MD) simulation (Manevitch & Rutledge, 2003; Mazo et al., 2008) studies. Indentation along two mutually perpendicular directions gives both qualitative and quantitative assessment of anisotropy. Figures 3.2a and 3.2b show the typical residual imprints for two indentation directions. Indentation imprints on face surfaces are more symmetrical, while imprints on edge surfaces are distinctly elongated. Relics of abrupt cracking, layer delaminations, spalling, and significant surface damage under the indenter are clearly visible, that are also reflected as discontinuities in the load-displacement curves. Also, kink boundaries and material pile-up around the imprint can be noticed. Comparatively, indentation imprint on the edge shows little pile-up, but visible cracks in the direction along the basal place. It may also be possible that some of these cracks may have closed after the load removal. Nevertheless, unlike the basal plane, indentation impression boundaries of the edge indentation are sharply defined.

For the sake of simplicity, mica is modeled as transversely isotropic such that the axis of symmetry is normal to the basal plane. For transversely isotropic solid, indentation modulus in the direction of the axis of symmetry (normal to basal plane) is related to elastic constants, C_{ijkl},, (Elliott, 1949; Hanson, 1992),

$$M_F = 2\sqrt{\frac{C_{31}^2 - C_{13}^2}{C_{11}^2}\left(\frac{1}{C_{44}} + \frac{2}{C_{31}+C_{13}}\right)^{-1}} \qquad [3.6]$$

where C_{mn} are the fourth order elastic stiffness tensors (C_{ijkl}) expressed in reduced notations; $C_{1111}=C_{11}$, $C_{3333}=C_{33}$ $C_{2323}=C_{44}$ $C_{1133}=C_{13}$ C_{31}=SQRT($C_{11}C_{33}$) and $C_{12}= C_{1111}-2C_{1212}$. Similarly, the indentation modulus normal to axis of symmetry (parallel to basal plane) can be

approximately expressed in terms of elastic constant using explicit solution (Delafargue and Ulm, 2004),

$$M_E = \sqrt{\frac{c_{11}^2 - c_{12}^2}{c_{11}}} \sqrt{\frac{c_{44}}{c_{33}}} M_F \qquad [3.7]$$

Table 3.1 summarizes the elastic constants of muscovite cited in the literature and the calculated indentation modulus using above equations. Average experimental indentation moduli at peak value are M_F = 68.5GPa and M_E=99.0 GPa which gives anisotropy factor M_E/M_F=1.45. Similarly, average indentation modulus at unloading M_F=53.5GPa and M_E=72.1 GPa gives anisotropy M_E/M_F =1.35.

Table 3.1: Calculated indentation moduli and anisotropy

Elastic Constants (GPa)	(Vaughan & Guggenheim, 1986)	(McNeil & Grimsditch, 1993)	(Aleksandrov & Ryzhova, 1961)
C_{11}	181	176.5	178
C_{33}	58.6	60.9	55
C_{44}	16.5	15	12
C_{13}	25.6	20	15
C_{31}	103	103.7	98.9
C_{12}	48	48	42
M_F	53.7	53.2	46.2
M_E	126.1	121.7	118.14
Anisotropy M_E/M_F	2.35	2.29	2.56

3.3.5. Fracture Toughness

The indentation fracture toughness along the basal plane was found to be 0.38 MPa $m^{1/2}$. No prominent radial cracks could be resolved for indentation parallel to basal plane indicating either the ductile behavior parallel to basal plane or cracks were closed on the removal of the load. Figure 3.8 shows typical radial crack length, *c*, measurement using SEM image.

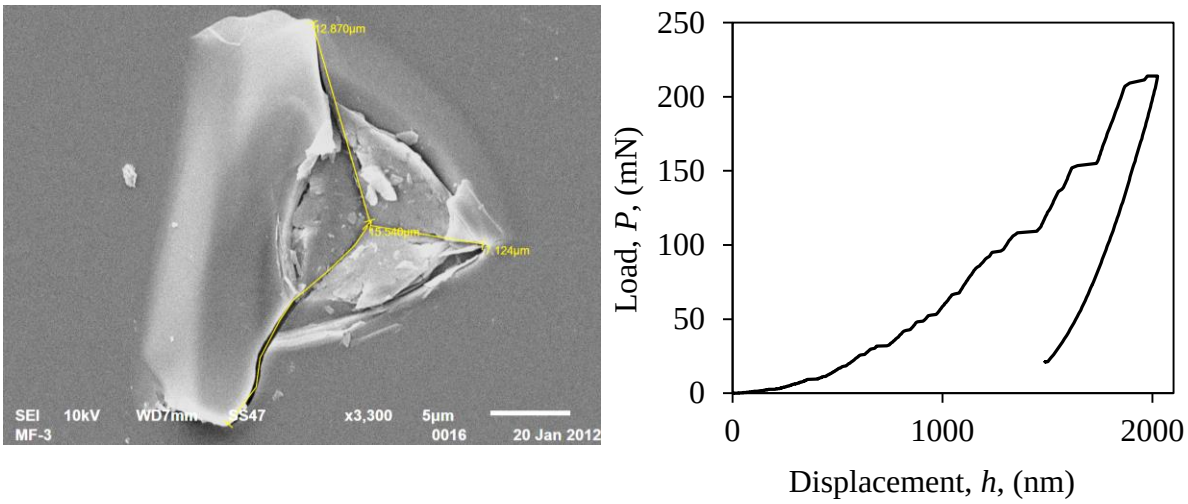

Figure 3.8: Typical residual indent normal to basal plane showing radial and lateral cracks. Load displacement curve is shown in the right.

3.4. Discussion

A distinct nanocrystalline structure of mica is clearly observed in nanoindentation experiment along two orthogonal directions. The different modes of nanoscale deformation are clearly reflected by the discontinuities in the load-displacement curves: giant pop-ins result from more abrupt cracking, layer delamination, and spallation, while the relatively smaller serrations are caused by relatively continuous, many small-step delaminations. Effect of these discontinuities is to shift elastoplastic load-displacement curve by horizontal plastic displacement. Similar observations were made in other studies on materials exhibiting pop-ins during nanoindentation loading (Basu et al., 2009; Tromas et al., 2006). Unlike in amorphous fused silica, slope of $\Delta F/\Delta h$ versus h is not constant for mica, which indicates variation of M/H with indentation depth. Also, the scatter in the data points is indicative of numerous nano size pop-ins that are continuously occurring during indentation. Again, larger scatter in data for edge indentation indicate that such this phenomenon is prominent for indentation along edges However, during continuous measurement of M and H, both parameters were found to decrease with depth. Generally, indentation modulus is expected to be a material property and thus depth

invariant, however, number of factors such as phase change under indenter, cracks, kinks and lattice disorientation may affect the material properties of equivalent volume that is sensed by indentation test. Decrease in hardness with depth is, also, due to indentation size effect (ISE), which is related to storage of dislocation densities (geometrically necessary dislocations, GNDs, and statistically stored dislocations, SSDs). Details of ISE are beyond the scope of this paper and are discussed elsewhere (Abu Al-Rub, 2007; Abu Al-Rub & Voyiadjis, 2004; Huang et al., 2006; Nix & Gao, 1998). However, artifacts of sample preparing method or area function error sometimes manifest as ISE in indentation test. However, deviation of $\Delta F/\Delta h$ data points from constant slope K is suggestive of ISE, such as in this experiment. Also, majority of data points fall between lines defined by upper and lower bound of M and H values during indentation.

Another interesting feature was revealed in the continuous plot of hardness versus depth. In case of face indentation, hardness rises locally between pop-ins and this effect is more prominent in the depth range of 200 nm to 500 nm. This region, as revealed in load-displacement curves, corresponds to several visible discontinuities in the load-displacement curve just before the onset of large micro size pop-in. During indentation, large crystals undergo domain change as new boundaries are defined by kink bands and cracks. Thus, once kink bands are formed, work required for nucleation of new IKBs and their propagation within these new subdomains imparts local hardening. Decrease in crystallite size is accompanied by a forest of micro cracks and voids caused by delaminations, thereby, facilitating easy slip and orientation of individual crystallites under indenter. Thus, whether the small step pop-ins following the large pop-in is caused by secondary kinks in these sub-domains or by slips and orientation of crystallites is the topic for further study. However, based on our observation of scatter in $\Delta F/\Delta h$ points, it is more likely the latter case. Thus, both indentation moduli and hardness decreases with indentation depth. It is

apparent that most of the material flow in edge indentation occurs by small step slip rather than abrupt bending and delamination following KBs. Thus the hardness curve is more or less smooth. This is also supported by large scatter in $\Delta F/\Delta h$ data points compared narrower band of basal indentation.

This study also observed plastic anisotropy as reflected in different hardness value measured for two orthogonal directions. Plastic behavior of well crystallized material is governed by dislocation density, dislocation interaction and active slip systems. In clay minerals such as mica, dislocations are restricted within glide plane i.e. basal plane and no cross slip or dislocation climb has been observed in mica. Therefore, the role of dislocation network, incipient kink band (IKB), and kink band (KB) is significant in affecting the deformation of mica (Barsoum et al., 2004; Zhang et al., 2010). These mechanisms are expected to be highly influenced by the orientation of crystal with respect to the principal deformation stress (Christoffersen & Kronenberg, 1993; Mares & Kronenberg, 1993), thus resulting in characteristic plastic anisotropy. Therefore, development of dislocation wall in to IKBs and subsequently to KBs result in flow normal to the basal plane, manifested as pile-up around the indent. The small pop-ins and serration in the load-displacement curves indicate that small step layer slips or formation of KBs are the main mechanisms of plastic flow.

M_F is 33% higher than the calculated modulus whereas the M_E is about 18% lower than the calculated value (Table 3.1), resulting in lower elastic anisotropy. However, lower elastic anisotropy was reported in others work (Bobko & Ulm, 2008; Ulm & Abousleiman, 2006). Cracks, lattice disorientation and phase transformation within the effective volume may influence the measure of mechanical property that is sensed by nanoindentation. Some variation in the result may also be inherent to simplistic transversely isotropic model for triclinic mica

structure. . Further, for kinking nonlinear elastic, KNE, material such as mica, IKBs which are fully reversible on unloading, contribute to unloading load-displacement curve. Therefore, indirect methods such as ultrasonic techniques or Brillouin scattering that exclude the role of IKBs are expected to produce different results than nanoindentation (Barsoum et al., 2004).

3.5. Conclusions

Indentation modulus measured normal to basal plane is smaller than that measured parallel to basal plane. Although, estimated indentation moduli from elastic constants, assuming transverse anisotropy, differ slightly from experimental values, anisotropy factor is comparable with results in other studies. Variability in the results may be attributed to sample to sample variations, assumption of simplified transverse anisotropy for triclinic structure of mica as well as other factors such as error in the alignment of sample, deformations and lattice disorientation during indentation. This study also found plastic anisotropy in mica, as evident from markedly differing penetration resistance and hardness along two mutually perpendicular directions.

3.6. References

Abu Al-Rub, R. K. (2007). Prediction of micro and nanoindentation size effect from conical or pyramidal indentation. *Mechanics of Materials, 39*(8), 787-802. doi: 10.1016/j.mechmat.2007.02.001

Abu Al-Rub, R. K., & Voyiadjis, G. Z. (2004). Analytical and experimental determination of the material intrinsic length scale of strain gradient plasticity theory from micro- and nano-indentation experiments. *International Journal of Plasticity, 20*(6), 1139-1182. doi: 10.1016/j.ijplas.2003.10.007

Aleksandrov, K. S., & Ryzhova, T. V. (1961). Elastic properties of rock-forming minerals II.Layered silicates. *Bull. Acad. Scie. USSR, Geophys. Ser. English translation 12* 1165–1168.

Anstis, G. R., Chantikul, P., Lawn, B. R., & Marshall, D. B. (1981). A Critical Evaluation of Indentation Techniques for Measuring Fracture Toughness: I, Direct Crack Measurements. *Journal of the American Ceramic Society, 64*(9), 533-538. doi: 10.1111/j.1151-2916.1981.tb10320.x

ASTM-D351-97. (2008). *e1. Standard Classification for Natural Muscovite Block Mica and Thins Based on Visual Quality* (Vol. 10.1). West Conshohocken, PA: ASTM International www.astm.org.

Barsoum, M. W., Murugaiah, A., Kalidindi, S. R., & Zhen, T. (2004). Kinking Nonlinear Elastic Solids, Nanoindentations, and Geology. *Physical Review Letters, 92*(25), 255508.

Basu, S., Zhou, A., & Barsoum, M. W. (2009). On spherical nanoindentations, kinking nonlinear elasticity of mica single crystals and their geological implications. *Journal of structural geology, 31*(8), 791-801. doi: 10.1016/j.jsg.2009.05.008

Bobko, C., & Ulm, F.-J. (2008). The nano-mechanical morphology of shale. *Mechanics of Materials, 40*(4–5), 318-337. doi: 10.1016/j.mechmat.2007.09.006

Christoffersen, R., & Kronenberg, A. K. (1993). Dislocation interactions in experimentally deformed biotite. *Journal of structural geology, 15*(9), 1077-1095.

Delafargue, A., & Ulm, F. J. (2004). Explicit approximations of the indentation modulus of elastically orthotropic solids for conical indenters. *International Journal of Solids and Structures, 41*(26), 7351-7360. doi: 10.1016/j.ijsolstr.2004.06.019

Elliott, H. A. (1949). Axial symmetric stress distribution in aeolotropic hexagonal crystals-the problem of the plane and related problems. *Proc. Camb. Phil. Soc., 45*(4), 10.

Hainsworth, S. V., Chandler, H. W., & Page, T. F. (1996). Analysis of nanoindentation load-displacement loading curves. *Journal of Materials Research, 11*(8), 1987-1995.

Hanson, M. T. (1992). The Elastic Field for Conical Indentation Including Sliding Friction for Transverse Isotropy. *Journal of applied mechanics, 59*(2), 123-S130.

Huang, Y., Zhang, F., Hwang, K. C., Nix, W. D., Pharr, G. M., & Feng, G. (2006). A model of size effects in nano-indentation. *Journal of the mechanics and physics of solids, 54*(8), 1668-1686. doi: 10.1016/j.jmps.2006.02.002

Lawn, B. (1993). *Fracture of brittle solids* (2 ed.). Cambridge, UK: Cambridge University Press.

Malzbender, J., de With, G., & den Toonder, J. (2000). The P–h2 relationship in indentation. *Journal of Materials Research, 15*(5), 1209-1212.

Manevitch, O. L., & Rutledge, G. C. (2003). Elastic Properties of a Single Lamella of Montmorillonite by Molecular Dynamics Simulation. *The Journal of Physical Chemistry B, 108*(4), 1428-1435. doi: 10.1021/jp0302818

Mares, V., & Kronenberg, A. (1993). Experimental deformation of muscovite. *Journal of structural geology, 15*(9), 1061-1075.

Mazo, M. A., Manevitch, L. I., Gusarova, E. B., Shamaev, M. Y., Berlin, A. A., Balabaev, N. K., & Rutledge, G. C. (2008). Molecular Dynamics Simulation of Thermomechanical

Properties of Montmorillonite Crystal. 1. Isolated Clay Nanoplate. *The Journal of Physical Chemistry B, 112*(10), 2964-2969. doi: 10.1021/jp076022q

McNeil, L. E., & Grimsditch, M. (1993). Elastic moduli of muscovite mica. *Journal of Physics: Condensed Matter, 5*(11), 1681.

Nix, W. D., & Gao, H. (1998). Indentation size effects in crystalline materials: A law for strain gradient plasticity. *Journal of the mechanics and physics of solids, 46*(3), 411-425. doi: 10.1016/s0022-5096(97)00086-0

Oliver, W. C., & Pharr, G. M. (2004). Measurement of hardness and elastic modulus by instrumented indentation: Advances in understanding and refinements to methodology. *Journal of Materials Research, 19*(1), 3-20. doi: 10.1557/jmr.2004.19.1.3

Pant, R., Hu, L., & Zhang, G. (2013). Anisotropy of Mica Probed by Nanoindentation. In L. Laloui & A. Ferrari (Eds.), *Multiphysical Testing of Soils and Shales* (pp. 239-245): Springer Berlin Heidelberg.

Pharr, G. M., Harding, D. S., & Oliver, W. C. (1993). Measurement of Fracture Toughness in Thin Films and Small Volumes Using Nanoindentation Methods. In M. Nastasi, D. Parkin & H. Gleiter (Eds.), *Mechanical Properties and Deformation Behavior of Materials Having Ultra-Fine Microstructures* (Vol. 233, pp. 449-461): Springer Netherlands.

Sneddon, I. N. (1965). The relation between load and penetration in the axisymmetric Boussinesq problem for a punch of arbitrary profile. *International Journal of Engineering Science, 3*, 10.

Swadener, J. G., & Pharr, G. M. (2001). Indentation of elastically anisotropic half-spaces by cones and parabolae of revolution. *Philosophical Magazine A, 81*(2), 447-466. doi: 10.1080/01418610108214314

Tromas, C., Gaillard, Y., Woirgard, J., Gaillard, Dagger, & Y. (2006). Nucleation of dislocations during nanoindentation in MgO. *Philosophical magazine, 86*(33), 5595-5606.

Ulm, F.-J., & Abousleiman, Y. (2006). The nanogranular nature of shale. *Acta Geotechnica, 1*(2), 77-88. doi: 10.1007/s11440-006-0009-5

Vaughan, M. T., & Guggenheim, S. (1986). Elasticity of Muscovite and Its Relationship to Crystal Structure. *J. Geophys. Res., 91*(B5), 4657-4664. doi: 10.1029/JB091iB05p04657

Vlassak, J. (1993). Indentation modulus of elastically anisotropic half spaces. *Philosophical Magazine A, 67*(5), 1045-1056.

Vlassak, J. J., Ciavarella, M., Barber, J. R., & Wang, X. (2003). The indentation modulus of elastically anisotropic materials for indenters of arbitrary shape. *Journal of the mechanics and physics of solids, 51*(9), 1701-1721. doi: 10.1016/s0022-5096(03)00066-8

Zhang, G., Wei, Z., & Ferrell, R. E. (2009). Elastic modulus and hardness of muscovite and rectorite determined by nanoindentation. *Applied Clay Science, 43*(2), 271-281. doi: http://dx.doi.org/10.1016/j.clay.2008.08.010

Zhang, G., Wei, Z., Ferrell, R. E., Guggenheim, S., Cygan, R. T., & Luo, J. (2010). Evaluation of the elasticity normal to the basal plane of non-expandable 2:1 phyllosilicate minerals by nanoindentation. *American Mineralogist, 95*(5-6), 863-869. doi: 10.2138/am.2010.3398

Chapter 4. Indentation Size Effect in Muscovite Mica

4.1. Introduction

Increase in measured hardness with decreasing indenter size has been widely observed in several studies across the wide range of metals, alloys and polymers. Early work on metals and alloys showed the indenter size effect with respect to indenter diameter where hardness increased with decreasing indenter size. With the advent of instrumented indentation techniques in material science, interest on indentation size effect (ISE) was once again renewed; as it is well established that measured hardness increases with decrease in indentation depth. However, cause of ISE is still contentious. Some researcher attributed ISE to surface anomalies such strain hardened deformed layer due to surface preparation techniques (Liu & Ngan 2001) strong oxidized layer or artifact of indentation techniques itself (Pharr et al., 2010). In fact some studies found the opposite trend, where hardness decreases with depth. However, study of Swadener et al. (2002) showed that work hardening during indentation is separate from ISE and effect of two phenomena can be decoupled and therefore ISE is characteristic behavior of the material property rather than artifact or anomaly at shallow depth of indentation.

Several models have been proposed to define ISE in metals, alloys and polymers. Majority of the models routinely encountered in this area are dislocation based. Strain gradient plasticity theories that are founded on the geometrically necessary dislocation (GND) concept have given reasonable agreement with ISE prediction (Abu Al-Rub, 2007). Originally, Nix and Gao (1998) developed an ISE model that suggest linear dependence of the hardness with reciprocal of indentation depth. Several studies modified this model for tip roundness , limits on GND storage with depth (Feng & Nix, 2004; Huang et al., 2006), kinking and strain gradient and non-linear coupling of flow stress (Abu Al-Rub, 2007; Abu Al-Rub & Voyiadjis, 2004a, 2004b, 2006).

The following sections review the summary of the ISE models and their limitations.

4.2. Review of ISE Models

4.2.1. Strain Gradient Theory and Physical Material Length Scale (Nix & Gao (1998))

Nix and Gao (1998) model is based on the work of Stelmashenko et al. (1993) and Shell De Guzman et al. (1993). This model assumes that circular dislocation loops injected into the material by conical indenter are contained in hemisphere defined by contact radius a_c (Figure 4.1). Therefore, volume of GND from total line length of λ is given as

$$\rho_{GND} = \frac{\lambda}{V} = \frac{\frac{\pi h a_c}{b}}{\frac{2\pi a_p^3}{3}} = \frac{3}{2}\frac{h a_c}{b a_p^3} = \frac{3}{2}\frac{\tan^2\theta}{f^3 b h} \qquad [4.1]$$

where b is burger vector, $a_p = f a_c$ defines plastic hemisphere zone that contains GND. In the original Nix-Gao model, f=1.

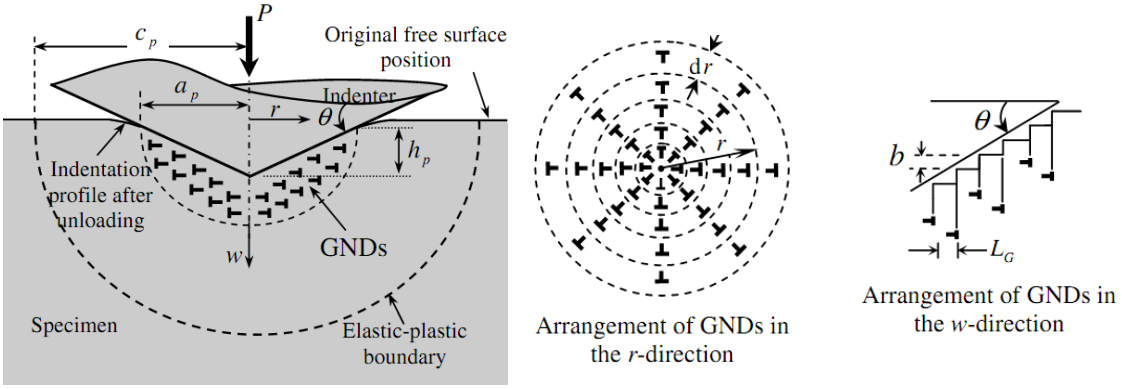

Figure 4.1: Geometrically necessary dislocation created during indentation by axissymetric conical indenter (adopted from Abu Al-Rub, 2007)

Relationship between macroscopic hardness and dislocation density is then derived based on Taylor (1938) relationship

$$\tau = \alpha G b\sqrt{\rho_T} = \alpha G b\sqrt{\rho_{SSD} + \rho_{GND}} \qquad [4.2]$$

where total dislocation density, ρ_T, is simply the sum of SSD and GND densities; G is shear modulus, and and α is statistical coefficient that asccounts for spatial deviation of SSD and

GND population. Kocks (1966) used $\alpha = 0.85$ for SSD and Busso et al. (2000) assumed $\alpha = 2.15$ for GND. However, for simplicity, same α is used for SSD and GND, with a range between 0.1 to 0.5.

Assuming von Misses flow rule ($\sigma = \sqrt{3}\tau$) and Tabor (1951) factor of 3 to convert flow stress to hardness ($H = 3\sigma$), indentation hardness can be expressed as

$$\frac{H}{H_0} = \sqrt{1 + \frac{h^*}{h}} \qquad [4.3]$$

such that $H_0 = 3\sqrt{3}Gb\sqrt{\rho_{SSD}}$ and $h^* = \frac{81}{2f^3} b\alpha^2 \tan^2\theta \left(\frac{G}{H_0}\right)^2$ [4.4]

where H_0 is hardness that arises from SSD alone; measured at large indentation depth ($h \gg h^*$). Thus, intrinsic length, h^* , scale based on Nix-Gao models is is not a constant for indenter rather depends on SSD through H_0 . In general, harder material exhibits small ISE as h^* is inversely proportional to H_0. Similarly, materials that contain higher dislocation density , such as work hardened during sample preparation, has smaller length scale and therefore exhibit low ISE. On the other hand, annealed specimen will have lower prior density and correspondingly exhibit higher ISE.

The concept of GND and depth dependence of hardness is attributed to the strain gradient plasticty. For conical indenters, strain gradient is of the form (Figure 4.1)

$$\chi = \frac{tan\theta}{a} \qquad [4.5]$$

Thus based on relation [4.2] and [4.3], this model propose the strain gradient plasticity law of the form

$$\left(\frac{\sigma}{\sigma_o}\right)^2 = 1 + b\left(\frac{G}{\sigma_o}\right)^2 \chi = 1 + \hat{l}\chi \qquad [4.6]$$

where $\hat{l}$ is the material length scale and changes with flow stress in the absence of strain gradient.

Microstructural interpretation of $\hat{l}$ can be explained considering the relation $\sigma_o = 3\sqrt{3}\alpha G b\sqrt{\rho_{SSD}}$ and $\rho_{SSD} = \frac{1}{L_s}$ where L_s is the mean spacing between SSD's.

$$\hat{l} = \frac{4}{3}\frac{L_s}{b} \quad [4.7]$$

Nix-Gao model provides an excellent description of ISE in the micrometer depth, however, fails to capture depth dependence in submicron and nanometer indentation depth range. Equation [4.3] suggests the linear dependence of hardness with inverse of root square indentation depth. However, recent experimental data showed significant deviation in nanoindentation. Several modifications have been suggested to account for this deviation at submicron and nano depth regime.

4.2.2. Non-linear Coupling of Flow Stress (Abu Al-Rub 2007, Abu Al-Rub and Voyiadzis 2004a, b)

Nix and Gao (1998) model assumes the linear coupling of dislocation densities (SSD and GND) to calculate flow stress using Taylor hardening law (Equation 4.2). This results in the underestimation of dislocation densities, particulary in shallow depth regime. Thus, Abu Al-Rub (2007), Abu Al-Rub and Voyiadjis (2004 a,b) proposed the non-linear coupling of flow stress such that

$$\sigma = \sigma_Y + \left(\sigma_{SSD}^{\beta} + \sigma_{GND}^{\beta}\right)^{1/\beta} \quad [4.8]$$

where β is the fitting factor and σ_Y is initial yeild stress. Thus, hardness is expressed as

$$H = \kappa\sigma = H_Y + \kappa m\alpha b G\left[\left(\rho_{SSD}\right)^{\beta/2} + \left(\rho_{GND}\right)^{\beta/2}\right]^{1/\beta} \quad [4.9]$$

where κ is Tabor factor (=3), m is von Misses factor ($\sqrt{3}$). For large depth, where effect of GND is negligible, hardness due to SSD alone is given as

$$H_0 = H_Y + \kappa m\alpha b G\sqrt{\rho_{SSD}} \quad [4.10]$$

From equations [4.8], [4.9] and [4.10]

$$\left(\frac{H-H_Y}{H_0-H_Y}\right)^{\beta} = 1 + \left(\frac{h^*}{h}\right)^{\beta/2} \quad [4.11]$$

$$h^* = \frac{3}{2f^3} b\kappa^2 m^2 \alpha^2 \tan^2\theta \left(\frac{G}{H_0-H_Y}\right)^2 \quad [4.12]$$

$$(H_0 - H_Y) = \kappa\sigma_0 c^{1/n} (\tan\theta)^{1/n}$$

where σ_0 measure of yield strength in uniaxial test, n is hardening exponent($n \geq 1$), c is material constant (0.2 to 0.4). Thus for n=2, β=2, m=$\sqrt{3}$, κ=3, f=1, and $H_Y = 0$ equation [4.11] collapses to Nix-Gao model, as defined in equation [4.3]. Similarly, for β=1 with above conditions, equation [4.11] yields to

$$\frac{H-H_Y}{H_0-H_Y} = 1 + \left(\frac{h^*}{h}\right)^{1/2} \quad [4.13]$$

which is similar to kinking model derived for glassy polymers (Chong & Lam, 1999; Lam & Chong, 1999).

4.2.3. Reverse Indentation Size Effect

Recently, several studies have also shown that some materials experience a local increase in indentation hardness at small indentation depth (Faghihi & Voyiadjis, 2012; Wang & Ngan, 2004; Yang & Vehoff, 2007). This local hardening/ softening behavior is attributed to number of factors, such as interstitial pinning (Britton et al., 2009) interaction of grain boundary and plastic zone and grain boundary yielding (Faghihi & Voyiadjis, 2012). Underlining effect of all these phenomena is to arrest the motion of dislocation resulting in the 'pile-up' of the dislocation. The repulsive forces between dislocations thereby resist the deformation of the material that is manifested as local hardening in *H-h* curves. Thus, the material exhibiting reverse ISE shows local increase in hardness for increasing indentation depth.

4.3. Indentation Size Effect in Muscovite Mica

4.3.1. Indentation Normal to Basal Plane

As discussed above, hardness-depth for indentation normal to basal plane shows reverse ISE. Since ISE models in literature are given in terms of contact depth, indentation hardness is re-plotted with respect to contact depth, h_c, in figure 4.2. As seen from the figure, region I and region III exhibit the decrease in hardness with increasing indentation depth or normal ISE, however in the region II, local increase in the hardness occur with respect to the indentation depth. Taking an analogy from reverse ISE behavior in BCC metals, it is suspected that inhibition of dislocations by kink boundary may result in increase in dislocation storage and therefor increase in hardness. Other factors such as formation of new micro domains due to KBs and cracks and elastic loading after pop-ins and spallation also need to be further explored.

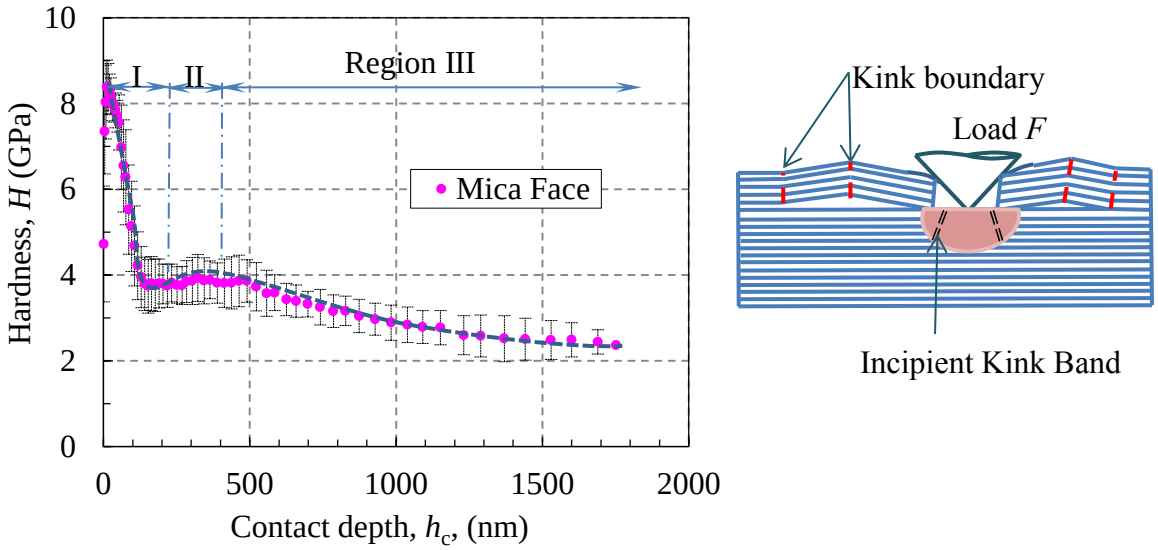

Figure 4.2: Reverse ISE for indentation normal to basal plane

4.3.2. Indentation Parallel to Edge

Indentations along the edge direction, on the other hand, exhibit normal ISE. Again, figure 4.3 is the re-plot of hardness data with respect to contact depth, h_c. As seen from figure, ISE

model based on Equation [4.11] fits hardness data for β=1.8, $H_0 = 1.42$ GPa $H_Y = 0.0$, which similar to Nix-Gao model (Equation [4.3]) and predicts h*=724.4 nm. Curve fitting using β=2, gives $H_0 = 1.51$, $H_Y = 0.0$ and h*=671.4 nm. As seen from the figure, Nix-Gao model fits the data fairly good even in nano depths (h<100nm). For b=0.53 nm, G=28.8 GPa, f=1, $\alpha = 0.5$, M=√3, κ=3 is, length scale h* predicted using equation [4.12] is 250.2 nm, which is smaller than those obtained using curve fit, but of the same order. Alternatively, $\alpha = 0.82$, gives correct match between calculated and derived h* which is higher than originally assumed, but still within the correct range .Some researcher vary f to curve fit especially at smaller depth (Feng and Nix, 2004) such that $f \to 1$ as $h \gg h^*$, which limits the GND density at shallow depth by exceeding plastic zone beyond contact radius ($a_p > a_c$). Coincidently, in this case good match between micro and nano indentation depth range suggest f=1 throughout.

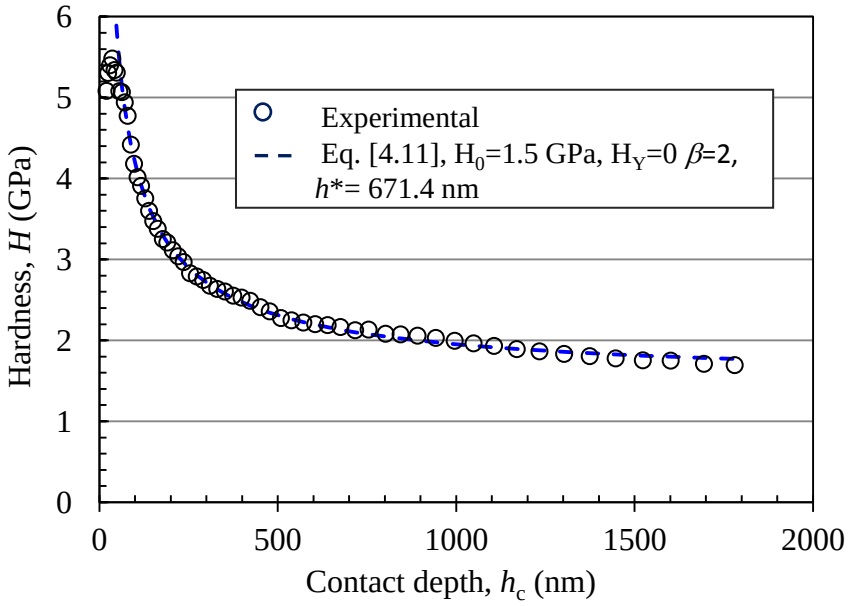

Figure 4.3: ISE effect for indentation parallel to basal plane.

It is noteworthy to mention that in the above fitting model, initial value of H_0=1.50 GPa was initially input in the model based on largest available nanoindentation depth (=2μm). Also, no

uniaxial test data are available for mica and thus best estimate for initial yield stress (friction hardness, H_Y) was obtained from triaxial compression test of mica (Mares & Kronenberg, 1993). The peak deviatoric stress for compression of muscovite mica at 45^o to (001) plane was in the range between 25-35 MPa, which gives shear stress, $\tau = 12 - 17$ MPa. Again assuming von Misses flow rule ($\sigma = \sqrt{3}\tau$) and Tabor (1951) factor of 3 to convert flow stress to hardness $H_Y \approx 0.07$, GPa.

4.4. Discussion

ISE on mica loaded parallel to basal plane, [001]*, showed good agreement with Nix-Gao model up to a depth of 75 nm. Slight variation in nano depth below 100 nm is may be attributed to tip roundness and errors inherent in CSM techniques. In this study, we only focused on the depth range 100 nm to 2 μm.

It can be noted that $H_Y = 0$, gives a good fit for the hardness data. This is attributed to the fact that a sharp indenter caused yielding in the mica immediately. Further, muscovite mica and biotite show fairly perfect plastic behavior with insignificant hardening or softening beyond yielding. Tri-axial test on Mica and Biotite showed that initial yielding occur at fairly low strain ($\varepsilon \cong$ 1-3%) for orientation favoring glide (loaded at 45^o to basal plane) (Christoffersen & Kronenberg, 1993; Mares & Kronenberg, 1993). For loading direction parallel to basal plane, slight softening was observed but it was attributed to kink annihilation (Mares and Kronenberg, 1992). Thus, it can be inferred that indentation in mica is governed by a fully plastic regime such that initial yield stress (σ_Y) coincide with flow stress (σ_0).

Deviation of Nix-Gao model at shallow depth of indentation is mainly attributed to prediction of GND density at these depths. It is reasonably assumed that for small depth, GND density exceed the maximum density that can be stored, whereby repulsive force acting on GND

forced them to spread out beyond the assumed hemispherical model. However, in case of mica, dislocations are restricted within glide plane i.e. basal plane. No cross slip or dislocation climb has been observed in mica. This restricts lateral spread of dislocation beyond contact zone, perpendicular to [001*] direction. This may also explain why no pile up was observed around indentation footprint. Two favorable dislocation glide direction within basal plane are [100] and 1/2 [110] or equivalent (Mares and Kronenberg, 1992, Christoffersen and Kronenber, 1993). Geometrically, this will result in volume with projected area equivalent of ellipse which gradually diverges out with depth. Now, excess dislocations align themselves forming multi poles, dislocation walls and consequently develop into IKB (incipient kink bank) and KB's. Formulation of IKBs and KBs results in pileup and nucleation of dislocations that also decreases dislocation density. Formation of KBs and IKBs are manifested as pop-ins in load-displacement curve. In other words, unique loading and crystallographic condition favors nucleation of excess GNDs into IKB and KBs rather than to spreading out. Similar observation was reported in tri-axial experiment for loading parallel to (001) plane where KB were mostly observed near the ends of the sample, thereby leading to the hypothesis that kinking is controlled by boundary condition (Mares and Kronenberg, 1993). Also, IKBs are reversible i.e, plastic flow due to formation of IKBs would reverse once the load is removed.

4.5. Conclusion

Simple Nix-Gao model was sufficient to model ISE in mica loaded parallel to basal plane for both macro and nano range. Further, based on Nix-Gao model, material length scale h^* was estimated as 724.4 nm and, α was calculated to be 0.82. Accuracy of the Nix-Gao model is affected by GND storage, strain hardening, formation and interaction of SSD and GND during indentation. In case of mica indentation parallel to basal plane, owing to near perfect plastic flow

and simple dislocation interaction, provided ideal condition for Nix-Gao model. This also underscores the adequacy of GND modeling and Taylor rule for hardness prediction in indentation method. Thus, it is likely that distribution GND and GND density are likely source of error and more physically based models should be developed, that incorporate crystallography and slip geometry.

4.6. References

Abu Al-Rub, R. K. (2007). Prediction of micro and nanoindentation size effect from conical or pyramidal indentation. *Mechanics of Materials, 39*(8), 787-802. doi: 10.1016/j.mechmat.2007.02.001

Abu Al-Rub, R. K., & Voyiadjis, G. Z. (2004a). Analytical and experimental determination of the material intrinsic length scale of strain gradient plasticity theory from micro- and nano-indentation experiments. *International Journal of Plasticity*, *20*(6), 1139-1182. doi: 10.1016/j.ijplas.2003.10.007

Abu Al-Rub, R. K., & Voyiadjis, G. Z. (2004b). Determination of the material intrinsic length scale of gradient plasticity theory. *Int. J. Multiscale Comput. Eng.*, *3*(3), 25.

Abu Al-Rub, R. K., & Voyiadjis, G. Z. (2006). A physically based gradient plasticity theory. *International Journal of Plasticity*, *22*(4), 654-684. doi: 10.1016/j.ijplas.2005.04.010

Britton, T. B., Randman, D., & Wilkinson, A. J. (2009). Nanoindentation study of slip transfer phenomenon at grain boundaries. *Journal of Materials Research, 24*(03), 607-615. doi: doi:10.1557/jmr.2009.0088

Busso, E. P., Meissonnier, F. T., & O'Dowd, N. P. (2000). Gradient-dependent deformation of two-phase single crystals. *Journal of the mechanics and physics of solids, 48*(11), 2333-2361. doi: http://dx.doi.org/10.1016/S0022-5096(00)00006-5

Chong, A. C. M., & Lam, D. C. C. (1999). Strain gradient plasticity effect in indentation hardness of polymers. *Journal of Materials Research, 14*(10), 4103-4110.

Christoffersen, R., & Kronenberg, A. K. (1993). Dislocation interactions in experimentally deformed biotite. *Journal of structural geology*, *15*(9), 1077-1095.

Faghihi, D., & Voyiadjis, G. Z. (2012). Determination of nanoindentation size effects and variable material intrinsic length scale for body-centered cubic metals. *Mechanics of Materials, 44*(0), 189-211. doi: http://dx.doi.org/10.1016/j.mechmat.2011.07.002

Feng, G., & Nix, W. D. (2004). Indentation size effect in MgO. *Scripta Materialia, 51*, 5.

Huang, Y., Zhang, F., Hwang, K. C., Nix, W. D., Pharr, G. M., & Feng, G. (2006). A model of size effects in nano-indentation. *Journal of the mechanics and physics of solids, 54*(8), 1668-1686. doi: 10.1016/j.jmps.2006.02.002

Kocks, U. F. (1966). A statistical theory of flow stress and work-hardening. *Philosophical magazine, 13*(123), 541-&. doi: 10.1080/14786436608212647

Lam, D. C. C., & Chong, A. C. M. (1999). Indentation model and strain gradient plasticity law for glassy polymers. *Journal of Materials Research, 14*(9), 3784-3788.

Liu, Y., & Ngan , A. H. W. (2001). Dependence of hardness in Copper single crystals measured by nano indentation. *Scripta matter, 44* 4.

Mares, V., & Kronenberg, A. (1993). Experimental deformation of muscovite. *Journal of structural geology, 15*(9), 1061-1075.

Nix, W. D., & Gao, H. (1998). Indentation size effects in crystalline materials: A law for strain gradient plasticity. *Journal of the mechanics and physics of solids, 46*(3), 411-425. doi: 10.1016/s0022-5096(97)00086-0

Pharr, G. M., Herbert, E. G., & Gao, Y. (2010). The indentation size effect: A critical examination of experimental observations and mechanical interpretations. *Annu. Rev. Mater. Res. , 40*, 22.

Shell De Guzman, M., Neubauer, G., Flinn, P., & Nix, W. D. (1993). The Role of Indentation Depth on the Measured Hardness of Materials. *MRS Online Proceedings Library, 308*, null-null. doi: doi:10.1557/PROC-308-613

Stelmashenko, N. A., Walls, M. G., Brown, L. M., & Milman, Y. V. (1993). Microindentations on W and Mo oriented single crystals: An STM study. *Acta Metallurgica et Materialia, 41*(10), 2855-2865. doi: http://dx.doi.org/10.1016/0956-7151(93)90100-7

Swadener, J. G., George, E. P., & Pharr, G. M. (2002). The correlation of the indentation size effect measured with indenters of various shapes. *J. Mech. Phys. Solids 50*, 13.

Tabor, D. (1951). *The hardness of metals*. New York: Oxford University Press Inc.

Taylor, G. I. (1938). Plastic strain in metals. *J. Inst. Metals 62*, 18.

Wang, M. G., & Ngan, A. H. W. (2004). Indentation strain burst phenomenon induced by grain boundaries in niobium. *Journal of Materials Research, 19*(08), 2478-2486. doi: doi:10.1557/JMR.2004.0316

Yang, B., & Vehoff, H. (2007). Dependence of nanohardness upon indentation size and grain size – A local examination of the interaction between dislocations and grain boundaries. *Acta Materialia, 55*(3), 849-856. doi: http://dx.doi.org/10.1016/j.actamat.2006.09.004

Chapter 5. Chemical and Microstructural Characterization of a Hybrid Clay-Lime-Starch Bio Nanocomposite

5.1. Introduction

Ordinary Portland cement (OPC) based concrete is the most widely used construction material in modern human history. However, production of OPC releases a large amount of greenhouse gases and therefore environmental sustainability is a growing concern. Furthermore, OPC based concrete is susceptible to deterioration under harsh environmental conditions, is brittle and may crack or spall due to degradation, resulting in expensive repairs or replacement of structures. Therefore, there is a growing demand for an environmentally sustainable binder that can be a viable alternative to OPC.

Recent archeological investigations revealed the use of a novel clay-based hybrid composite in some ancient Chinese structures. This ancient material technology uses lime, clay, sand, and biopolymers such as starch to prepare a hybrid clay based composite. Samples of this material obtained from an intact old tomb are remarkably tough, strong, acid resistant, and reportedly blast resistant. Understanding its mechanical properties and the underlying physical and chemical mechanisms controlling the mechanical behavior can help revitalize this ancient material technology and motivate its reuse in modern constructions for sustainability (Pant & Zhang, 2014).

This chapter presents the detail chemical, structural and microstructural characterization of a hybrid clay-lime-starch bio nanocomposite. Following sections describe the material and methods utilized, results and analysis of the results.

5.2. Materials and Methods

A sample of this hybrid clay-based composite was obtained from an approximately 250 year old tomb in Anhui province in China. Material obtained from the tomb site was remarkably

tough, strong and, except for few micro cracks, seemed remarkably sound and showed no sign of deterioration. Visual inspection of hybrid concrete showed few rounded, smooth pebble to sharp angular rock fractions, mostly obtained from igneous or metamorphic rock origin, embedded in the binder matrix. Figure 5.1 shows the optical micrograph of the polished surface. Slightly orange hue is due to oxides of the iron present in the clay. Again, except for few microcracks, samples show dense, compact structure with sound interface between binder and aggregates (sand and silt inclusions).

Figure 5.1: Optical microscope of the polished sample.

5.2.1. Sample Preparation

Powder sample for XRD was prepared from the scrapings of the freshly exposed binder surface, excluding any silt or sand size inclusions, and milled using anhydrous ethanol as coolant. X-ray diffraction patterns, XRD, for randomly oriented powder samples were collected in a Siemens D-5000 diffractometer using Cu-Kα radiation generated at 40 kV and 30 mA and a scan range of 2-70^{o} 2θ.

The powdered sample for NMR study was prepared similar to XRD analysis and then exposed to strong magnetic field to remove any magnetic materials. The solid state ^{29}Si and ^{27}Al MAS NMR spectroscopy were performed with Tecmag-based 270 and 363 MHz spectrometers

respectively. For this study, resonance frequency of 53.76 and 94.67 MHz were used for ^{29}Si and ^{27}Al MAS NMR characterization. Spinning rates used were 4 and 10 kHz. Measurements were conducted at room temperature with tetramethylsilane (TMS) and 1M $Al(NO_3)_3$ as external standards. Estimated error in chemical shift values are expected to be less than < 1 ppm.

The sample for SEM images was prepared by coating a small chip of freshly exposed concrete surface with Platinum (Pt). SEM images were obtained using FEI-Quanta 3D FEG equipped with dual beam (FIB/SEM) electron microscope. Images were captured electronically using a CCD camera. EDS analysis on the bulk uncoated concrete samples and micronized cement powder were obtained using EDAX analyzer attached to Hitachi S-3600N microscope.

The sample preparation process for TEM study was modified from Kim et al. (1995) and Krekeler et al. (2004). Immobilization technique, as described here, is suggested to preserve the original texture of the specimen. Samples were prepared by immersing small concrete chips, with an approximate diameter of 10 mm, in 100% ethanol for dehydration and exchange step for 24 hours. The glass vial containing the individual chip was placed in a rotator. After initial dehydration and exchange, the concrete chip was then immersed in 3:1 ethanol-resin mixture for 24 hours. Chips were then immersed in 1:1 and 1:3 ethanol-resin mixtures for 24 hours each, followed by immersion in 100% resin solution for 24 hours. In the final stage, chips were immersed in full strength Epon812 resin and placed in embedding mold. Samples were then placed in an oven set at 60^{o}C temperature overnight for polymerization. Epon812 resin used in above protocols was prepared by mixing 50 g of Epon812, 25 g of DDSA, 25 g of NMA and 2 g of DMP-30. Ultra-thin sections (100 nm thickness) for TEM were cut on a Leica EM UC7 Microtome. TEM sections were mounted on collodion-coated copper grids and imaged with a JEOL 100CX TEM.

5.3. Results

5.3.1. Chemical Composition

XRD pattern of the bulk powder sample obtained from cement binder matrix is shown in figure 5.2. Table 5.1 shows the result of semi-quantitative analysis of the mineralogical composition of powder sample based on methodology of Cook et al. (1975) and performed using in-house XRDPhil program used at LSU/Geology lab. XRD pattern exhibits a broad hump between 20^o-40^o 2θ which is characteristic of presence of amorphous C-S-H or geopolymers (Gruztec et al. 2009; Duxson et al., 2007; Fernández-Jiménez & Palomo, 2005; Xu & Van Deventer, 2000). Further the broadening of peak corresponding to Muscovite (8.8^o 2θ) is indication of activation of crystalline phase into nano-crystalline or amorphous structure.

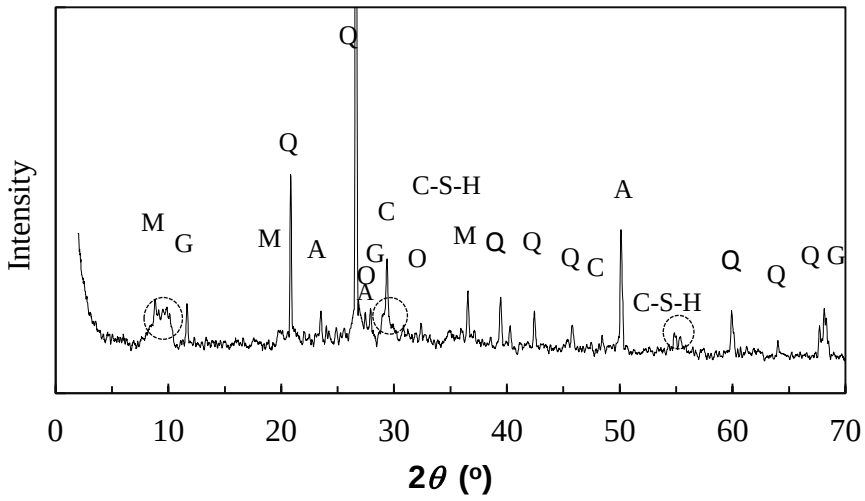

Figure 5.2: XRD pattern of powder matrix sample. (*Q*: Quartz, *M*: Muscovite, *O*: Orthoclase, *A*: Albite, *G*: Gypsum, and *C*: Calcite).

Further, low intensity peaks corresponding to layer spacing, *d*, ≈0.78 nm to 0.93 nm (2θ=9.48º-11º) indicate formation of nano-crystalline, hydrated calcium silicate precipitates. Other characteristic peaks corresponding to C-S-H at 2θ=29º, 2θ=50º and 2θ=55º (Gruztec et al. 2009), unfortunately, overlaps with peaks from more crystalline calcite, albite and quartz

phase in the sample. Well defined peaks corresponding to Calcite suggest formation of crystallized $CaCO_3$.

Table 5.1: Semi-quantitative analysis of hybrid composite.

Mineral	Concentration (%)
Quartz	43.0
Feldspar	9.0
Gypsum/Anhydrite	2.0
Calcite	9.0
Amorphous Phase	37.0

Figure 5.3 shows the Fourier transform infrared spectroscopy (FTIR) of the composite material (Zhang et al. 2013). Strong absorbance band corresponding to 1415 and 872 cm^{-1} confirms the presence of calcite. Similarly, absorbance band of 1326 cm^{-1} (-CH_2 group) and 762 cm^{-1} (C-O-C ring) indicates the existence of organic polymer (amylopectin in the starch). Similarly, absorbance band at 793 cm^{-1} is assigned to Si-O-Si, possibly belonging to C-S-H phase. Band corresponding to 1645 is assigned to O-H group belonging to starch or C-S-H in this composite material. EDS analysis of the powdered sample also suggested the presence of C-S-H, $CaCO_3$ along with starch in the sample as identified by carbon peak (Figure 5.4).

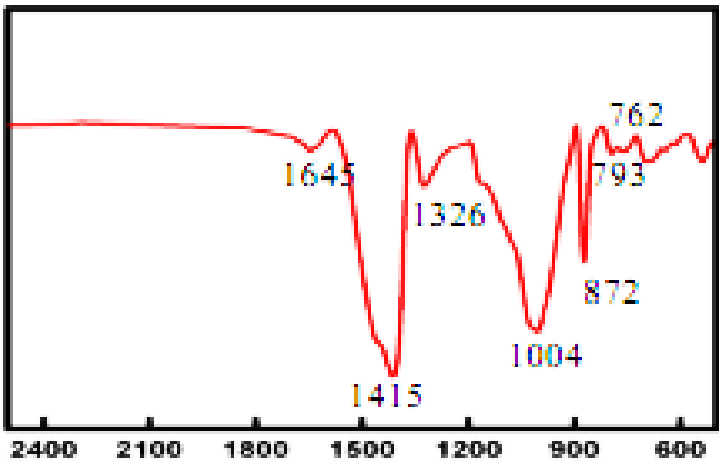

Figure 5.3: FTIR of a hybrid clay-lime-starch bio nanocomposite (Zhang et al., 2013).

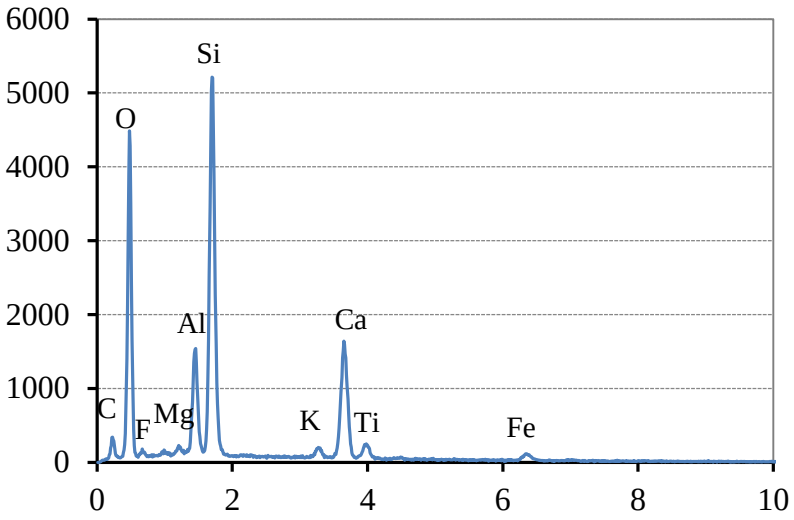

Figure 5.4: EDS analysis of the powdered sample.

5.3.2. Morphology

SEM images revealed a highly complex heterogeneous structure and morphology of the clay based binder. A fully activated clay based cement binder exhibit a very dense network of C-S-H globulets of 5 to 10 nm forming a frozen gel like structure (Figure 5.5). Pore size of the matrix ranges from micrometer to nanometer size and few micro-cracks are discernible in the structure. Morphology of the partially activated gel, on the other hand, retained tubular, platy or fibrous structure of the original clay structure (Figure 5.6). While the higher magnification images of the bulk unreacted clay aggregate showed partial activation on the surface and along the edges, (Figure 5.6b, inset), large mica sheet embedded in the matrix showed little to no structural change (Figure 5.6c). Thus, unreacted clay aggregates act as an active filler material in this composite. Further, SEM images indicate dense and compact microstructure and interfaces between aggregates and binder did not show any weak transition zone. In addition, highly porous, crystalline, honey-combed structures were also observed in the matrix (Figure 5.7) that could be the relics of dissolved minerals such as calcite or gypsum.

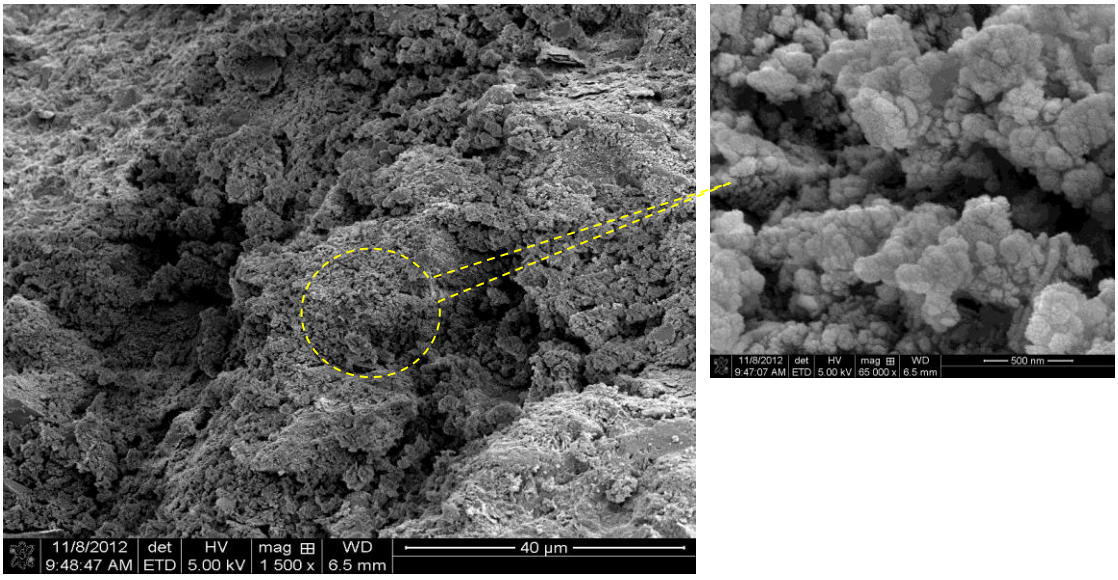

Figure 5.5: SEM micrograph of fully activated clay structure. High resolution image (inset) reveals globulets of size 5-10 nm clumped together to form larger micro-sized globules.

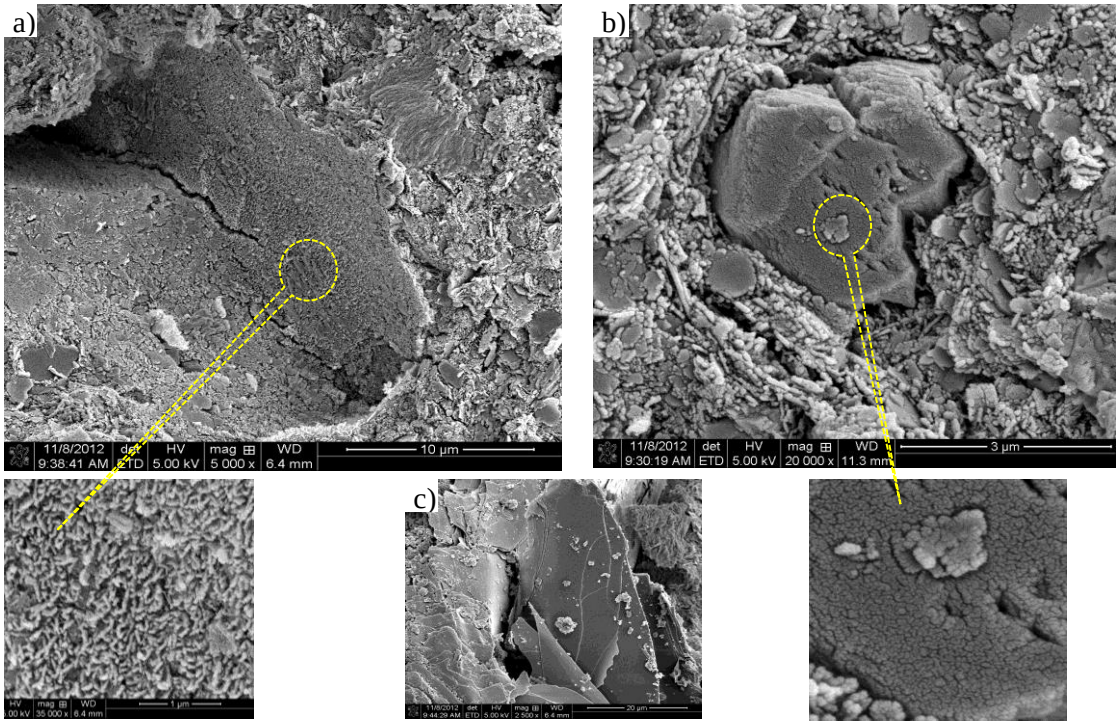

Figure 5.6: SEM micrograph of partially activated or unreacted clay aggregates in the matrix. a) morphology of crater formed possibly by removal of silt or sand inclusion. Tubular or fibrous morphology of the interface indicates influence of chemical species leached from aggregate during or after the polymerization process b) clay aggregate and c) unreacted micaceous plate in the cementitious binder.

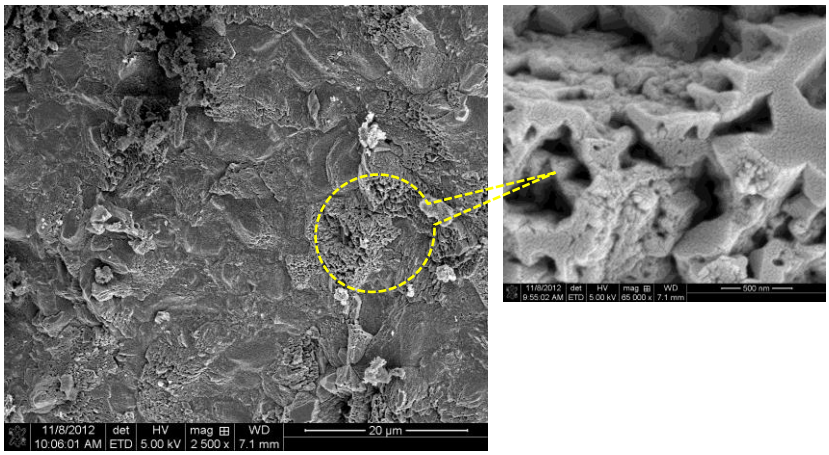

Figure 5.7: Porous, honey-combed relics of the dissolved crystalline phase.

5.3.3. Microstructure

High resolution TEM image of the clay concrete revealed a complex web like structure and dense nano-crystallites formed along the voids and within the matrix (Figure 5.8). Higher magnification image of the C-S-H phase revealed inner dense nano- crystalline core extending outward forming less dense, fibrous phase (Figure 5.9).

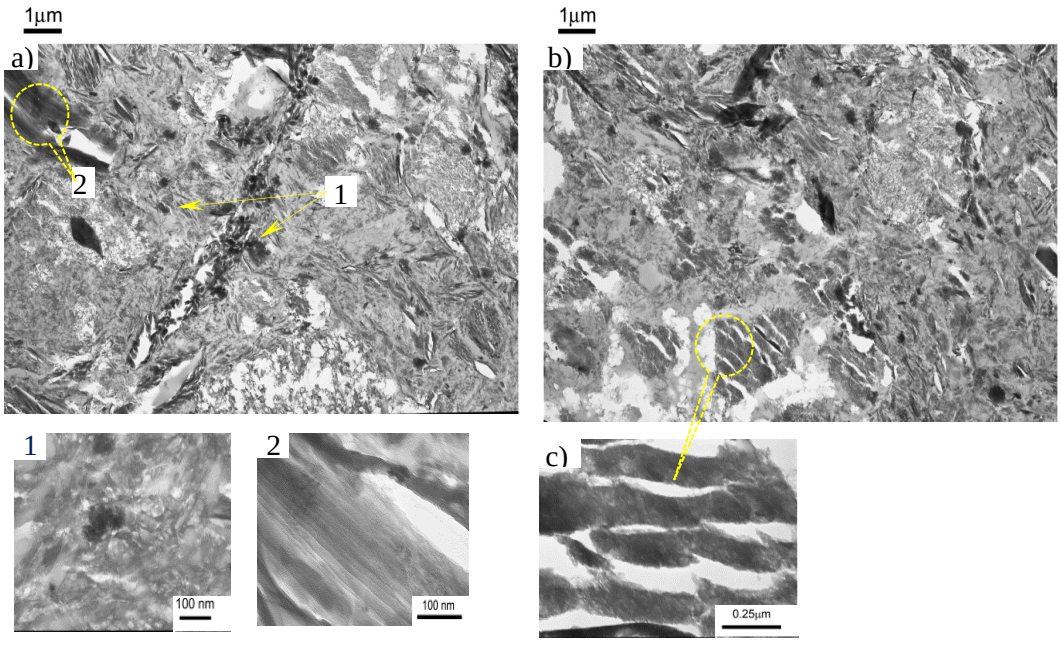

Figure 5.8: TEM micrograph showing a complex network of fibrous C-S-H phase a) nano-crystallites precipitates (point 1) in the matrix and along the pores, exfoliated clay plates b) reticulate C-S-H matrix with intercalated clay/C-S-H nanocomposites.

Pore size of the matrix, observed as electron transparent white image of the embedding epoxy, ranges from micrometer to nanometer scale. Relics of the organic polymers (rice starch) that were frequently used in these types of cements can also be seen (Figure 5.9, point 5). It is evident that interaction of clay and/or C-S-H with biopolymer formed the dense, intercalated nanocomposites (Figure 5.8c).

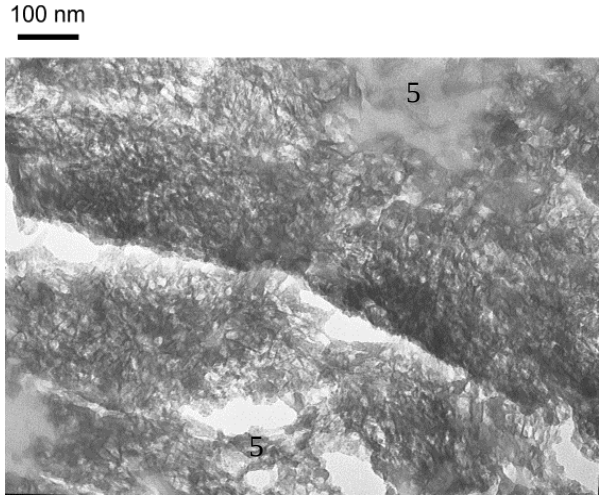

Figure 5.9: High magnification image of the C-S-H phase.

5.3.4. Structural Composition

Figure 5.10 shows the ^{29}Si MAS NMR spectra of the powdered sample. Deconvolution of this spectrum shows the presence of eleven components (Figure 5.10b). Peaks detected at -80.37 (Q^1), -81.85 (Q^{2p}) and -85.85 ppm (Q^{2Ca}) correspond to C-S-H phase (Aono et al., 2007) where notations Q^1 , Q^{2p} and Q^{2Ca} denote outer chain end, within chain (H^+ coordination) and within chain (CaO layer coordination) respectively (Klur et al., 1998). In addition to straight silicate anion chain, evidence of branching (Q^3) and networked chain (Q^4) is also seen in NMR spectra. High intensity peak at -107.62 and low intensity shoulders at -110.18 ppm indicate the tetrahedral coordination in Si_4 environment (Q^4(0Al)) that can be attributed to different crystalline silica phases such as sand (Parry-Jones et al., 1988) and quartz (Palomo et al., 2004)

inclusions in the composite material. Peaks detected at -87.47 (Q^4[4Al]), -92.96, -94.48 (Q^4[3Al,Si]), -96.78, -98.67 (Q^4[2Al,2Si]) and -102.01 (Q^4[Al,3Si]) indicate the presence of cross linked frameworks of aluminosilicates such as zeolites and geopolymers (Palomo et al., 2004; Škvára et al., 2009).

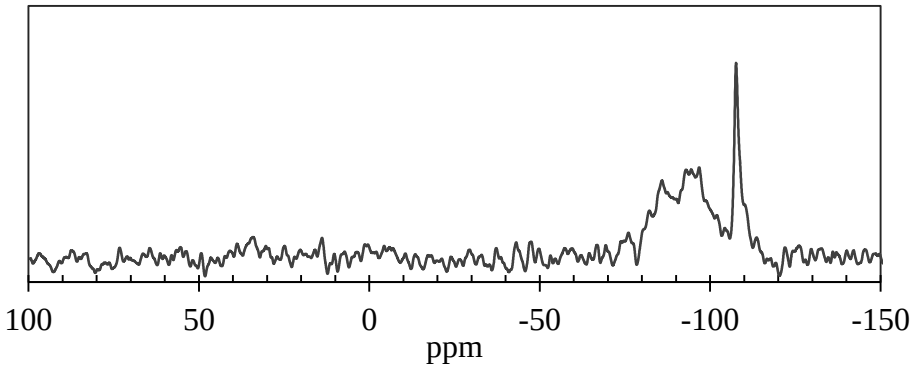

5.10a)

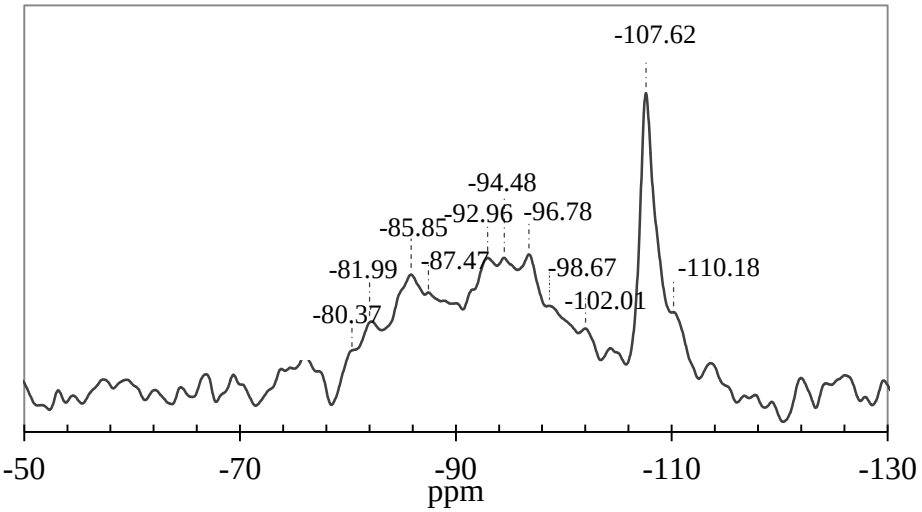

5.10b)

Figure 5.10: a) ^{29}Si MAS NMR spectrum b) peaks identified for various Si coordination.

The ^{27}Al MAS NMR spectrum of powdered sample shows a dominant peak at 56.27 ppm corresponding to tetrahederally coordinated aluminium (AlQ^4(4Si) type) and minor shifts at 3.57 ppm corresponding to octahedrally coordinated aluminium.

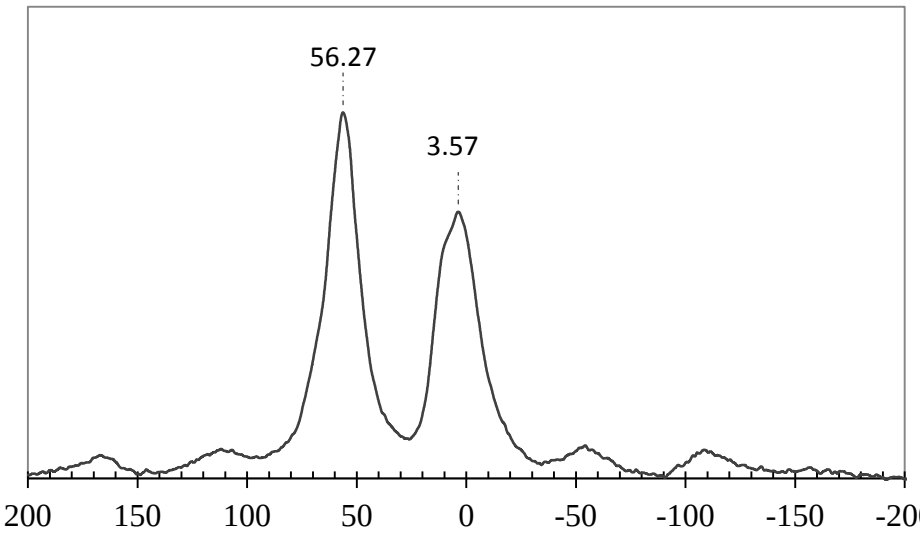

Figure 5.11: ^{27}Al MAS NMR spectra of composite material.

5.4. Discussion

Microstructural and morphological analyses of the hybrid clay concrete indicate heterogeneous structure with different degrees of activation. Fully activated cement phase showed globular, frozen viscous structure in SEM whereas partially activated phase showed reminisce of the morphology of raw material. Closer examination of the partially activated or unreacted aggregate under higher magnification, however, indicated reaction along the edges as well on the surfaces. Therefore, it can be inferred that reactivity of aluminosilicate minerals was mostly influenced by particle size rather than mineralogical composition. It is highly likely, given the available technology, these cement mixes were prepared by simply mixing non-pulverized clays, coarse aggregates and lime and using high water/cement (w/c) ratio for workability. Higher w/c ratio is inferred based on dominance of LD C-S-H phase in cementitious binder, as observed in SEM and TEM micrograph. This is further corroborated by the precipitation of nano-crystallites and network of fibrous low density C-S-H phase in the voids and micro-cracks, as observed in TEM images.

Presence of biopolymer (starch) in this composite material is corroborated by FTIR analysis (Figure 5.3), EDS (Figure 5.4) and TEM images. This is rather striking observation, since starch is biodegradable. Therefore, it is likely that high temperature during mixing of lime and highly alkaline environment thereafter sterilized the composite and thus preserved the biodegradable starch. However, more intriguing fact is the role of biopolymer in the physical and chemical properties of this composite material. The use of starch or other biopolymers as a thickening or gelling agent is a well-established practice in numerous industrial fields, such as paper making, textiles and food industry to name few. Thus, in this case, gelatinous starch acts as a conditioner during mixing process whereby allowing uniform distribution of lime and clay in the matrix. In the latter stage, dissolved amylopectin (starch) polymer is integrated structurally with clay or C-S-H to form novel bio-nano-composites. Evidence of intercalated clay and/or C-S-H particles in TEM image indicates active interaction between inorganic binders and organic biopolymers. Owing to the spatial confinement of biopolymer and dense clay and C-S-H layer, these types of intercalated nanocomposites are expected to demonstrate superior mechanical and barrier properties. Role of dissolved amylopectin polymers during pozzolanic reaction or possible polymerization of dissociated alumino-silicate species requires further attention.

Structural analysis of the binder phase using NMR spectroscopy suggests multiple phase C-S-H in the cementitious binder of this hybrid bio-nanocomposite. Abundance of Q^2 and Q^{2ca} peaks in ^{29}Si NMR spectra indicate that some polymerization has occurred in the C-S-H. Q^4 peaks suggest presence of three dimensional aluminosilicate networks characteristic of geopolymers. Coexistence of C-S-H and geopolymers gel in the alkali activation of various aluminosilicate sources (metakaolin, fly ash) in the presence of calcium hydroxide was demonstrated in recent studies (Alonso & Palomo, 2001; Granizo et al., 2002; Yip et al., 2005).

Generally, higher hydroxyl (OH^-) ion concentration impedes the dissolution of calcium hydroxide and therefore deficiency of Ca^{+2} favors the fixation of dissolved silicate in the form of alkali-aluminosilicate (Alonso & Palomo, 2001). On the other hand, for lower OH^- concentration, presence of Ca^{+2} in the solution promotes the formation of C-S-H gel. Thus, owing to the dynamic nature of the dissolution and polymerization, it is quite possible that a several phases may coexist in the final product depending upon hydrothermal condition, concentration and presence of alkaline cation species in the primary solution (Figure 5.12).

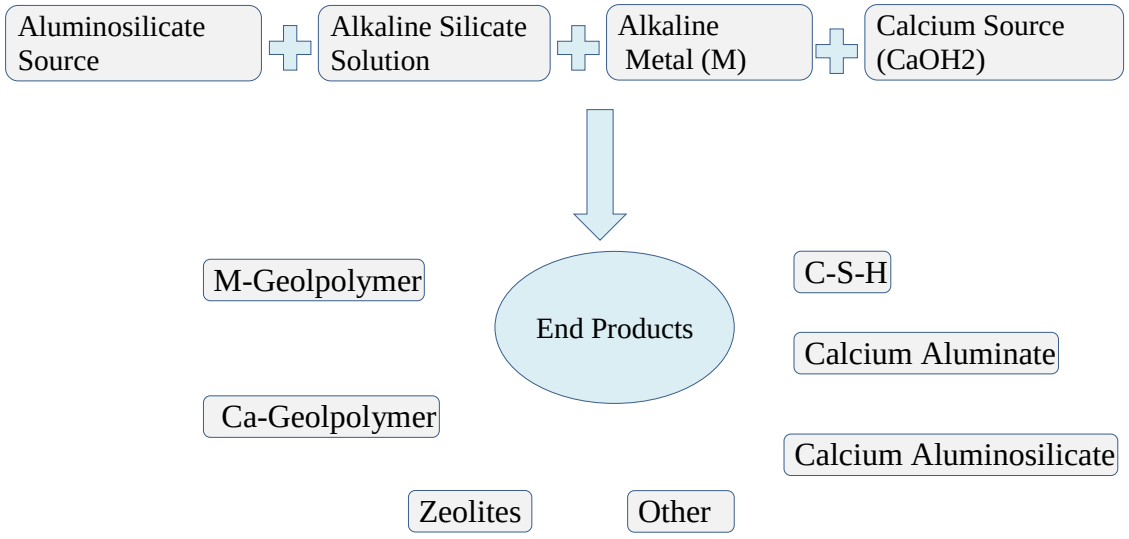

Figure 5.12: Conceptual model for end products of alkali activation of aluminosilicate sources in the presence of calcium source (modified fromYip et al. (2005))

Origin of the characteristic properties such as strength, durability and resistance against environmental degradation can, now, be attributed to the unique microstructural, morphological and structural features of this hybrid bio-nano-composite. Lime stabilization of high plasticity clays is a well-established method to improve their engineering properties. Generally, cation exchange, flocculation and agglomeration and formation of cementitious binder through weak pozzolanic reaction are involved in the stabilization process. The main distinctive feature is the

extent of pozzolanic reaction in this hybrid material. TEM images show that large interconnected networks of rigid C-S-H phase are formed similar to those produced in OPC based concrete. In addition nanocomposites are formed, possibly networked aluminosilicates, in the supersaturated pore volumes. Presence of intercalated nanocomposites is another distinctive feature. Overall, these features render low permeability, thereby minimizing the percolation, washout or environmental degradation of the composite material.

5.5. Conclusions

The microstructure of the hybrid clay-lime-starch composite showed highly heterogeneous structure consisting mainly of C-S-H binder and silt, sand, and unreacted clay aggregates as filler material. Microstructure of this C-S-H phase is similar to that produced in OPC. However, interaction of the biopolymer (sticky rice) with clay and C-S-H resulted in intercalated nanocomposites which appear to be the key to superior mechanical properties of this composite. Based on this study, we propose that slow and weak pozzolanic reaction between clay and lime produces a cementitious binder consisting of C-S-H phase with an overall low packing density. Clay, sand, and silt particles act as active fillers in this composite, whereby forming a dense and compact mass, which renders durability and toughness to this hybrid composite.

5.6. References

Alonso, S., & Palomo, A. (2001). Calorimetric study of alkaline activation of calcium hydroxide–metakaolin solid mixtures. *Cement and Concrete Research, 31*(1), 25-30. doi: 10.1016/s0008-8846(00)00435-x

Aono, Y., Matsushita, F., Shibata, S., & Hama, Y. (2007). Nano-structural changes of C-S-H inhardened cement paste during drying at 50°C. *Journal of Advanced Concrete Technology, 5*(3), 13.

Cook, H. E., Johnson, P. D., Matti, J. C., & Zemmels, I. (1975). Methods of sample preparation and X-ray diffraction data analysis, X-ray Mineralogy Laboratory, Deep Sea Drilling Project, University of California, Riverside. In Hayes, D.E., Frakes, L.A., et al.,. *Init. Repts. DSDP, 28: Washington (U.S. Govt. Printing Office)*, 9.

Duxson, P., Fernández-Jiménez, A., Provis, J. L., Lukey, G. C., Palomo, A., & Deventer, J. S. J. (2007). Geopolymer technology: the current state of the art. *Journal of Materials Science, 42*(9), 2917-2933. doi: 10.1007/s10853-006-0637-z

Fernández-Jiménez, A., & Palomo, A. (2005). Composition and microstructure of alkali activated fly ash binder: Effect of the activator. *Cement and Concrete Research, 35*(10), 1984-1992. doi: 10.1016/j.cemconres.2005.03.003

Granizo, M. L., Alonso, S., Blanco-Varela, M. T., & Palomo, A. (2002). Alkaline Activation of Metakaolin: Effect of Calcium Hydroxide in the Products of Reaction. *Journal of the American Ceramic Society, 85*(1), 225-231. doi: 10.1111/j.1151-2916.2002.tb00070.x

Grutzeck, M. W., Hoyle, S., Kwan, S., LaRosa, J., & Bozich, S. (1991). Microstructure, porosity and mechanical property relationships of calcium-silicate-hydrate (pp. 117): Pennsylvania State University, Park Materials Research Lab.

Kim, J. W., Peacor, D. R., Tessier, D., & Elsass, F. (1995). A Technique for maintaining texture and permanent expansion of smectite interlayers for TEM observation. *Clays and Clay Minerals, 43*(1), 51-57. doi: 10.1346/ccmn.1995.0430106

Klur, I., Pollet, B., Virlet, J., & Nonat, A. (1998). C-S-H Structure Evolution with Calcium Content by Multinuclear NMR. In P. Colombet, H. Zanni, A.-R. Grimmer & P. Sozzani (Eds.), *Nuclear Magnetic Resonance Spectroscopy of Cement-Based Materials* (pp. 119-141): Springer Berlin Heidelberg.

Krekeler, M. P. S., Guggenheim, S., & Rakovan, J. (2004). A microtexture study of palygorskite-rich sediments from the Hawthorne Formation, southern Georgia, by transmission electron microscopy and atomic force microscopy. *Clays and Clay Minerals, 52*(3), 263-274. doi: 10.1346/ccmn.2004.0520302

Palomo, Á., Alonso, S., Fernandez-Jiménez, A., Sobrados, I., & Sanz, J. (2004). Alkaline Activation of Fly Ashes: NMR Study of the Reaction Products. *Journal of the American Ceramic Society, 87*(6), 1141-1145. doi: 10.1111/j.1551-2916.2004.01141.x

Pant, R., & Zhang, G. (2014). Nanomechanical and microstructural characterization of a hybrid clay-lime-starch composite. *Proceedings of the 2014 Geo-Congress: Geo-Characterization and Modeling for Sustainability*, (in press).

Parry-Jones, G., Al-Tayyib, A. J., & Al-Mana, A. I. (1988). Evaluation of degree of hydration in concrete using 29Si magic angle spinning NMR in solids. *Cement and Concrete Research, 18*(2), 229-234. doi: http://dx.doi.org/10.1016/0008-8846(88)90007-5

Škvára, F., Kopecký, L., Šmilauer, V., & Bittnar, Z. (2009). Material and structural characterization of alkali activated low-calcium brown coal fly ash. *Journal of Hazardous Materials, 168*(2–3), 711-720. doi: 10.1016/j.jhazmat.2009.02.089

Xu, H., & Van Deventer, J. S. J. (2000). The geopolymerisation of alumino-silicate minerals. *International Journal of Mineral Processing, 59*(3), 247-266. doi: 10.1016/s0301-7516(99)00074-5

Yip, C. K., Lukey, G. C., & van Deventer, J. S. J. (2005). The coexistence of geopolymeric gel and calcium silicate hydrate at the early stage of alkaline activation. *Cement and Concrete Research, 35*(9), 1688-1697. doi: 10.1016/j.cemconres.2004.10.042

Zhang, G., & Hu, L. Collaborative Research: Rediscover Ancient Chinese Concrete: the Fundamental Science and Synthesis of an Organic-Inorganic Hybrid Green Binder (unpublished)

Chapter 6. Nanoindentation Characterization of a Hybrid Clay-Lime-Starch Bio Nanocomposite

6.1. Introduction

Nanoindentation test is a widely used technique to assess elastic modulus and hardness of the bulk homogenous material. Recent developments in grid indentation technique have extended the application of nanoindentation to nanomechanical characterization of heterogeneous materials such as composites, polymers, biomaterials and geomaterials (Sakulich & Li, 2010; Ulm et al., 2007). In the previous chapter, detailed chemical and nano/micro structural characterization of hybrid clay-based composite was presented. In this chapter, results and analysis of the grid nanoindentation test used to extract the nanomechanical properties and volume fraction of mechanically different phases of this hybrid composite material is presented.

6.2. Materials and Methods

6.2.1. Sample Preparation

In order to prepare smooth surfaces for indentation, small chips of 10-15 mm size were first carefully cut and impregnated with Epon812 resin or LR White Resin using the same protocol used in TEM specimen preparation, as described in Section 5.2. The specimens were then grounded and polished with 400, 600, and 800 grid silicon carbide paper followed by finer polishing using low nap polishing cloth and alcohol based diamond suspension (3μm and 1μm). Surface roughness was measured using optical profilometer and found to be in order of 150-200 nm. Relatively smooth areas within the matrix were chosen for grid nanoindentation tests.

6.2.2. Nanoindentation Testing

Nanoindentation tests were performed with an MTS Nano XP indenter at ambient conditions. An XP indenter equipped with Berkovich tip was used to indent under the continuous

stiffness measurement (CSM) mode at a constant indentation strain rate ($\dot{h}/h$) of 0.05 s^{-1} where h is indentation depth, frequency of 45 Hz, and amplitude of 1 nm. For homogeneous material where continuum scale mechanical models are valid, two mechanical properties indentation hardness, H, and indentation modulus, E_r, can be extracted directly from F-h curve (Oliver & Pharr, 1992, 2004)

$$E_{\mathrm{r}} = \frac{\sqrt{\pi}}{2\beta\sqrt{A_{\mathrm{c}}}} S \qquad [6.1]$$

$$H = \frac{F}{A_{\mathrm{c}}} \qquad [6.2]$$

$$S = \frac{dF}{dh}\Big|_{h_{max}} \qquad [6.3]$$

where β is dimensionless correction factor for indenter tip shape and β =1.05 is commonly used for Berkovich indenter (Oliver and Pharr 2004), S is unloading indentation stiffness and A_c is contact area at h_{max} and it is a polynomial function of the contact depth h_c at h_{max}, (i.e.,$A_c = f(h_c)$, (Oliver & Pharr, 1992, 2004; Sneddon, 1965)) In CSM method, typically a small oscillation (sinusoidal) is applied to the force signal during loading, and amplitude and phase of the displacement oscillation at the same frequency are measured. Harmonic contact stiffness, S, is then measured continuously as the ratio of the load amplitude to the oscillation amplitude (Pharr et al., 2009). The constant displacement amplitude oscillation (1 nm) utilized in this study, however, was implemented by feedback control technique.

For isotropic homogeneous materials, reduced modulus and elastic modulus are related as

$$\frac{1}{E_r} = \frac{(1-\nu^2)}{E} + \frac{(1-\nu_i{}^2)}{E_i} \qquad [6.4]$$

where E and υ are the elastic modulus and Poisson's ratio of the tested material and E_i and υ_i are that of indenter respectively. In this research, Poisson's ratio υ was assumed to be 0.2 for all

measurements. As discussed in section 2.4.1, Poisson's ratio of the tested material has no significant influence on elastic modulus (Mencik et al., 1997).

Indentation gives the bulk properties of material at length scale $\mathcal{L}\approx 4x h_{max}$ (Constantinides et al., 2003). Considering an infinite half-space composed of *N* different phases of characteristic length scale ℓ, such that $\ell << \mathcal{L} << D$, where *D* is the material length scale, for indentation depth, $h >> \ell$, each indentation event is a response of one of the individual phases in the material. Thus, if a large number of indentations are performed in grid with spacing larger than the characteristic size of individual phase, probability of finding each phase is equal to the surface fraction occupied by the two phases on the indentation surface. On the other hand, for $h \square \ell$, indentation gives some average response of the composite material. Grid indentation involves a large number of indentation in arrays and statistical deconvolution of indentation results (Constantinides et al., 2006; Constantinides et al., 2003; Ulm et al., 2007).

For the deconvolution of indentation data, distribution of mechanical properties of each phase in the hybrid composite material was assumed Gaussian distribution. Then, the cumulative distribution function, CDF, of each phase is given as:

$$D\left(X_i; \mu_j^X, \sigma_j^X\right) = \frac{1}{\sigma_j^X \sqrt{2\pi}} \int_{-\infty}^{X_i} \mathrm{e}^{-\frac{1}{2}\left(\frac{u-\mu_j^X}{\sigma_j^X}\right)^2} du \qquad \mathrm{X}=E,H \tag{6.5}$$

where $\mu_j = \frac{1}{N_j}\sum_{\mathrm{k}=1}^{N_j} \mathrm{X_k}$ is the mean and $\sigma_{\mathrm{j}}^2(x) = \frac{1}{N_j - 1}\sum_{k=1}^{N_j}\left(X_{\mathrm{k}} - \mu_{\mathrm{k}}\right)$ is the standard deviation. Additionally, surface fraction occupied by each phase, f_{j}, is given as $f_j = \frac{N_j}{N}$ such that $\sum_{\mathrm{j}=1}^{n} f_j = 1$. Now, the unknowns $\left\{f_j, \mu_j^M, \sigma_j^M, \mu_j^H, \sigma_j^H\right\}$ for $\mathrm{j} = 1, n$ were determined by minimizing scaled experimental CDF and scaled model CDF (Ulm et al., 2007)

$$min \sum_{\mathrm{i}=1}^{N} \sum_{X=M,H} \left(\sum_{j=1}^{n} f_j D\left(X_i; \mu_j^X, \sigma_j^X\right) - D_X(X_i)\right)^2 \tag{6.6}$$

where $D_X(X_i) = \frac{i}{N} - \frac{1}{2N}$ for $i \in [1, N]$ gives the points of experimental CDF. In order to avoid overlap of the two distributions, further constraints were applied as

$$\mu_j^X + \sigma_j^X \leq \mu_{j+1}^X + \sigma_{j+1}^X \quad X=E, H \qquad [6.7]$$

6.3. Results

6.3.1. Surface Roughness

Surface finish of the test specimens was determined using optical profiler equipped with Veeco software. The root mean square surface roughness, R_q, of the specimens after final polishing with 1 μm diamond suspension on low nap cloth was in the order of 200 nm. It was observed that due to different removal rates of the silt/sand inclusions, hardened cement binder, and unreacted clays, prolonged polishing only increased the surface roughness. Therefore, this surface roughness was deemed optimum level achieved for this composite material using the method described above.

6.3.2. Grid Indentation

Three grid indentation series were performed on two samples prepared using technique described above. Trials ANC-1 and ANC-2 were performed on two separate locations in same specimen whereas trial ANC-3 was performed on another concrete specimen. Figure 6.1 shows the plot of indentation modulus versus hardness for trial ANC-1. A good scaling relationship, $E_r \propto \sqrt{H}$ confirms the relationship given by Equations [6.1] and [6.2] thereby implying the separation of scales in each indentation test and random sampling of the data. This also implied that statistical analysis could be employed with confidence (Ulm & Abousleiman, 2006).

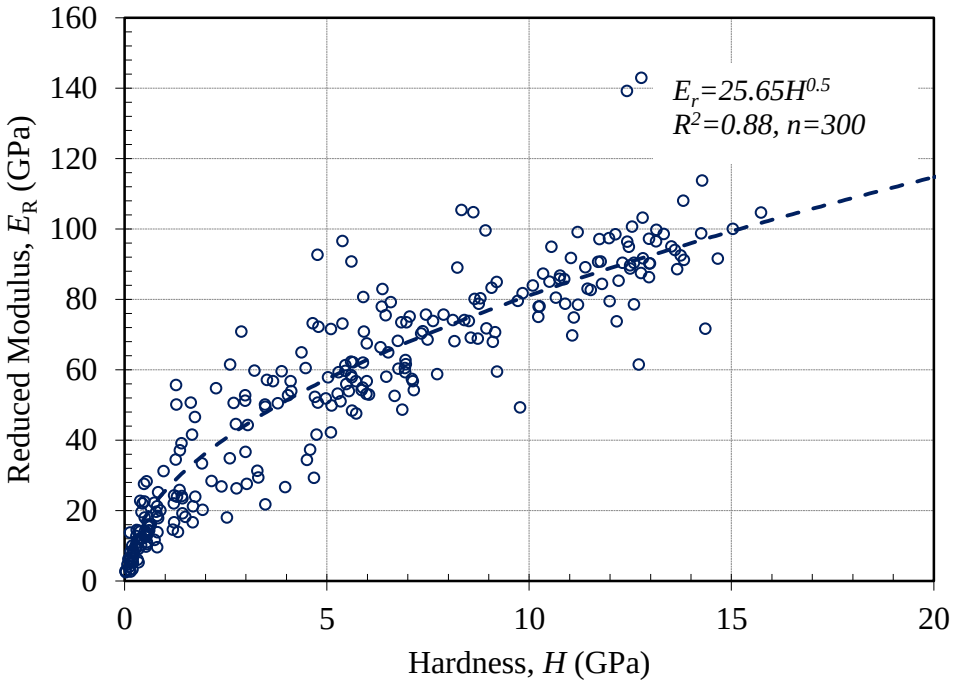

Figure 6.1: Relationship between indentation modulus and indentation hardness for concrete specimen ANC-1 (h=200-210 nm, n=*300*).

6.3.3. Indentation Modulus

Figure 6.2a and 6.2b shows the deconvoluted peaks of the indentation modulus, E_r, for trial ANC-1 (n =300). Although individual peaks were deconvoluted using the cumulative distribution function, CDF, described in section 6.2.2, results are also visualized in terms of probability distribution function, PDF, plots.

Deconvolution of indentation modulus CDF indicate five distinct mechanical phases present in this hybrid nano-composite. The lowest peak corresponding to E_r < 8 GPa is possibly from the effect of micro porosity and indentation on LR White resin impregnated pores. Indentation modulus of the polished LR White resin was found to be 2.86±0.39 GPa. Peak corresponding to 12.94-17.3 GPa is from the clay-polymer (starch) aggregates or clay-lime aggregates. Similarly, E_r = 22.85-26.10 GPa indicates indentation on C-S-H phase. Likewise peaks corresponding to E_r

=52.46 -54.02 GPa and E_r =79.4 -84 GPa result from indentation on nanocomposites (intercalated C-S-H and/or clay, $CaCO_3$, geopolymers) and sand/silt inclusions respectively.

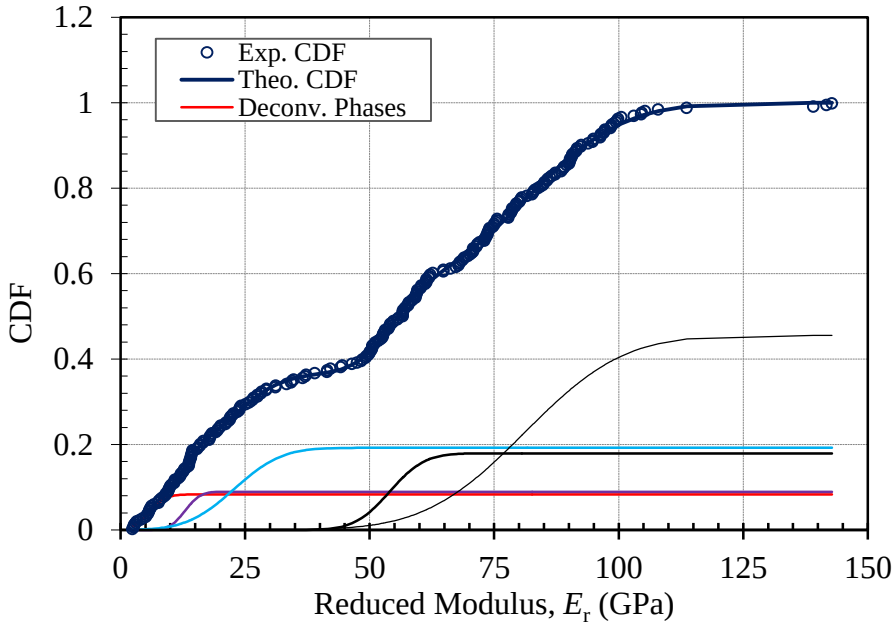

6.3a)

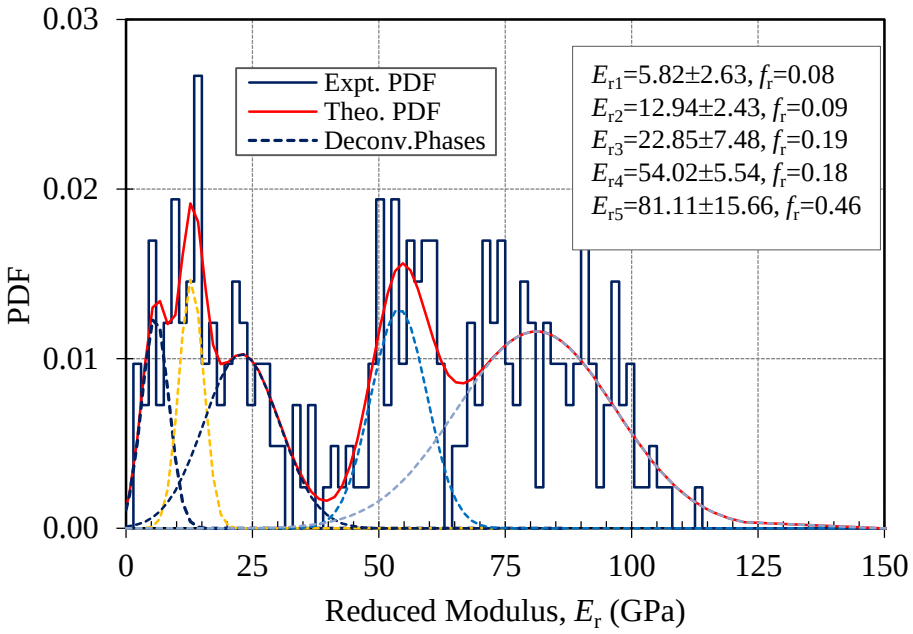

6.3b)

Figure 6.2: Reduced modulus deconvolution of ANC-1 data a) CDF b) PDF

Table 6.1: Summary of reduced modulus of constituent phases obtained from statistical analysis of grid indentation results for three different trials.

Trials	Reduced modulus	# data	Constituent Phase *i*				
			MP,LRW	CPA	C-S-H	NC	INC
ANC-1	μ_i, GPa	300	5.82	12.94	22.85	54.02	81.11
	σ_i, GPa		2.63	2.43	7.48	5.54	15.66
	fr_i, %		0.08	0.09	0.19	0.18	0.46
ANC-2	μ_i, GPa	100	8.18	17.3	26.10	52.46	79.4
	σ_i, GPa		3.62	2.58	6.20	10.69	9.88
	fr_i, %		0.31	0.26	0.19	0.21	0.06
ANC-3	μ_i, GPa	100	4.8	11.6	24.3	53.4	84.0
	σ_i, GPa		1.5	5.4	3.5	8.9	8.7
	fr_i, %		0.19	0.43	0.17	0.19	0.02

MP: Microporosity, LRW: resin, CPA: clay-polymer-aggregate, NC: nano-crystallites and INC: inclusions.

6.3.4. Hardness

Summary of the deconvoluted hardness data is shown in Figure 6.3 and Table 6.2. Again indentation hardness of the LR White surface is the order 0.12 GPa. Thus, the lowest hardness value is signature of indentation on high porosity region. Hardness data for other peaks are consistent with indentation moduli peaks obtained in section 6.3.3.

Table 6.2: Summary of hardness of constituent phases obtained from statistical analysis of grid indentation results for three different trials.

Trials	Hardnes	# data	Constituent Phase *i*				
			MP,LRW	CPA	C-S-H	NC	INC
ANC-1	μ_i, GPa	300	0.16	0.48	1.35	5.70	12.16
	σ_i, GPa		0.07	0.16	0.43	2.23	1.53
	fr_i, %		0.07	0.14	0.11	0.45	0.22
ANC-2	μ_i, GPa	100	0.28	0.62	1.21	3.27	8.41
	σ_i, GPa		0.10	0.25	0.11	1.94	0.45
	fr_i, %		0.24	0.27	0.13	0.29	0.06
ANC-3	μ_i, GPa	100	0.23	0.57	1.39	5.57	12.16
	σ_i, GPa		0.15	0.19	0.55	2.20	1.53
	fr_i, %		0.41	0.18	0.17	0.22	0.02

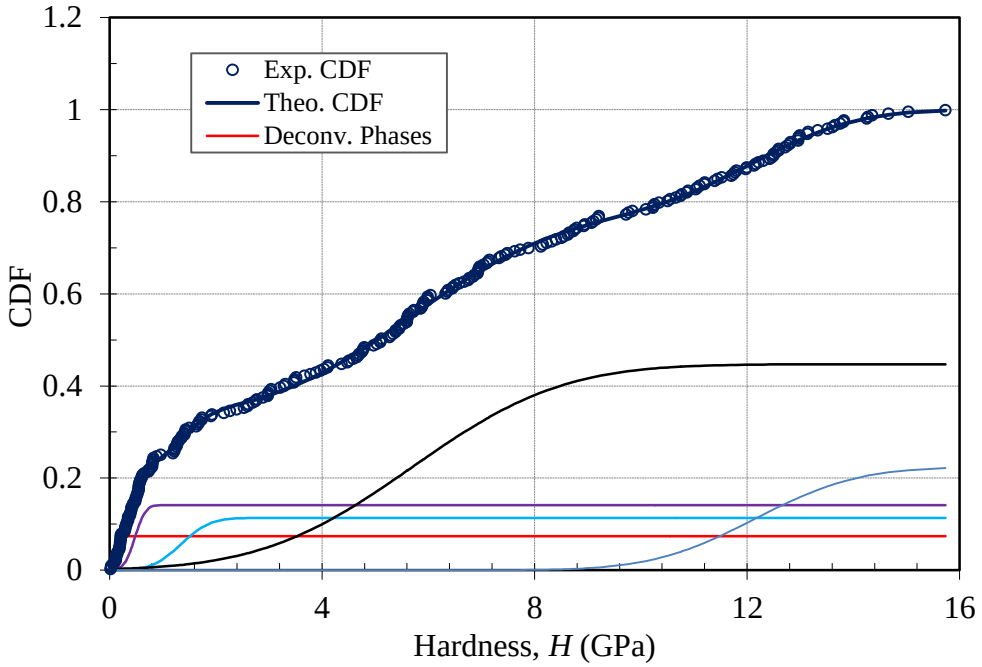

6.4a)

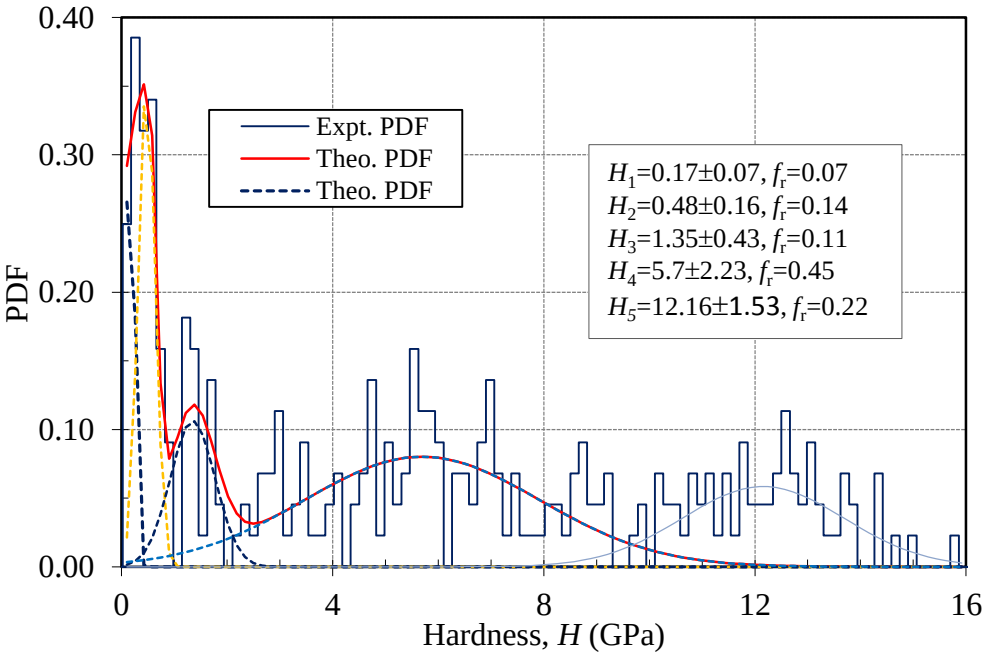

6.4b)

Figure 6.3: Hardness deconvolution of ANC-1 data a) CDF b) PDF

6.4. Discussion

6.4.1. Indentation Depth: Length Scale

Choice of indentation depth in a grid indentation technique is primarily governed by length scale of the largest heterogeneity, *d*, and the microstructure, *D*. Based on microstructural analysis, characteristic size of fully activated gel is of the order of 5-10 nm. Capillary pores in the CSH phase are also of similar dimension and randomly distributed throughout. Therefore, it is imperative that indentation response of C-S-H phase is inclusive of the effect of nano porosity. On the other hand, microstructural length scale is 1 μm to 4 μm (Figure 5.5-5.9). Since unreacted clay, sand or silt inclusions are crystalline, *d* is in the order of lattice parameters. Based on SEM and TEM micrographs, *D* for these phases are estimated between 1 μm to several micrometers. Therefore, indentation depth, $h \in [200,300]$ nm is sufficient to satisfy the scale separability and 1/10 rule for nanoindentation sensing of individual phase properties. However, this depth does not necessarily satisfy the roughness criteria, $R_q < 3h$ (Donnely et al., 2006) . However, efforts to bring R_q below 200 nm range without disturbing the sample surface were not successful. In fact, in the nanoindentation study of shales, Bobko and Ulm (2008) performed similar experiment at this depth range with satisfactory results. Thus, this study concurs that criteria for surface roughness can be relaxed, especially for a grid indentation technique that involves statistical analysis of massive volume of indentation data on a large area. Further, use of the CSM technique minimized the chances of false detection of the surface, thereby minimizing the effect of surface roughness.

6.4.2. Nanomechanical Characteristics of a Hybrid Clay-Lime-Starch Bio Nanocomposite

Statistical deconvolution of indentation data suggests five distinct mechanical phases in this hybrid composite material. While the peak corresponding to highest and lowest E_r (and H) shows

the indentation behavior in presence of micro porosity and inclusion phases, other three phases are identified as the signature of cementing binder phases. Indentation moduli of 22.85-26.10 GPa is indicative of indention on C-S-H phase. Similar indentation testing on white cement and ordinary Portland cement mix reported indentation moduli in the range of 18±4 to 21.7±2.2 for low density (LD) C-S-H and 29.1±1 GPa to 31±4 GPa for high density (HD) C-S-H phase (Constantinides & Ulm, 2007; Jennings et al., 2007). It is noteworthy to mention that indentation modulus of nanogranular materials, such as cement and concrete, is highly dependent on packing density, thus, variation in stiffness measurement is understandable. Further, we made no effort to distinguish LD C-S-H or HD C-S-H phase in this composite material. In fact, based on SEM/TEM images, it is recognized that LD C-S-H is a dominant phase. Hardness data for C-S-H phase are slightly higher than those reported in the literature, however in the same order of the magnitude. Thus, based on the nanoindentation behavior, it can be inferred that nano-mechanical behavior of C-S-H phase present in this binder matrix is identical to that produced in OPC concrete. In addition to diffused C-S-H skeleton, presence of nanocrystallite with superior mechanical properties (E_r =52.46 -54.02 GPa) are also identified in the matrix. Volume fractions of the different mechanical phases, as identified by nanoindentation, vary from sample to sample, which is in agreement with the highly heterogeneous structure of the hybrid composite observed in SEM and TEM images. Reproducibility of the mechanical properties, on the other hand, validate the application of the grid indentation technique in nano-mechanical characterization of the heterogeneous composite material.

6.4.3. Application of a Hybrid Clay-Lime-Starch Bio Nanocomposite Technology in Sustainable Construction Materials.

Ordinary Portland cement (OPC) based concrete is the most widely used construction material in modern human history. However, production of OPC releases a large amount of

greenhouse gases and therefore environmental sustainability is a growing concern. Typically, production of one ton of cement generates 0.55 tons of CO_2 and use of fossil fuel emits another 0.40 tons of CO_2 (Davidovits, 1991). Thus, estimated global production of 3700 million metric tons of cement in 2012 (USGS, 2013) emitted approximately equal amount of greenhouse CO_2 gas. In addition to greenhouse gas emission, disposal of other potent pollutant such as mercury, heavy metals and solid wastes are of equal concern. On the other hand, concrete based on OPC based cement themselves are prone to environmental degradation in harsh conditions, resulting in costly repairs. Overall, OPC based construction material are not environmentally sustainable and therefore there is a ever growing demand for alternative cementing binder that can substitute or supplement OPC in construction industry.

Alkaline activation of aluminosilicate rich raw materials such as clays (Kaolin, metakaolin), coal ash, blast furnace and slag produce inorganic polymers or geopolymers with network structures that have superior mechanical, thermal and chemical properties than OPC (Davidovits, 1988; Davidovits, 1991; Duxson et al., 2007; Palomo & López dela Fuente, 2003; Van Deventer et al., 2012; Xu & Van Deventer, 2000). The inherent fire resistance/thermal stability, workability, adhesive properties and acid resistance of geopolymer technology have naturally led to the development of many other products with advantageous market potential. However, the use of an alkaline hydroxide or silicate activating solution introduces some Greenhouse cost.

In the hybrid clay-lime-starch-bio-nano-composite, on the other hand, mechanical strength is achieved from the spontaneous pozzolanic reaction of clay with lime in presence of starch. Now, resources for lime are geologically widespread and abundant. Sources for biopolymer (amylopectin) are also abundant and renewal, thanks to advancement in agricultural techniques.

Similarly, clay and sand are available at negligible cost. Thus, this technology has a great potential for true "Green concrete" technology. Further, excess lime in this composite is carbonated into nanocrystalline calcite and nanocomposites in presence of biopolymer. This process absorbs CO2 from the atmosphere, in contrast to emission in other concrete preparation techniques. Nano-mechanical and structural characterization revealed the high mechanical strength, thermal and barrier properties of this composite material which are vindicated by the durability and performance of ancient structure, still in existence in some part of China. Similarly, average unconfined compression strength of 100x100x100 mm cube specimen was found to be 30 MPa (Zhang et al., 2013) which is comparable to the strength of geopolymers and type III OPC concrete (Davidovits, 1991). Thus, this technology has tremendous potential in mortar preparation, ordinary concrete design mix as well as in niche usages such as waste containment, erosion control and protective coatings.

6.5. Conclusion

Statistical deconvolution of a massive volume of nanoindentation data suggests that the cementitious binder consists of five major mechanically different phases. Based on nanoindentation characterization, primary cementing binder consisted of C-S-H phase whose nano-mechanical properties are similar to that obtained in hydration of OPC. A low volume fraction of high microporosity regions corroborates the compact nature of this hybrid concrete as observed in SEM and TEM images. Overall, superior nano-mechanical properties of the hybrid clay-lime-starch bio-nano-composite indicate its potential as one of the sustainable substitute for OPC concrete.

6.6. References

Bobko, C., & Ulm, F.-J. (2008). The nano-mechanical morphology of shale. *Mechanics of Materials, 40*, 19.

Constantinides, G., Ravi Chandran, K. S., Ulm, F. J., & Van Vliet, K. J. (2006). Grid indentation analysis of composite microstructure and mechanics: Principles and validation. *Materials Science and Engineering: A, 430*(1–2), 189-202. doi: 10.1016/j.msea.2006.05.125

Constantinides, G., & Ulm, F.-J. (2007). The nanogranular nature of C–S–H. *Journal of the Mechanics & Physics of Solids, 55*(1), 64-90. doi: 10.1016/j.jmps.2006.06.003

Constantinides, G., Ulm, F.-J., & Vliet, K. V. (2003). On the use of nanoindentation for cementitious materials *Materials and Structures, 36*, 5.

Davidovits, J. (1988). Paper presented at the Proceedings of geopolymer '88—first European conference on soft mineralurgy, Universite De Technologie De Compeigne,Compeigne, France.

Davidovits, J. (1991). Geopolymers. *Journal of Thermal Analysis and Calorimetry, 37*(8), 1633-1656. doi: 10.1007/bf01912193

Donnelly, E., Baker, S. P., Boskey, A. L., & van der Meulen, M. C. (2006). Effects of surface roughness and maximum load on the mechanical properties of cancellous bone measured by nanoindentation. *J Biomed Mater Res A, 77*(2), 426-435. doi: 10.1002/jbm.a.30633

Duxson, P., Fernández-Jiménez, A., Provis, J. L., Lukey, G. C., Palomo, A., & Deventer, J. S. J. (2007). Geopolymer technology: the current state of the art. *Journal of Materials Science, 42*(9), 2917-2933. doi: 10.1007/s10853-006-0637-z

Jennings, H. M., Thomas, J. J., Gevrenov, J. S., Constantinides, G., & Ulm, F.-J. (2007). A multi-technique investigation of the nanoporosity of cement paste. *Cement and Concrete Research, 37*(3), 329-336. doi: 10.1016/j.cemconres.2006.03.021

Mencik, J., Munz, D., Quandt, E., Weppelmann, E. R., & Swain, M. V. (1997). Determination of elastic modulus of thin layers using nanoindentation. *Journal of Materials Research, 12*(9), 2475-2484. doi: 10.1557/jmr.1997.0327

Oliver, W. C., & Pharr, G. M. (1992). An improved technique for determining hardness and elastic-modulus using load and displacement sensing indentation experiments *Journal of Materials Research, 7*(6), 1564-1583. doi: 10.1557/jmr.1992.1564

Oliver, W. C., & Pharr, G. M. (2004). Measurement of hardness and elastic modulus by instrumented indentation: Advances in understanding and refinements to methodology. *Journal of Materials Research, 19*(1), 3-20. doi: 10.1557/jmr.2004.19.1.3

Palomo, A., & López dela Fuente, J. I. (2003). Alkali-activated cementitous materials: Alternative matrices for the immobilisation of hazardous wastes: Part I. Stabilisation of boron. *Cement and Concrete Research, 33*(2), 281-288. doi: 10.1016/s0008-8846(02)00963-8

Pharr, G. M., Strader, J. H., & Oliver, W. C. (2009). Critical issues in making small-depth mechanical property measurements by nanoindentation with continuous stiffness

measurement. *Journal of Materials Research, 24*(3), 653-666. doi: 10.1557/jmr.2009.0096

Sakulich, A. R., & Li, V. C. (2010). Nanoscale characterization of engineered cementitious composites (ECC). *Cement and Concrete Research, 41*, 7.

Sneddon, I. N. (1965). The relation between load and penetration in the axisymmetric Boussinesq problem for a punch of arbitrary profile. *International Journal of Engineering Science, 3*, 10.

Ulm, F.-J., & Abousleiman, Y. (2006). The nanogranular nature of shale. *Acta Geotechnica, 1*(2), 77-88. doi: 10.1007/s11440-006-0009-5

Ulm, F.-J., Vandamme, M., Bobko, C., Alberto Ortega, J., Tai, K., & Ortiz, C. (2007). Statistical Indentation Techniques for Hydrated Nanocomposites: Concrete, Bone, and Shale. *Journal of the American Ceramic Society, 90*(9), 2677-2692. doi: 10.1111/j.1551-2916.2007.02012.x

U.S. Geological Survey (2013). Mineral commodity summaries 2013: U.S. Geological Survey, 198 p

Van Deventer, J. S. J., Provis, J. L., & Duxson, P. (2012). Technical and commercial progress in the adoption of geopolymer cement. *Minerals Engineering, 29*(0), 89-104. doi: http://dx.doi.org/10.1016/j.mineng.2011.09.009

Xu, H., & Van Deventer, J. S. J. (2000). The geopolymerisation of alumino-silicate minerals. *International Journal of Mineral Processing, 59*(3), 247-266. doi: 10.1016/s0301-7516(99)00074-5

Zhang, G., Zhang, X., Wang, B. (2013). Collaborative Research: Rediscover Ancient Chinese Concrete: the Fundamental Science and Synthesis of an Organic-Inorganic Hybrid Green Binder (unpublished)

Chapter 7. Conclusions and Recommendations

7.1. Conclusions

This dissertation had two objectives. First was the evaluation of elastic and plastic properties of clay minerals, namely muscovite mica, along two principle crystallographic direction using nanoindentation technique. Second was the statistical analysis of a grid nanoindentation data to extract the nanomechanical characterization of clay based hybrid composite. In addition, chemical and nano/micro structural characterization using X-ray diffraction (XRD) and scanning/transmission electron microscopy (SEM/TEM) was also conducted to help understand the nanoindentation results. The main conclusions of this study are

7.1.1. Nanoindentation Characterization of Muscovite Mica

- The results of nanoindentation tests performed on well-ordered mica crystal along two orthogonal crystal axes (normal to basal plane and parallel to edges) demonstrated capabilities of this method to capture anisotropic behavior of layered hydrous aluminosilicates using nanoindentation.
- The nanoindentation experimental approach has advantages over other indirect measurement methods in the sense that dislocation movement, phase changes, kinking and evolution of cracks that play key role in the deformation mechanism of layered hydrous aluminosilicates are activated during nanoindentation and thus, the test assess true mechanical properties.
- The distinct layered structure of phyllosilicates result in anisotropic behavior. Both elastic and plastic anisotropy were observed in the case of mica. The indentation modulus, M, in the direction perpendicular to the basal plane is smaller than that in the direction parallel to the basal plane, while the hardness, H, is the other way around.

- The indentation fracture toughness along the basal plane was found to be 0.38 MPa $m^{1/2}$. No prominent radial cracks could be resolved for indentation parallel to basal plane indicating either the ductile behavior parallel to basal plane or cracks were closed on the removal of the load.
- The indentation on mica also shows ISE. Indentation normal to basal plane shows local hardening while, indentation parallel to edge shows normal ISE. Simple Nix-Gao model was sufficient to model ISE in mica loaded parallel to basal plane for both macro and nano range.

7.1.2. Characterization and Nanomechanical Behaviour of a Hybrid Clay-Lime-Starch Bio Nanocomposite

- Microstructural and morphological analyses of the hybrid clay concrete indicate heterogeneous structure with different degree of activation.
- C-S-H produced by weak pozzolanic reaction between lime and clays is the principle cementing binder in this matrix.
- Presence of biopolymer (starch) in the composite material is indicated in FTIR and EDS analysis. Evidence of intercalated clay and/or C-S-H particles in TEM image indicates active interaction between inorganic binders and organic biopolymers.
- Structural analysis of the binder phase using NMR spectroscopy suggests multiple phase C-S-H in the cementitious binder of this hybrid bio-nanocomposite. Abundance of Q^2 and Q^{2ca} peaks in ^{29}Si NMR spectra indicate that some polymerization has occurred in the C-S-H. Q^4 peaks suggest the presence of three dimensional aluminosilicate networks characteristic of geopolymers.
- Statistical deconvolution of a massive volume of nanoindentation data suggests that the cementitious binder consists of five major mechanically different phases.

- Nano-mechanical properties of C-S-H phase are similar to that obtained in hydration of OPC.
- In summary, slow and weak pozzolanic reaction between clay and lime produces a cementitious binder consisting of C-S-H phase with an overall low packing density. Clay, sand, and silt particles act as active fillers in this composite, whereby forming a dense and compact mass, which renders durability and toughness to this hybrid composite.
- Superior nano-mechanical properties of the hybrid clay-lime-starch bio-nano-composite indicate its potential as one of the sustainable substitute for OPC concrete.

7.2. Recommendations

- Indentation on mica in this study only focused on two orthogonal directions i.e. normal to basal plane and parallel to edges. To further evaluate the effect of crystallographic orientation in nanomechanical deformation of mica, nanoindentation test along principle crystallographic directions [100], [001], [110] and [310] is recommended.
- It will be further interesting to explore repeated nanoindentation loading along these crystallographic orientation to examine effect of repeated loading on elastic and plastic properties, hysteresis and energy dissipation.
- Role of biopolymer (starch) in hybrid nano-composite material in facilitating pozzolanic reaction and nano-composite precipitation need to be explored further.
- MAS NMR analyses indicate the presence of networked aluminosilicates (inorganic polymer structure). However, these peaks may also be influenced by other interfering crystalline inclusions such as quartz, mulites etc. Selective dissolution of reaction products followed by chemical and structural analysis is recommended to better understand the reaction mechanism and the quantitative analysis of the different phases.

Appendix: Permissions

Dickert, Donna <ddickert@asce.org> 2:21 PM (22 hours ago)

to me

11/14/13

Dear Rohit,

Your inquiry was forwarded to me. You can reuse material you publish in your GeoCongress 2014 paper in your dissertation; however, you would need to reference the proceedings paper. No formal permission is required to reuse your own material.

If you have additional questions or concerns please feel free to contact me directly.

Sincerely,
Donna Dickert
Acquisitions Editor, ASCE
703-295-6244

SPRINGER LICENSE
TERMS AND CONDITIONS

Nov 13, 2013

This is a License Agreement between Rohit Pant ("You") and Springer ("Springer") provided by Copyright Clearance Center ("CCC"). The license consists of your order details, the terms and conditions provided by Springer, and the payment terms and conditions.

All payments must be made in full to CCC. For payment instructions, please see information listed at the bottom of this form.

License Number	3267101502361
License date	Nov 13, 2013
Licensed content publisher	Springer
Licensed content publication	Springer eBook
Licensed content title	Anisotropy of Mica Probed by Nanoindentation
Licensed content author	Rohit Pant
Licensed content date	Jan 1, 2013
Type of Use	Thesis/Dissertation
Portion	Excerpts
Author of this Springer article	Yes and you are the sole author of the new work
Order reference number	
Title of your thesis / dissertation	NANOINDENTATION CHARACTERIZATION OF CLAY MINERALS AND CLAY-BASED HYBRID BIOGEOMATERIALS
Expected completion date	Dec 2013
Estimated size(pages)	110
Total	0.00 USD
Terms and Conditions	

Introduction
The publisher for this copyrighted material is Springer Science + Business Media. By clicking "accept" in connection with completing this licensing transaction, you agree that the following terms and conditions apply to this transaction (along with the Billing and Payment terms and conditions established by Copyright Clearance Center, Inc. ("CCC"), at the time that you opened your Rightslink account and that are available at any time at http://myaccount.copyright.com).

Limited License
With reference to your request to reprint in your thesis material on which Springer Science and Business Media control the copyright, permission is granted, free of charge, for the use indicated in your enquiry.

Licenses are for one-time use only with a maximum distribution equal to the number that you identified in the licensing process.

This License includes use in an electronic form, provided its password protected or on the university's intranet or repository, including UMI (according to the definition at the Sherpa website: http://www.sherpa.ac.uk/romeo/). For any other electronic use, please contact Springer at (permissions.dordrecht@springer.com or permissions.heidelberg@springer.com).

The material can only be used for the purpose of defending your thesis, and with a maximum of 100 extra copies in paper.

Although Springer holds copyright to the material and is entitled to negotiate on rights, this license is only valid, subject to a courtesy information to the author (address is given with the article/chapter) and provided it concerns original material which does not carry references to other sources (if material in question appears with credit to another source, authorization from that source is required as well).

Permission free of charge on this occasion does not prejudice any rights we might have to charge for reproduction of our copyrighted material in the future.

Altering/Modifying Material: Not Permitted
You may not alter or modify the material in any manner. Abbreviations, additions, deletions and/or any other alterations shall be made only with prior written authorization of the author (s) and/or Springer Science + Business Media. (Please contact Springer at (permissions.dordrecht@springer.com or permissions.heidelberg@springer.com)

Reservation of Rights
Springer Science + Business Media reserves all rights not specifically granted in the combination of (i) the license details provided by you and accepted in the course of this licensing transaction, (ii) these terms and conditions and (iii) CCC's Billing and Payment terms and conditions.

Copyright Notice:Disclaimer
You must include the following copyright and permission notice in connection with any reproduction of the licensed material: "Springer and the original publisher /journal title, volume, year of publication, page, chapter/article title, name(s) of author(s), figure number (s), original copyright notice) is given to the publication in which the material was originally published, by adding; with kind permission from Springer Science and Business Media"

Warranties: None

Example 1: Springer Science + Business Media makes no representations or warranties with respect to the licensed material.

Example 2: Springer Science + Business Media makes no representations or warranties with respect to the licensed material and adopts on its own behalf the limitations and disclaimers established by CCC on its behalf in its Billing and Payment terms and conditions for this licensing transaction.

Indemnity
You hereby indemnify and agree to hold harmless Springer Science + Business Media and CCC, and their respective officers, directors, employees and agents, from and against any and all claims arising out of your use of the licensed material other than as specifically authorized pursuant to this license.

No Transfer of License
This license is personal to you and may not be sublicensed, assigned, or transferred by you to any other person without Springer Science + Business Media's written permission.

No Amendment Except in Writing
This license may not be amended except in a writing signed by both parties (or, in the case of Springer Science + Business Media, by CCC on Springer Science + Business Media's behalf).

Objection to Contrary Terms
Springer Science + Business Media hereby objects to any terms contained in any purchase order, acknowledgment, check endorsement or other writing prepared by you, which terms are inconsistent with these terms and conditions or CCC's Billing and Payment terms and conditions. These terms and conditions, together with CCC's Billing and Payment terms and conditions (which are incorporated herein), comprise the entire agreement between you and Springer Science + Business Media (and CCC) concerning this licensing transaction. In the event of any conflict between your obligations established by these terms and conditions and those established by CCC's Billing and Payment terms and conditions, these terms and conditions shall control.

Jurisdiction
All disputes that may arise in connection with this present License, or the breach thereof, shall be settled exclusively by arbitration, to be held in The Netherlands, in accordance with Dutch law, and to be conducted under the Rules of the 'Netherlands Arbitrage Instituut' (Netherlands Institute of Arbitration).***OR:***

All disputes that may arise in connection with this present License, or the breach thereof, shall be settled exclusively by arbitration, to be held in the Federal Republic of Germany, in accordance with German law.

Other terms and conditions:

v1.3

If you would like to pay for this license now, please remit this license along with your payment made payable to "COPYRIGHT CLEARANCE CENTER" otherwise you will be invoiced within 48 hours of the license date. Payment should be in the form of a check or money order referencing your account number and this invoice number RLNK501158325.
Once you receive your invoice for this order, you may pay your invoice by credit card. Please follow instructions provided at that time.

Make Payment To:
Copyright Clearance Center
Dept 001
P.O. Box 843006

Boston, MA 02284-3006

For suggestions or comments regarding this order, contact RightsLink Customer Support: customercare@copyright.com or +1-877-622-5543 (toll free in the US) or +1-978-646-2777.

Gratis licenses (referencing $0 in the Total field) are free. Please retain this printable license for your reference. No payment is required.

Vita

Rohit Raj Pant was born in 1979 in Mahakali Zone, Nepal to Dr. T. R. Pant and Mrs. Kamala D. Pant. He finished his school level education from Kanchan Vidhya Mandir and Intermediate in Science from Siddhanath Science Campus, Mahakali Zone, Nepal. He attended NIT Rourkela (formerly Regional Engineering College, Rourkela, India) from 1998 to 2002, under student exchange scholarship program for Bachelor of Engineering degree in Civil Engineering. He received a Master of Science in Civil Engineering degree with focus in geotechnical engineering from Louisiana State University in August 2007.

Rohit Raj Pant has worked on several civil and geotechnical projects as a design engineer and currently holds a Professional Engineering license in Louisiana. He is expected to fulfill his requirements for the Doctor of Philosophy degree in December 2013.